UNIVERSITÀ DEGLI STUDI DI PADOVA

SCUOLA DI SCIENZE

DIPARTIMENTO DI FISICA E ASTRONOMIA
"Galileo Galilei"

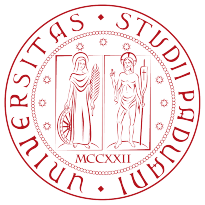

Corso di Laurea in Astronomia

Optical Characterization for the New Generation Cherenkov Telescopes

Relatore: Ch.mo Prof. *Piero Rafanelli*

Correlatore: Dott. *Enrico Giro*

Correlatore: Dott. *Giacomo Bonnoli*

Laureanda: *Rossella Spiga*

Matr. 444457/SA

Anno Accademico 2014/2015

Non al denaro non all'amore né al cielo

Fabrizio De Andrè

In the field of observation, chance only favours the prepared mind.

Louis Pasteur, 1854

Contents

INTRODUCTION

Since 80s a new astonishing window on the electromagnetic domain has been opened, revealing unexpected sources in non-thermal and violent Universe. High-energy gamma rays are generated in violent environments such as compact objects, like neutron stars and black holes, and associated with pulsars, quasars, Active Galactic Nuclei (AGN) and Gamma-Ray Bursts (GRB). The study of these sources provides clues to many basic questions in astrophysics, astroparticle physics, physics of cosmic rays till cosmological themes such as the dark matter.

The relevance of high-energy Astronomy (X rays and γ rays up to TeV energies) in the modern Science is strictly related to the technology development of the instrumentation field.

Concept of this thesis work is primarily technologic, concerning in the optical characterization of mirrors for Cherenkov telescopes and making fully operative the Mirror Test Facility of Merate (INAF – Astronomical Observatory of Brera) in the framework of CTA Project.

The first section is centered on the state of the art of ground-based Very High Energy Gamma-ray Astrophysics that has opened in the last twenty years a new intriguing observational window, initiating to new research opportunities. It is reported a brief history of the Cherenkov astronomy and the physical processes leading the observations are analysed. The imaging technique adopted by ground-based Imaging Atmospheric Cherenkov Telescopes (IACT) and the main current and next generation instruments are largely presented.

The second section consists in an analysis of the main design concepts for Cherenkov telescopes, starting from the classical Davies-Cotton to the last technological challenges, such as the optical configuration designed for the ASTRI telescope. ASTRI (Astrofisica con Specchi a Tecnologia Replicante Italiana) is the Italian SST (Small Size Telescope)

prototype for CTA and is the very first instrument implementing the double reflection for air Cherenkov imaging with a Schwarzschild-Couder optical configuration.

In the new technology telescopes segmented optics are used because of their capability of coupling low-cost and low-weight together with respect to monolithic mirror solution. The present status of the optical manufacturing technologies for the industrial mass production of the Cherenkov mirrors is largely illustrated in the framework of technical requirements of the new generation of TeV telescopes.

In the third section the topic is how to qualify reflecting panels devoted to Cherenkov telescopes. In order to characterize a generic optical system, it is needed to define and quantify global and local features of the optical surfaces and their substrates. Both optical and mechanical properties are taken into account, because performances of the mirrors are strictly related to the accuracy of their shape and the surface. Cherenkov mirrors need to survive to particular aggressive weather conditions and this makes necessary to test them for mechanical performances in robustness and stability in order to foresee long-term effects caused by environmental conditions. For this reason, a network of Mirror Test Facilities (MTF) is needed in order to characterize panels, to test equipment, and to evaluate mirror technologies in a consistent and systematic way. A cross-checking assures that the measurements performed by different facilities are coherent, in order to confirm the robustness and the accuracy of the results obtained. An overview of the CTA facilities and the main tests performed on the mirrors is presented.

The fourth section is the core of the work. It describes in detail the Test Facility of Merate (Astronomical Observatory of Brera, INAF) and discusses its measuring capabilities. Merate facility is part of the CTA network to test and characterize the mirrors to be mounted on the telescopes of the array. Due to its features, this test facility is devoted to the Medium Size Telescopes (MST) panels.

During the period January 2014/June 2015 Media Lario Technologies Company built on behalf of INAF 72 mirrors for replacing the deteriorated ones in MAGIC I and II telescopes in La Palma (Canary Islands, Spain). This brought the possibility to cross calibrate the new facility with measurements obtained during the production pipeline. The dish surface of the two MAGIC telescopes is described in details and which mirrors had to be replaced is discussed. A sample of five mirrors of the production has been tested in order to cross calibrate the overall Media Lario production and the robustness of their

calibration. Measurement activities were carried out at the INAF-Astronomical Observatory of Brera during the summer 2014. Data reduction follows, using an ad hoc IDL routine that fits and calculates Radius of Curvature, R80, FWHM and Astigmatism.

Chapter I

SKY AT HIGH ENERGY AND ITS OBSERVATION

1.1 Sources Of Gamma Radiation

1.1.1 OVERVIEW

Optical astronomy involves investigation of the electromagnetic spectrum within a narrow band between 1 μm - 300 nm. This waveband, named optical band, entirely contains the region where our eyes are sensitive (400-700 nm), where most of the baryonic matter present in the Universe emits electromagnetic signals. Starlight has a thermal distribution described by the black body model at temperatures between 3000 and 10000 K with an emission peak in the optical band. Historically, it was the first band exploited for astronomy and the only one until few decades ago. Anyway, lots of astrophysical phenomena take place in other windows of the electromagnetic spectrum such as the radio, infrared, ultraviolet, X-ray and gamma-ray band (see Figure 1).

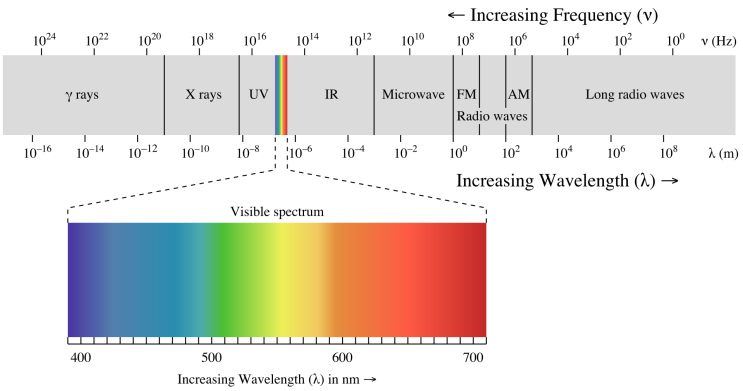

Figure 1: A common classification of the electromagnetic spectrum, with a zoom on the optical waveband.

During a series of experiments performed in 1910s, Victor Hess and Domenico Pacini independently studied the nature of a radiation today called *cosmic rays*, unknown at that time. Pacini observed the radiation strength to decrease when going from the surface to a few meters underwater, thus demonstrating that such radiation could not come from the Earth. He published his results [Pacini, 1912] one year before the famous balloon experiment by Victor Hess, who found the ionization rate to increase with height in atmosphere [Hess, 1913]. While Hess is today celebrated as the discoverer of cosmic rays, Pacini's work was largely overlooked [De Angelis, 2011]. In 1936 Victor Hess was awarded the Physics Nobel Prize for his discovery of "*cosmic radiation*", proving that the flow of high-energy particles reaching the Earth was of extra-terrestrial origin.

Cosmic rays mainly consist of charged particles, such as protons (about 90%), helium nuclei or α particles (<10%), ionized heavier elements (<1%), and electrons (<1%), while only 0.1%-1% of the total radiation consists of photons with energy >1 MeV[1]. Although rare, photons are particularly precious for astronomy as they travel through the Universe without suffering deviations in the magnetic fields that permeate it. Thus, and at variance from charged cosmic rays that are eventually isotropized losing memory of their emitter, they can be easily related to their source once their arrival direction is reconstructed, allowing to study individual gamma-ray sources

The energy of cosmic rays covers more than 10 orders of magnitude, from tens of MeV up to 10^{14} MeV and higher. The dependence of the flux on the energy *E* of the particle can be approximated by a power law

$$\frac{dN}{dE} \propto E^{-\gamma} \qquad \text{[Longair, 2011]}$$

where $\gamma = \gamma(E)$ is the spectral index with typical values between 2.5 and 2.7 in the energy range 10^9-10^{14} eV. Figure 2 shows the energy spectrum for cosmic rays.

[1] 1 eV = 1.6 x 10^{-19} J. One electron volt is the amount of energy gained (or lost) by the charge of a single electron moving across an electric potential difference of one volt.

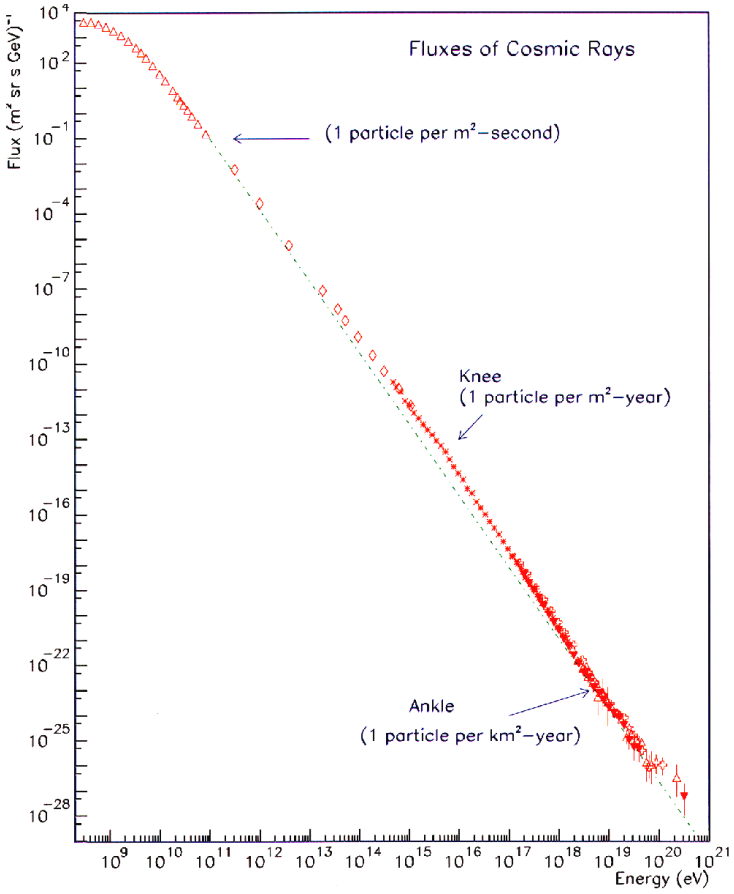

Figure 2: Energy spectrum of cosmic rays.

Of great importance is the presence of a "knee" at about 3 PeV[(2)] in the energy distribution that separates two different populations with different origins: galactic and extragalactic, respectively before and beyond this point. This interpretation is based on estimations of the strength of the magnetic field of our galaxy that should not be able to trap particles of energies greater than the knee [De Angelis et al., 2008]. Around $E = 6x10^{19}$ *eV* a rapid flux reduction is predicted; this is the so-called GZK cut-off (Greisen–Zatsepin–Kuzmin limit) [Greisen, 1966; Zatsepin & Kuzmin, 1966].

At above 10^{15}-10^{16} eV, the flux of cosmic rays drops to less than one particle per square meter per year. This rate makes direct measurements impractical, as it would require flying very large detectors in order to collect sufficient number of particles.

[2] 1PeV = 10^{15} eV

Since their energies far exceed the temperatures typically encountered in astronomical objects, cosmic rays are messengers of the *non-thermal* universe. Typical energy distribution presents a power-low spectrum, instead of the black-body spectrum commonly observed e.g. in stars.

In 1900 Paul Villard, a French chemist and physicist, discovered very high energy radiation (E > 100 keV), while studying radiation emitted from radium [Villard, 1900]. Villard's radiation was named "gamma rays" by Ernest Rutherford in 1903 [Rutherford, 1903]. Gamma rays refer to high energy photons. Due to their uncharged nature they are not deflected by a magnetic field.

Although the threshold energy for defining “high-energy” gamma rays is arbitrary, it reflects profound astrophysical and experimental arguments:

- the emission is non-thermal, and mostly produced by the conversion of gravitational energy into electromagnetic energy;
- at these energies energy photons dig into a number of cosmic rays of comparable energy, constituting a large background.

In this thesis, I will adopt the definitions outlined by Aharonian: “high energy” astronomy, or “GeV”, refers to the energy range from 30 MeV to 30 GeV, while “very high energy” astronomy, or “TeV”, refers to the range from 30 GeV to 30 TeV [Aharonian, 2004].

	Energy Range
Low - Medium Energy	0.1 MeV - 20 MeV
High Energy HE	20 MeV - 30GeV
Very High Energy VHE	30 GeV - 30 TeV
Ultra High Energy UHE	30 TeV - 30 PeV
Extremely High Energy EHE	> 30 PeV

Table 1: A classification of the gamma-ray spectral band.

The EHE band is observationally limited due to the heavy reduction of the fluxes as the energy of the observed photons increases (at 30 PeV no more than 1 photon/km^2 per day even from the most powerful sources is expected).

High-energy gamma rays can be detected even if they come from very far distances, since the detection efficiency is good and the mean free path at those energies is large: regions of the sky which are opaque in other energy bands can be transparent to X- and HE gamma-rays, providing us a key to some fundamental physics phenomena. From VHE absorption due to pair production in interaction with optical/IR photons of the Extragalactic Background light arises, originating a "gamma-ray" horizon getting increasingly narrow with the energy of gamma-rays observed [Stecker, 1973].

Among the most elusive particles permeating the Universe are neutrinos. A large quantity of neutrinos of energies within 10 MeV originates from nuclear fusion reactions inside the Sun and other stars. Neutrinos of much higher energy also originate in different processes, such as supernova explosions. Due to the extremely small cross-section of these particles, neutrinos can arrive on the Earth from the farthest reaches of the Universe, without suffering absorption or deflection by magnetic fields and for this reason they are precious information carriers.

1.1.2 PHYSICAL PROCESSES

GeV to TeV gamma rays cannot conceivably be generated by thermal emission from hot celestial objects. The energy of thermal radiation reflects the temperature of the emitting body, and there is nothing hot enough to emit such gamma rays in the known Universe.

Spectrum of the radiation of a black body of temperature T is described by Planck's law

$$B_\upsilon(\upsilon, T) = \frac{2h\upsilon^3}{c^2} \frac{1}{e^{\frac{h\upsilon}{k_B T}} - 1}$$

where υ is the frequency, B_υ is the spectral radiance of a body, T is the absolute temperature, h is the Planck constant, c is the speed light, k_B is the Boltzmann constant [Planck, 1914]. The maximum of the energy spectrum is defined by Wien's displacement law:

$$\lambda_{max} = \frac{b}{T}$$

where T is the absolute temperature in kelvin and $b \sim 2.89 \cdot 10^{-3}$ m·K (Wien's constant) [Mehra et al., 1982].

For a thermal radiator with significant emission in Gamma Rays of ~1MeV, T would be of the order of 10^{10} K. Thus, Thermal production is not the typical process for gamma radiation.

Instead, we find that high-energy gamma rays probe a non-thermal Universe, where other mechanisms allow the concentration of large amounts of energy into a single quantum of radiation (photon). The gamma-ray window is characterized by many possible radiation mechanisms. Several theoretical works had led to understand that a number of different processes, which are occurring in the universe, would result in gamma-ray emission [Feenberg & Primakoff, 1948; Hayakawa, 1952; Morrison et al., 1954; Morrison, 1957].

Mechanisms of production of γ-rays are the Bremsstrahlung, the Synchrotron radiation, the inverse Compton scattering, the curvature radiation and the pion decay, while processes of absorption are the photoelectric effect, the Compton scattering and the pair production.

The Bremsstrahlung is a 'braking radiation' that occurs whenever a fast-moving electron undergoes a Coulomb collision with an ion. This process is also called *free-free* because it is a transition between an unbound state of the electron to another unbound state (at different energy). The process can be described in a simplified way, considering a hot completely ionized and optically thin plasma made of hydrogen at temperatures 10^7 - 10^8 K in thermodynamic equilibrium and moving at non-relativistic speed. In this condition the number density of the electrons is the same of the ions $n_e = n_i$. When an electron collides with an ion it is decelerated by the positive charge and part of its kinetic energy is converted into radiation.

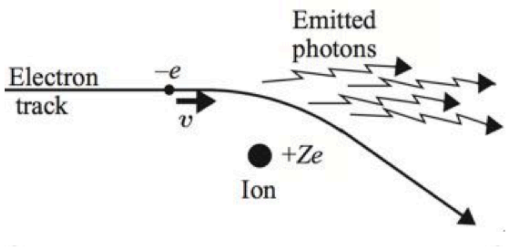

Figure 3: Free-free collision between an electron and a heavier ion.

This fixes a maximum limit to the energy of the emitted photon that cannot be greater than the kinetic energy of the electron. As a consequence, υ_{max} is defined by:

$$\upsilon_{max} = \frac{mv^2}{2h}$$

The radiation spectrum derived is continuous and it is proportional to the number density of the particles and decreases exponentially towards high frequencies. This process is also important for the detection of high-energy particles and gamma rays by means of the Imaging Atmospheric Cherenkov technique, as it occurs in the development of the Extended Air Showers produced by these particles when they enter the atmosphere.

One of the most important mechanisms that can give origin to high-energy photons is the so-called synchrotron radiation. The emission is stimulated by an acceleration process like in the Bremsstrahlung scenario, but in this case the force is related to the magnetic field instead of the electric field. In the synchrotron case an electron spirally orbits around a magnetic field line and it emits photons because it is accelerated by the Lorentz's force. For ultra-relativistic electrons (typically encountered in astrophysical situations), the emission spectrum follows power law.

The basic interpretation for the production of high-energy photons from gravitational collapses is the so-called self-synchrotron Compton (SSC) mechanism [Tavecchio et al., 1998]. Synchrotron emission from ultra-relativistic electrons accelerated in a magnetic field generates photons with an energy spectrum peaked in the infrared/X-ray range.

The Compton scattering is the process by which an incoming high-energy photon collides with an electron at rest and transfers part of its energy and momentum to the electron, absorbing energy. In this interaction the photon exchanges part of its energy with the electron that is accelerated and exits the collision with a certain angle of scattering.

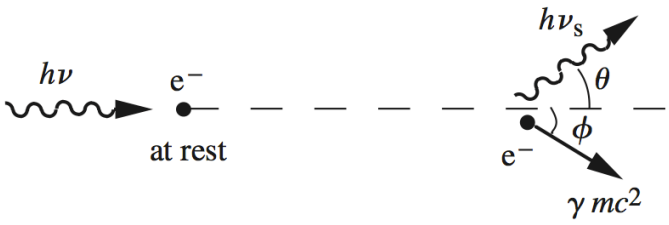

Figure 4: Classical Compton scattering.

The out coming photon has a longer wavelength and the dependence of the wavelength shift with the scattering angle is given by equation:

$$\lambda_s - \lambda = \frac{h}{m_e c}(1 - cos\vartheta)$$

where the term $h/m_e c$ = 2.42 x 10^{-12} m is called Compton wavelength of the electron.

The scattering of low-energy photons by collisions with high-energy electrons is the inverse Compton (IC) scattering. If the electron instead of being at rest is moving at relativistic speed the energy transfer in Compton interaction is reversed (for this reason it is called *inverse*). This mechanism is very effective for increasing the photon energy and is important in regions of high soft-photon energy density and energetic-electron number density.

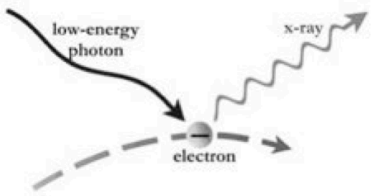

Figure 5: Scheme of inverse Compton scattering.

Particularly important for the interpretation of the spectral energy distribution of the VHE sources is the Synchrotron-Self-Compton (SSC) mechanism. As discussed, relativistic electrons immersed in a magnetic field emit synchrotron radiation. If the photons number density is sufficiently high, the radiation can be up-scattered to higher energies via Inverse Compton process by the same population of relativistic electrons. The SSC

mechanism is responsible for the presence of two well-defined peaks in the spectral energy distribution of many galactic and extragalactic VHE sources [Gao et al., 2013].

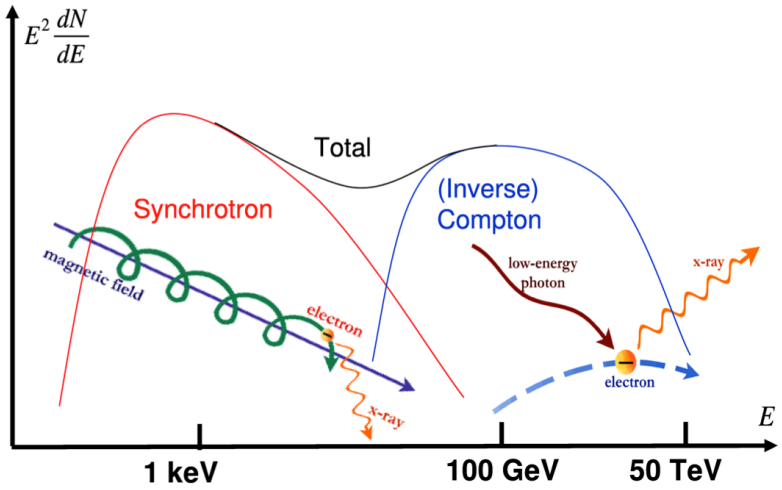

Figure 6: Energy spectrum of photons in the SSC model [De Angelis et. al., 2008].

Another important source of gamma photons is provided by the pion decay. Pions are the lightest and unstable mesons and they are the carrier of the strong nuclear force. They are usually produced in the collision between hadrons. The process of interest for this context is the collision between cosmic rays and the hadrons in the cosmic matter (mainly gas). There are three types of pions: charged positive and negative $\pi^{\pm}$, and neutral π^0. The charged pions, with masses $m_{\pi^{\pm}}$~139.6 MeV/c^2, have a short lifetime (~ 26 ns) and they decay by the following leptonic reactions:

$$\pi^{\pm} \rightarrow \mu^{\pm} + \overline{\upsilon}_{\mu}$$

$$\pi^{\pm} \rightarrow e^{\pm} + \overline{\upsilon}_{e}$$

The neutral pions, that have masses m_{π^0}~135 MeV and a lifetime of 10^{-17} s, undergo electromagnetic decay by the emission of high-energy rays:

$$\pi^0 \rightarrow \gamma + \gamma \qquad \text{(a)}$$

$$\pi^0 \rightarrow e^+ + e^- + \gamma \qquad \text{(b)}$$

The decay (a) is the preferred channel (99%). Pion decay together with the Inverse Compton scattering is one of the most efficient mechanisms of production for the gamma-ray radiation.

One of the main mechanisms of absorption of high-energy photons by the atoms in the matter (apart the Compton scattering discussed above) is the photoelectric effect. In 1905 Albert Einstein [Einstein, 1905] explained the photoelectric effect using the Planck hypothesis for which the energy of light is quantized into the photons. At relatively low energies ($h\nu << m_e c^2$), if the photon energy is greater than the binding energy E_b of an electron into a certain atomic shell the particle is freed from the attractive force of the nucleus and it is ejected with a kinetic energy, ($h\nu$ - E_b). This process dominates the photon-absorption interactions for energies below 100 keV (X-ray).

The most important absorption mechanism for the VHE radiation in the Universe is given by the photon-photon ($\gamma\gamma$) interaction that leads to the pair production of matter and anti-matter particles (clearly, electrons and positrons are favoured products due to their low mass) by the interaction:

$$\gamma + \gamma \rightarrow e^+ + e^-$$

Very high-energy photons interact with the galactic and extragalactic cosmic background photons that permeate the space-time of the Universe. It is a threshold process, preferentially occurring for well-matched energy of the high energy and soft photons.

The background radiation, called extragalactic background light (EBL), is the integrated mean surface brightness of the sky due to resolved and unresolved galactic and extragalactic sources in all the wavebands of the electromagnetic spectrum from all the cosmic epochs.

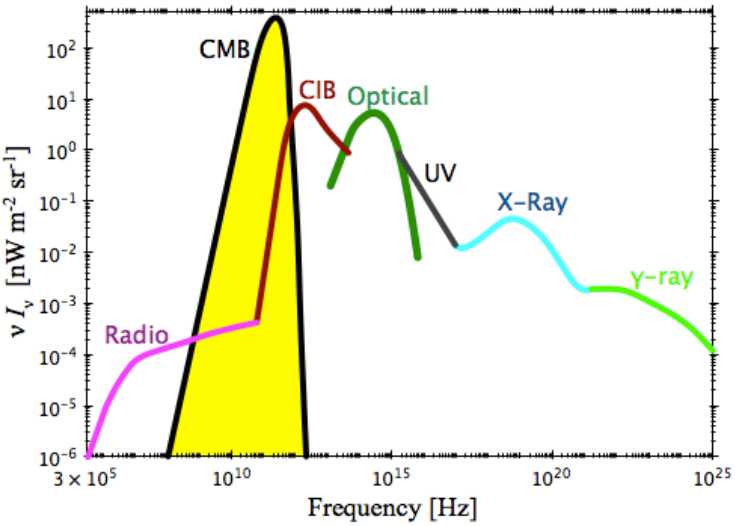

Figure 7: Intensity of the "background light" integrated over all sources in the Universe [Dole and Bethermin[3]].

The cosmic radio background radiation accounts for a small contribution to the EBL. The cosmic microwave background (CMB), the fossil radiation from the earliest epochs of the Universe, is the predominant source of the EBL (~ 400 photons/cm^{-3}) and it is a perfect black body at 2.73 degrees Kelvin. This isotropic and diffuse radiation plays an important role also in the detection of high-energy photons in the gamma domain.

The cosmic infrared background (CIB) is mainly due to re-emitted starlight by dust grains, galactic cirrus, cold stars and zodiacal light. The light does not come directly from stars, but is re-processed as visible starlight and absorbed by interstellar dust, which heats up and in turn glows in the infrared. The optical and UV backgrounds are directly related to stellar and Active Galactic Nuclei (AGN) emission. The X-ray background is well resolved into discrete sources while the background is mainly diffuse and probably associated to the interactions of the cosmic rays with the interstellar medium. Background photon flux is coming from both very hot gas, heated by falling into clusters of galaxies on large scales, or by supernovae within galaxies, along with the very energetic collisions between particles in the environments around black holes as matter falls in.

[3] www.andrewjaffe.net/blog/2011/09/passion-for-lig.html

1.1.3 RELEVANCE OF HIGH-ENERGY ASTROPHYSICS IN MODERN SCIENCE

High-energy astrophysics, with cosmology and planetary sciences, is one of the three most active branches in the contemporary astrophysics [Zhang et al., 2013]. This field study astrophysical objects emitting high-energy photons (X rays and γ rays) and more generally emitting non-thermal photons outside the traditional optical wavelengths. Gamma rays are primary messengers of the non-thermal and violent Universe. They allow inferring the mechanisms of their production and acceleration. Moreover, they keep tracks of the physical properties of the environment traversed from the source to the observer.

By studying non-thermal emission in the Universe, it is possible to unveil the part of it that is not in a steady state, usually originating in violent environments near compact objects, such as neutron stars and black holes. These objects, besides emitting the broadband non-thermal electromagnetic radiation, are also believed to be emitters of other signals outside the electromagnetic channel. These multi-messenger signals include cosmic rays, neutrinos, and gravitational waves. The goals of TeV astronomy are wide-ranging, but can broadly be described as the study of sites of relativistic particle acceleration in the Universe, both hadronic and leptonic. This encompasses a huge range of size scales and energetics, from the interactions of galaxy clusters, to the magnetospheres of individual pulsars. Because it is very difficult to produce gamma rays, the objects that emit them are very interesting to astrophysicists. High-energy gamma rays are associated with exploding stars (supernovae), pulsars, quasars, and black holes rather than with ordinary stars or galaxies.

The main field in cosmological research for dark matter in γ -ray energy range is related to the detection of photons emitted by self-annihilation of WIMPs (weakly interacting massive particles). These dark matter particle candidates, heavier than the proton, should be weakly interacting with ordinary matter, and therefore neutral. WIMPs should be long-lived enough to have survived from their decoupling from radiation in the early universe into the present epoch.

The emission of high-energy gamma rays from cosmic objects always implies the presence of exotic and extreme physical conditions, high magnetic and electric fields, shock waves, cataclysmic explosions, etc. In fact, this emission offers the best direct probe of the extreme conditions in these exciting phenomena.

During the past decades, the field of high-energy astrophysics has enjoyed a rapid development, thanks to a large list of space-based and ground-based observational facilities. These instruments have greatly advanced our understanding of various high-energy phenomena, including stellar-scale black holes in binary systems, super-massive black holes in Active Galactic Nuclei (AGNs), Gamma-Ray Bursts (GRBs), several objects in the neutron star list, as well as supernovae and their remnants. Thanks to the advent of cornerstone space missions as the Fermi and AGILE satellites and the construction of ground-based Cherenkov telescopes, the gamma-ray astronomy has unlocked a completely new, unproved window on the high-energy Universe. In this way detailed full-sky maps in the gamma domain have been provided.

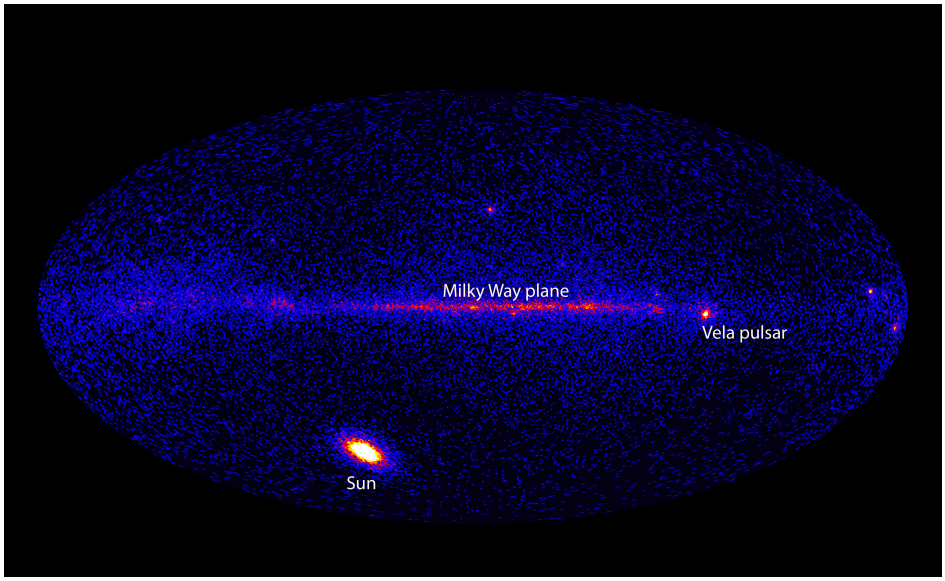

Figure 8: Image from Fermi's Large Area Telescope (LAT) showing the light of gamma rays with energies beyond 100 MeV and up to ~100 GeV in the entire sky.

The study of these sources provides clues to many basic questions in astrophysics, astroparticle physics, physics of cosmic rays and cosmology.

1.2 Gamma-Ray Observations

The identification of the Crab Nebula as the first TeV gamma-ray source, in 1989, opened the studies of the electromagnetic spectrum in the range between 30 GeV and 30 TeV [Weekes et al., 1989]. The Crab Nebula was first detected in the Whipple Observatory with an IACT (Atmospheric Cherenkov Imaging Telescope, largely discussed in the following sections) equipped with a 10 m optical reflector and a 37-pixel camera. This important experiment is commonly assumed to mark the birth of the ground-based VHE gamma astronomy.

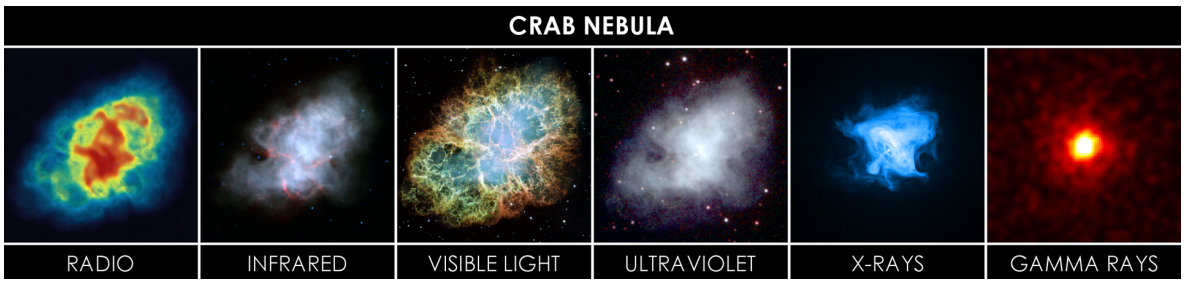

Figure 9: Crab Nebula in multiple wavelengths.

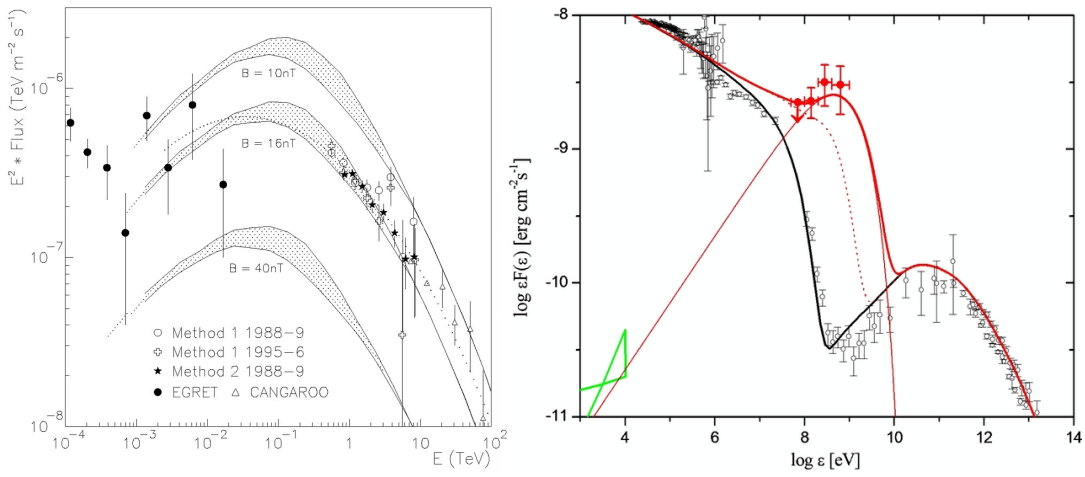

Figure 10: Left: The VHE spectral energy distribution of the Crab Nebula compared with the predictions of a synchrotron self-Compton emission model [Hillas, et al. 1998]. Right: The crab nebula super-flare observed by AGILE. The red curve is the result of the theoretical modelling of the super-flare; data points marked in black show the average nebular spectrum [Striani et al., 2011]. The flare is evident at HE, while on the right, the Inverse Compton peak observed at VHE seems unaffected. Therefore Crab Nebula can still be considered a good calibration standard at these energies, while it is now know to vary significantly at HE.

This observation proved that the flux came from the hard Inverse Compton spectrum of the nebula. The Crab Nebula has become the standard candle for TeV Gamma-ray Astronomy, available as a steady source to test and calibrate the IACT visible from both hemispheres.

As of today over 160 sources of gamma rays of very different types, of both galactic and extra-galactic origin, have been discovered with this technique. This is a really fast evolving branch in science, rapidly improving our understanding of the most violent and energetic sources and processes in the sky [Mirzoyan, 2014].

The first images of the plane of the plane Milky Way in VHE gamma rays have been obtained in the last few years. These reveal a chain of gamma-ray emitters situated along the Galactic equator, demonstrating that sources of high- energy radiation are ubiquitous in our Galaxy [Carrigan et al., 2013].

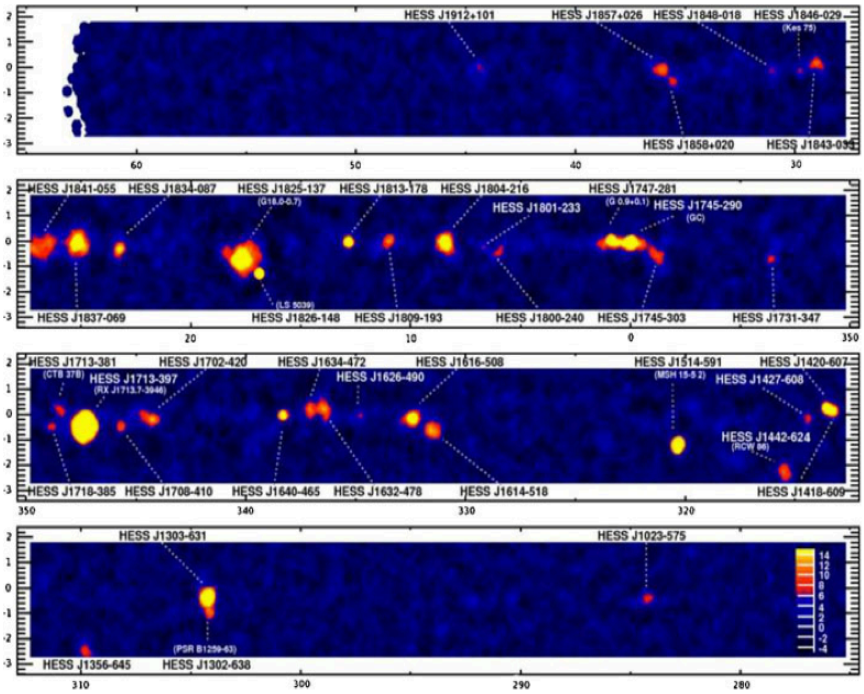

Figure 11: The plane of the Milky Way viewed in VHE gamma rays, in four bands of Galactic longitude [Aharonian et al., 2006].

Figure 12 shows the sky near the Galactic plane in spectral lines and continuum bands spanning a frequency range of more than 14 orders of magnitude, as result of the coverage of the electromagnetic spectrum by ground-based and spaced-based instruments.

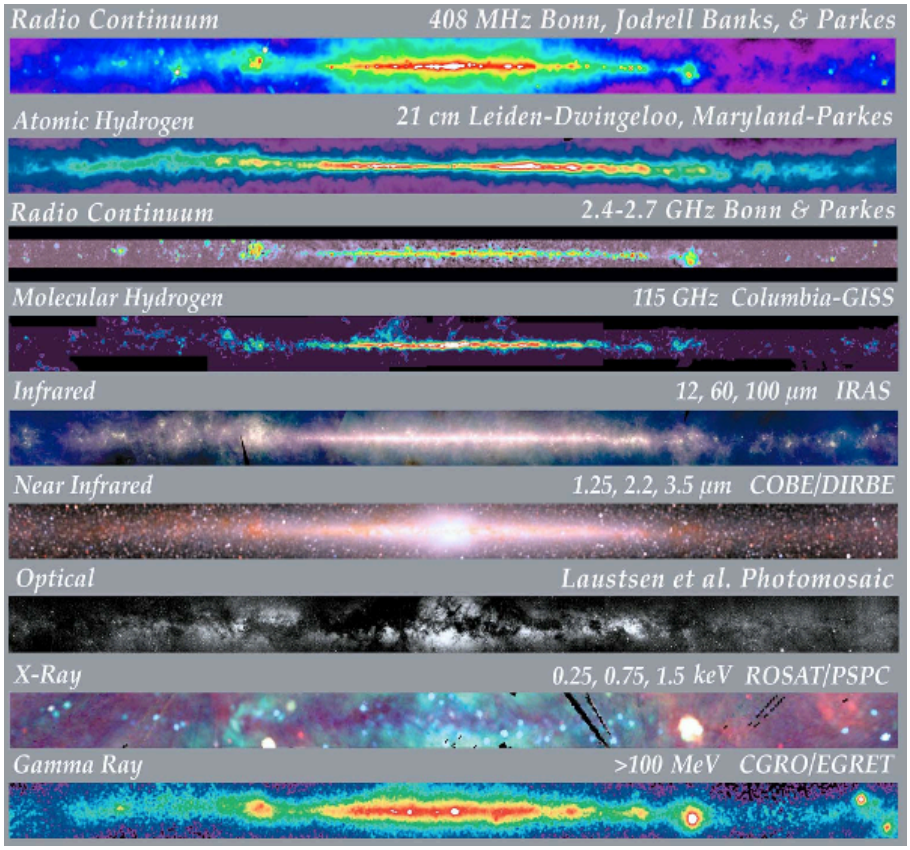

Figure 12: Multi-wavelength images of the plane of the Milky Way. [4]

The intensity map of high-energy gamma-ray emission (observed by the Energetic Gamma-Ray Experiment Telescope EGRET instrument) includes all photons with energies greater than 300 MeV. At these energies, most of the celestial gamma rays originate in collisions of cosmic rays with nuclei in interstellar clouds, making the Milky Way a diffuse source of gamma-ray light. Along the Galactic plane there are several gamma-ray pulsars, e.g., the Crab Nebula. Away from the plane, many of the sources are known to be Active Galactic Nuclei (AGNs).

[4] http://mwmw.gsfc.nasa.gov/

1.2.1 DIRECT DETECTION

The Earth's atmosphere absorbs electromagnetic radiation at most infrared, ultraviolet, X-ray, and gamma-ray wavelengths. Only two atmospheric windows, in the radio and visible wavebands are widely accessible to ground-based astronomy.

Except for some sharp bands in the near infrared and a large window in the radio band the Earth's atmosphere is opaque to most of the infrared radiation and all the wavelengths beyond 320 nm as shown in Figure 13, where we can see that the major windows are at visible wavelengths (marked by the rainbow) and at radio wavelengths from about 1 mm to 1 m.

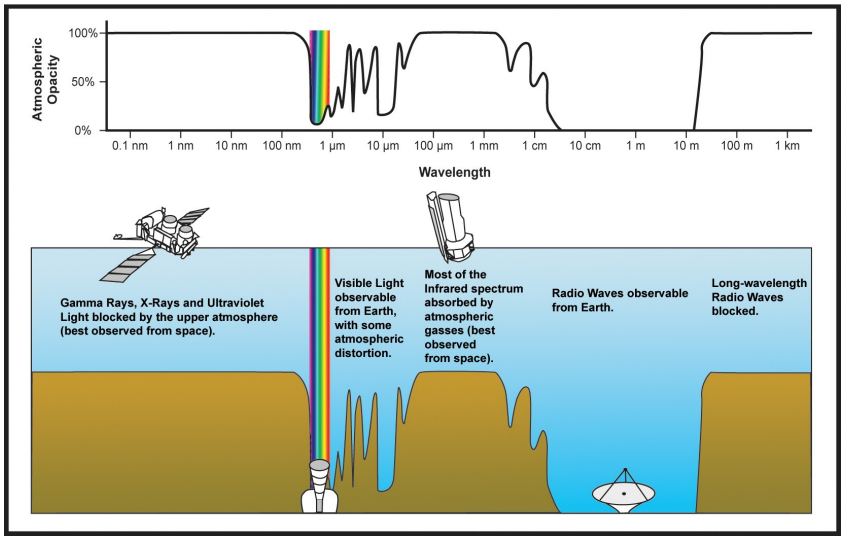

Figure 13: Atmospheric Opacity as a function of wavelengths [Credit: ESA/Hubble].

The source of opacity for the infrared radiation comes mainly from the absorption by molecules of water vapour and OH present in the atmospheric mixture, while ozone (O_3) molecules in the stratosphere absorb the ultraviolet radiation. X-rays and low energy γ-rays are blocked by photoelectric processes with the molecules of the Earth's atmosphere while the Very High Energy (VHE) rays undergo Compton scattering processes and electron-positron pair production.

To observe the far-infrared, X-ray and γ-rays emission from the celestial bodies, balloons, sounding rockets and satellite are hence necessary. The development of sounding rockets capable of carrying instruments outside the absorbing layers of the Earth's atmosphere made possible the observation of celestial objects in the X-ray range of wavelength

coming from sources outside the Solar System [Giacconi et al., 1962]. Riccardo Giacconi and his team observed a considerable flux of radiation - identified as soft X-rays - coming from a region of sky where Cassiopeia A and Cygnus A are located. The discovery was awarded with the Nobel Prize in 2002, marking the birth of the high-energy astrophysics.

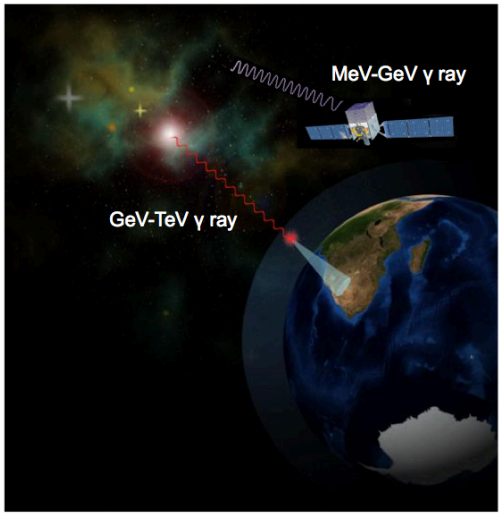

Figure 14: Gamma- ray observations: from space and from ground.[5] *Courtesy of G. Rodeghiero.*

Gamma-ray photons can be observed from space in the MeV - GeV domain or indirectly by ground in the GeV - TeV spectral window.

The space-based detectors are limited in size and very expensive. Moreover, the flux of very high-energy (VHE) gamma rays (energies above ~ 100 GeV) is so small that even the largest space-based gamma-ray telescopes cannot detect enough photons coming from the sources of this radiation. The satellite observatories have a very limited effective area and a low sensitivity, but they have a large duty cycle and a low background. Also the maximum measurable energy of photons is limited as the interaction products must be fully stopped into the detector to allow an accurate measurement. For instance, the FERMI/LAT detector can measure accurately photons with energies up to ~300 GeV [Atwood et al., 2009].

The number of satellites launched to study gamma ray emission from celestial bodies by all the countries is remarkable: 22 missions in 1960s, 31 in 1970s, 11 in 1980s, 16 in

[5] www-ucjf.troja.mff.cuni.cz/ hess/experimental.php

1990s and 4 in 2000s [6]. The cornerstone mission in this field, marked also the beginning of the modern era of such studies, is the Compton Gamma Ray Observatory (CGRO) that operated for about ten years since 1991. The satellite covered more than six orders of magnitude in energy from 30 keV to 30 GeV and amongst its primary discoveries it proved the isotropic distribution of the GRBs, it mapped the entire Milky Way using the ^{26}Al gamma-ray line. Because gamma rays at energy of 1.8 MeV have the characteristic energy of the radioactive decay of aluminium isotope and pass through the interstellar medium with negligible absorption, the Imaging Compton Telescope (COMPTEL[7]) provided an efficient way to trace sites of nucleosynthesis in the Galaxy at this energy.

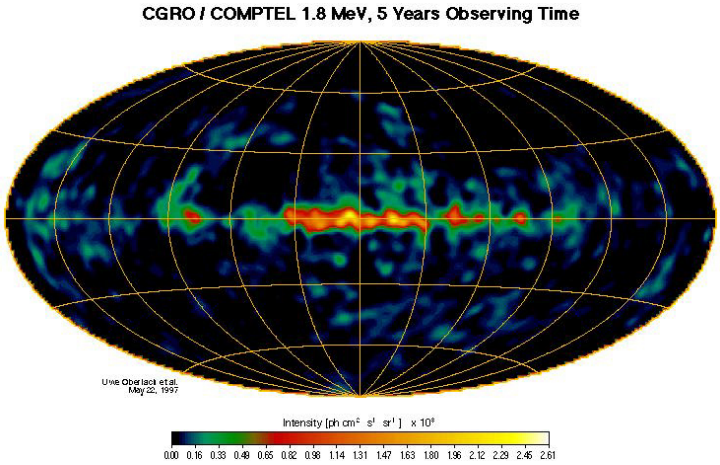

Figure 15: CGRO/COMPTEL map of the Milky Way at energy of 1.8 MeV[7]

A successful Italian mission is AGILE, a space observatory sensitive to the energy range between 30 MeV and 50 GeV. It was launched in April 2007 and it discovered temporal flux variability in many sources and about a dozen of pulsar emitting at the GeV scale. The design of AGILE derived from the experience of the EGRET instrument on board of the CGRO [Tavani, 2008].

The state of the art of gamma-ray satellites is represented by FERMI, originally Gamma-ray Large Area Space Telescope (GLAST)[8] [Gehrels et al., 1999; Michelson, 2003].

---

[6] http://imagine.gsfc.nasa.gov/docs/sats_n_data/gamma_missions.html

[7] http://heasarc.gsfc.nasa.gov/docs/cgro/comptel/

The mission is the result of a collaboration of many countries, under the leadership of NASA. The mission began the observations in 2008, and its spacecraft hosts the most sensitive instrument ever built in the range 20 MeV – 300 GeV the Large Area Telescope (LAT).

Figure 16: Artistic image of the FERMI spacecraft. The LAT detector is visible on top. Its effective area is ~1 m^2.

The two missions AGILE and FERMI improved greatly our knowledge of the sky at gamma rays, and allowed to perform simultaneous observations with ground-based Imaging Atmospheric Cherenkov Telescopes (see section I.3.2). Moreover, the presence of other X-ray experiments in orbit (e.g. Swift, Chandra, Newton- XMM, etc.) made possible for the first time to observe astrophysical sources all over the whole electromagnetic spectrum at almost same time.

1.2.2 CHERENKOV DETECTION

The discovery of the Cherenkov radiation is of primary importance for the development of ground based VHE gamma-ray observations. Marie Curie firstly noted in 1910 [Curie, 1910], a bluish faint light emitted by the bottles containing a solution of liquids and some radioactive compounds. The phenomenon was then studied by Mallet who discovered the continuum spectrum of this radiation and excluded it from being a result of some luminescence processes. The task of studying this new radiation was given to Pavel

Cherenkov by his supervisor Sergei Vavilov in 1932. With his experiment, Cherenkov discovered that β-particles and more generally electrons liberated into the liquid during scattering processes of the γ-rays, created a bluish light that propagated mainly in the onward direction of the primary beam [Cherenkov, 1937].

Cherenkov light is an electromagnetic radiation due to the interaction of charged particles moving in a transparent dielectric medium with the particles of the medium itself, occurring when the speed is $v > \frac{c}{n}$ (c = light speed in the vacuum; n = refraction index of the medium). If a particle passes through a transparent dielectric medium, the atoms along its trajectory become temporarily polarized and emit electromagnetic waves due to polarization.

If $v > \frac{c}{n} = c'$ the particle moves at a velocity that is faster than the speed of light in this medium, the waves interfere in a constructive manner.

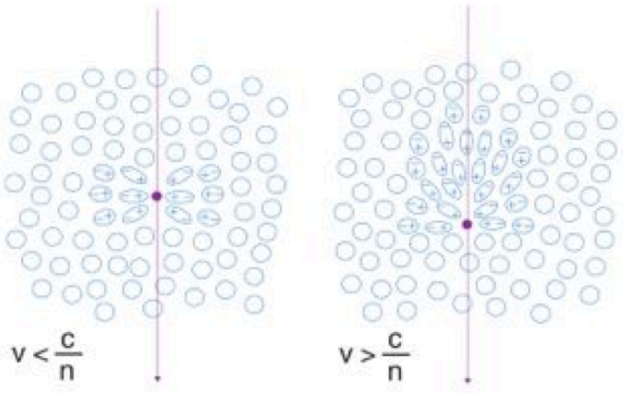

Figure 17: Left: Polarization of a dielectric refractive medium by a slowly moving charged particle (purple arrow). Right: Polarization effect of a fast moving charged particle, superluminal in the medium, that causes the emission of a coherent radiation called Cherenkov radiation [Courtesy of C. Schultz].

The Huygens principle [Landau & Lifshitz, 1971] can be applied to retrieve the angle for which the wavefronts are added coherently to create Cherenkov radiation. With reference to the geometry in

Figure 18 we define $\beta = \frac{v}{c}$ the ratio between the particle and the light speed and Δt the time of flight of the particle.

$$\frac{c}{n}\Delta t = \beta c \Delta t cos\theta \quad \rightarrow \quad cos\theta = \frac{1}{\beta n(\lambda)}$$

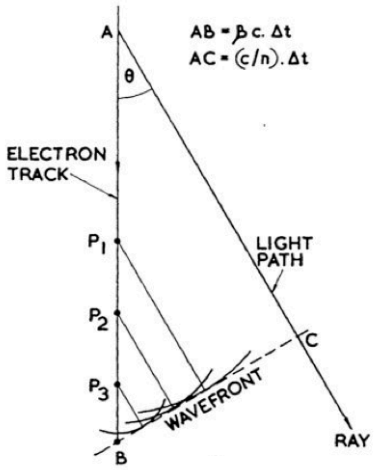

Figure 18: Geometry of the Cherenkov emission: the wavefronts from the polarized molecules combine coherently for a well-defined angle θ. The overall envelope results in a cone of radiation pointing in the direction of the particle motion [Galbraith & Jelley, 1953].

For a medium of a given refractive index n, there is a threshold velocity $\beta_{min} = \frac{1}{n}$, below which there is no emission of radiation. At this critical velocity the direction of radiation coincides with that of the particle. On the other hand, for an ultra-relativistic particle (β= 1) there is a maximum angle of emission, given by $cos\theta = \frac{1}{n}$. A real medium is always dispersive (n > 1), so actually radiation is restricted to those wavelengths for which n (λ) > 1. Conversely in the X-ray domain n (λ) is always < 1 and radiation is forbidden.

The Cherenkov photons form a cone-shaped wavefront centred on the particle trajectory at an aperture angle θ_c with respect to the particle direction.

The cone angle of the Cherenkov radiation depends on the speed of the particle and the refractive index of the medium: in air (standard temperature and pressure) the angle θ_c is within the range of 0.4° – 1.2°, in water and ice are wider, $\theta_c \sim 40°$.

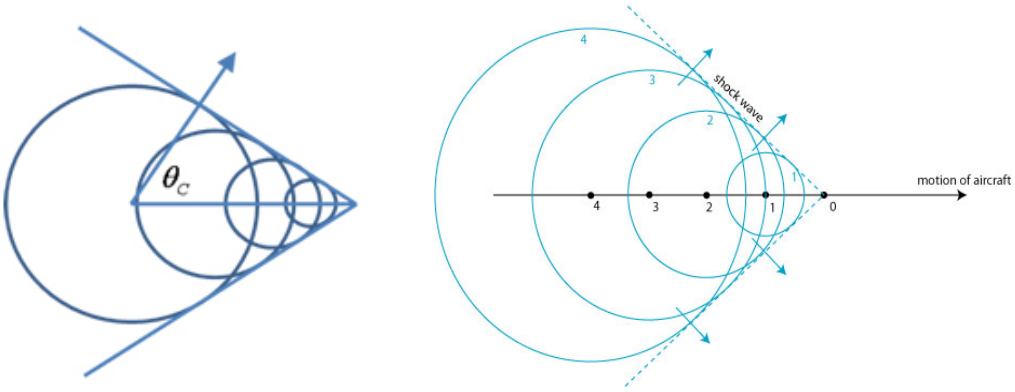

Figure 19: Analogy between Cherenkov cone and Mach cone.

The light emitted appears blue because most photons produced by the Cherenkov effect are in the ultraviolet part of the electro-magnetic spectrum. The Cherenkov effect is often compared to the sonic boom caused by ultra-sonic aircraft in air. This effect is commonly observed at nuclear reactor sites, as energetic electrons due to beta decay produced by radioactive material enter the water surrounding them travelling at superluminal speed in water.

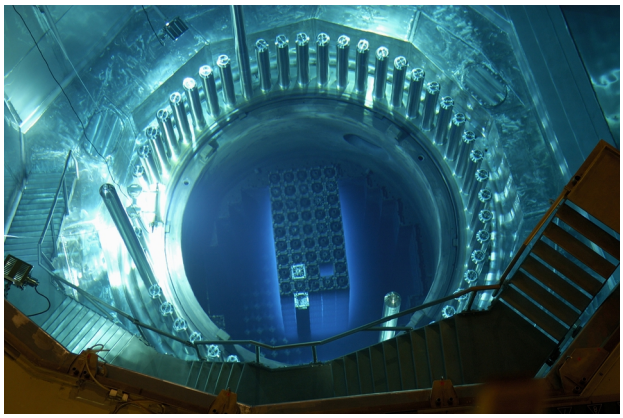

Figure 20: Nuclear reactor core and Cherenkov radiation.

The Nobel Laureate P.M.S. Blackett first reported to the Royal Society [Blackett, 1948] of the possibility that cosmic rays are contributing to light of the night sky by means of Cherenkov radiation. Very high-energy gamma rays and cosmic rays can be detected from the ground via secondary radiation they produce when they strike the atmosphere

generating a cascade of particles, a fraction of which is charged and superluminal. The secondary radiation is produced as a brief flash of blue light (Cherenkov light) caused by these particles.

More in detail, a γ-ray impinges the top atmosphere due to interaction with the electric field of atmospheric molecules, it produces an electron-positron couple:

$$\gamma_\gamma \rightarrow e^+ + e^-$$

The reaction has an energy threshold and normally takes place for γ-rays in the VHE band. Each electron-positron in turn generates new γ-rays via bremsstrahlung:

$$e^{\pm}(\gamma) \rightarrow e^{\pm}+\gamma$$

where the secondary gamma rays emerge with a continuous spectrum but in the first approximation it can be simply assumed that they carry half of the energy of the electron.

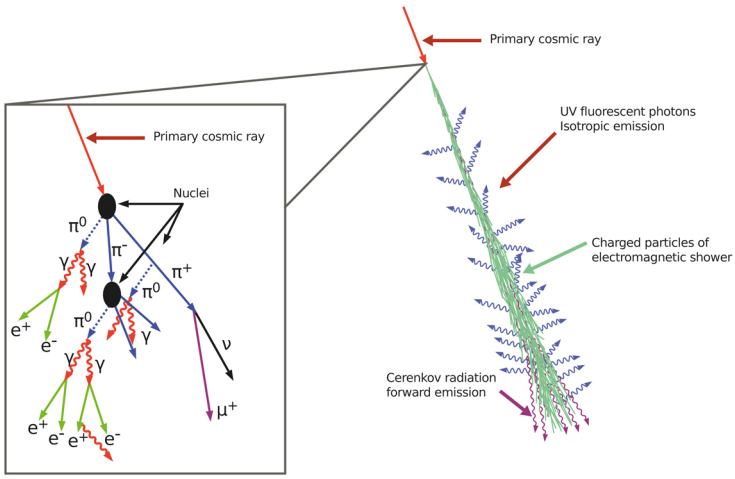

Figure 21: A sketch of the shower development of a cosmic ray.

Eventually the secondary γ-ray again produces a pair electron/positron and so on, and the γ-shower keeps on producing new generations of particles if total energy is enough.

The energy of secondary particles produced in the shower decreases as the shower proceeds while the number increases. When the mean energy of $e^{\pm}$ is below a critical energy $E_c \approx 83$ MeV (in the air), the dominant energy loss process for electrons becomes ionization, rather than bremsstrahlung. Almost contemporary, when the mean photon energy decreases below few MeV, the cross-section for Compton scattering and photoelectric absorption becomes dominant over pair-production. Rapidly the showers stop. The Cherenkov light is extremely faint (~7 opt. photons/m^2 per primary gamma

ray with energy ~ 300 GeV) [Longair, 2001] and only lasts for a few billionths of a second but is observed in an even narrower time interval (~10^{-9} s) [Heß et al., 1999]. Cherenkov light reaching the ground from air showers peaks at optical/UV wavelengths [Holder , 2012].

Also the cosmic rays that invest the Earth (primary particle) enter the upper layers of the atmosphere and impact one of its atoms developing a cascade process, also labeled Extensive Air Shower (EAS), of ionized particles and photons (secondary and tertiary particles) that reach the ground. They interact strongly with atmospheric nuclei creating pions, kaons and nucleons. The secondary particles keep on multiplying in successive generations until the mean energy per particle drops below the pion production threshold at around 1 GeV. At that point, ionization becomes the dominant process and the shower starts to die out.

The Cherenkov emission from an air shower produces a conical flash of blue light of blue light, with the maximum emission occurring around 10 km above sea level at TeV energies (lower, for higher energies).

1.3 Ground-based Observations

Ground-based astronomy is confined to the visible/infrared and radio atmospheric windows, these being the frequencies of the electromagnetic spectrum in which most radiation can reach the ground. The high-energy portion of the electromagnetic spectrum is completely inaccessible from ground-based observations.

Despite the high duty cycle and the privileged view on the Universe of the space observatories, the high costs and the relatively short lifetime motivate the construction of ground-based detectors. Unlike satellite observatories, rather inefficient in terms of effective area, ground-based detectors have large effective area and consequently a high sensitivity, but they have also a low duty cycle and they suffer a high background. Furthermore, given the very low fluxes of γ-rays in the VHE regime, a few photons per m^2 per year above 1 TeV for strong sources, direct detection by space-based instruments is excluded.

In such a scenario, it is needed to develop ground-based instruments in order to significantly improve the sensitivity, the observed energy band, the field of view and the observing time.

Ground-based detectors are divided into two main categories: Extensive Air Shower (EAS) detectors and Imaging Air Cherenkov Telescopes (IACT).

Both the techniques are based on the observation of particles and photons from the interaction of the primary ray with the upper layers of the troposphere. In ground-based observations, the atmosphere is a part of the detection system and is the key ingredient for reaching the large collection areas typical of this kind of detectors.

Ground–based astronomy with the imaging atmospheric Cherenkov technique can observe photons in the band γ–ray from around 100 GeV up to several TeV. While charged particles of the Extensive Air Shower (EAS) are usually completely absorbed in the atmosphere and do not reach the ground, Cherenkov photons can propagate. The Cherenkov light is emitted at around 10 km altitude. There is only some absorption in the UV band, but most of the light can reach the ground [Rao, 1998]. One of the important contributions of Bruno Rossi is the discovery and the study of extensive air showers [Rossi, 1964].

If a telescope is located inside the Cherenkov light pool (~120 m wide in radius at the ground, as the shower starts to develop around 10 km and the Cherenkov cone has an aperture of ~1°), the photons are reflected onto the focal plane and in a shape that resembles an ellipse. The ellipse contains information about the primary γ–ray that initiated the shower: the ellipse size is related to the γ–ray energy and its position and orientation in the camera are related to the shower direction [Doro, 2009].

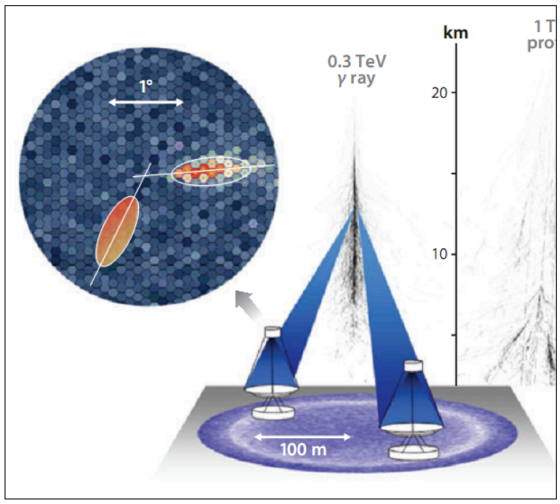

Figure 22: Scheme of Cherenkov light detection on ground with IACT.

In contrast to the well-collimated electromagnetic air showers induced by γ-rays (or electrons), air showers initiated by cosmic ray nucleons typically feature a number of electromagnetic sub-showers induced by π_0 decays and contain muons from charged pion decays.

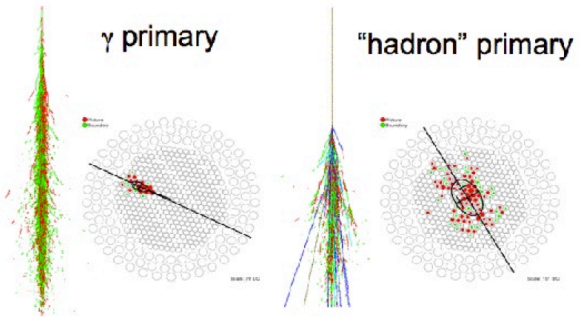

Figure 23: Typical spatial development of γ- and hadron-induced air showers.

The Cherenkov images of cosmic rays (not gamma rays) initiated air showers are consequently wider then those with γ-ray primaries, and form an irregular shape, as opposed to a smooth ellipse. In addition, since the original charged particle has been deflected by galactic magnetic fields before reaching the Earth, cosmic-ray images have no preferred orientation in the camera but they appear as an isotropic flux [Holder, 2012]. Rejection of the background of showers initiated by charged cosmic rays is a key performance criterion for γ-ray detection systems, and is usually achieved on the basis of gamma versus hadronic shower discrimination.

From the beginning of gamma ray astronomy, data analysis techniques were mostly based on the "Hillas parametrisation" [Hillas, 1985] of the shower images, relying on the fact that the Cherenkov event images in the camera focal plane are, to a good approximation, elliptical in shape (Hillas ellipsoids).

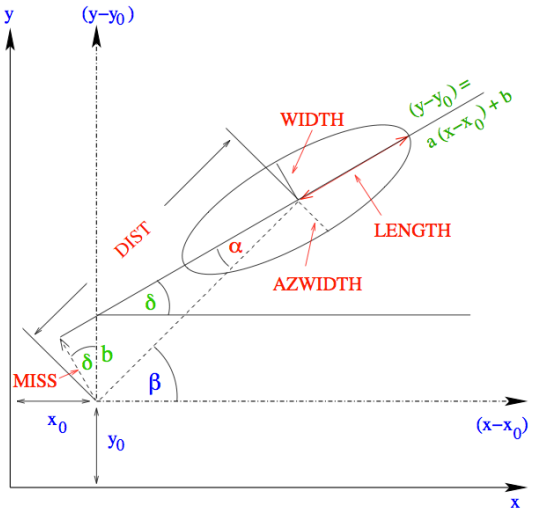

Figure 24: The characterization of the camera image based on the Hillas parameters.

The main Hillas parameters are:

- *size:* sum of the number of photons in the image;
- *alpha:* angle between the major ellipse axis and a line going from the centre of the ellipse to the centre of the camera.;
- *dist:* distance from the centre of the ellipse to the camera centre;
- *length:* major semi-axis of the ellipse;
- *width:* minor semi-axis of the ellipse.

This parameterisation permits to disentangle between gamma and hadronic events, e.g. *width* is generally narrower for gamma-ray initiated showers than for hadronic ones. Moreover to reconstruct energy and direction of the primary gamma rays from the Hillas parameters is possible. Gamma-ray showers can be discriminated by means of the image shape and orientation. Gamma-ray images result from purely electromagnetic cascades and appear as narrow, elongated ellipses in the camera plane. The major axis of the ellipse corresponds to the vertical extension of the air shower, and points back towards the source position in the field of view. The major axis of the ellipse corresponds to the

vertical extension of the air shower, and points back towards the source position in the field of view. If multiple telescopes are used to view the same shower, the source position is the intersection point of the various image axes in the plane of the sky. The intensity of the image is related to the energy of the gamma ray.

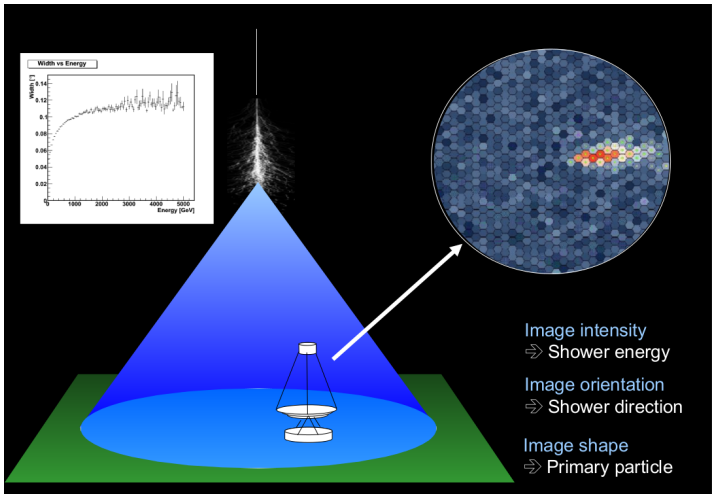

Figure 25: Schematic description of the IACT technique. In the circle an image of γ-induced air shower as it appears in the camera [Credits: M. Mariotti].

A typical Cherenkov light flux density between 300 and 600 nm from a 1 TeV gamma shower is around 100 photons/m^2, nearly uniformly spread over an area of 50000 m^2 at ground. The faint light flashes must be detected against a substantial night sky light background. Even if the hadronic background cannot be completely removed, gamma/hadron separation efficiency can be larger than 99%. However, this is not the only contribution to background.

Electron initiated showers cosmic electrons or secondary electrons in the atmosphere also produce electromagnetic showers. This background is even subtler compared to hadronic background because an electron–initiated shower is pretty indistinguishable from a pure γ–ray one. Fortunately, the electron flux is smaller than γ–ray, at least for energies larger than 100 GeV.

The muons produced in hadronic showers are extremely penetrating and can easily reach the ground. Muons are almost completely rejected with the use of stereoscopic observation and partly by image analysis. However they are useful tools for calibrating each single telescope in an array [Strazzeri et al., 2013].

1.3.1 AIR SHOWERS (AUGER, ARGO)

The development of ground-based gamma-ray astronomy is closely linked to the study of cosmic rays and cosmic ray air showers.

Cherenkov radiation associated with large cosmic ray air showers was first detected in 1950s [Galbraith & Jelley, 1953] and the possibility of using this phenomenon to study gamma-rays initiated showers led to the development of a number of dedicated facilities in the 1960s. This effort was boosted by the apparent detection of a gamma-ray signal from the black-hole binary Cygnus X-3 by both particle air shower arrays and atmospheric Cherenkov detectors. Some experiments directly detect the charged component of the atmospheric shower. Water tank detectors distributed over a large area permit the detection of Cherenkov photons produced by shower in the water. The direction of the primary event can be calculated to about one degree accuracy by the analysis of Hillas ellipsoids. The energy threshold of Extensive Air Shower (EAS) detectors is at the best in the 0.5-1 TeV range [De Angelis et al, 2008].

A well–famous representative of this technique is the Auger[9] experiment in Argentina. Auger combines the two detection methods and it is composed by two different detection arrays. The first system consists of 1600 particle detector stations that form a giant grid, covering about 3000 square kilometres. The detector station is about 1.5 km apart, each one an 11000 litres tank filled with pure water.

Figure 26: ARGO Observatory (Tibet).

[9] https://www.auger.org/index.php/science/

Shower particles from a high-energy cosmic ray reach several stations at the same time producing Cherenkov light in the water. Computers at the data centre combine the measurements of the number of particles and their time of arrival at each station to determine the direction and energy of the original cosmic ray that set off the shower. A second system detects fluorescence light caused by the collisions of shower particles with air molecules in the troposphere. The total amount of light depends on the number of particles in the shower and, in turn, on the energy. The shape and direction of the light trace help determine the cosmic ray's direction and indicate what kind of particle the original cosmic ray might have been.

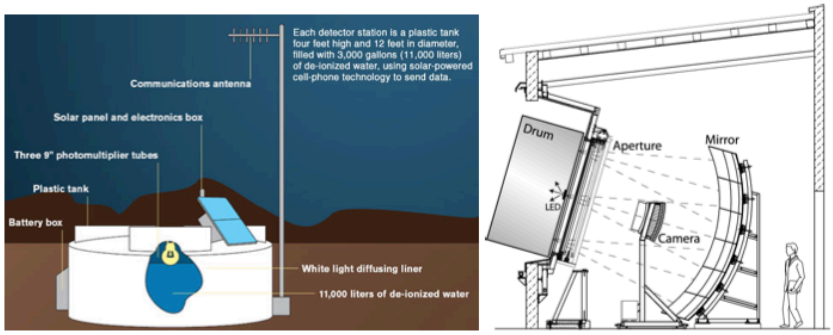

Figure 27: Sketch of one of Pierre Auger surface detectors (left); a fluorescence telescope (right)[9].

In the science plane of Auger Observatory[10] some of main topics of investigation are:

- energy spectrum of cosmic rays;
- the upper limits for the photon flux at above 10 EeV (10^{18} eV);
- composition of cosmic rays;
- UHE anisotropy;
- neutron sources;
- large scale anisotropy of cosmic rays.

The ARGO-YBJ experiment[11] (Astrophysical Radiation Ground-based Observatory Yangbajing) is located in Tibet (P.R. China), 90 km to the north of Lhasa. The aim of this

[10] www.fnal.gov/directorate/OPMO/Programs/Auger/DirRev/2011/12_15/Docs/Plan_8DEC11C1.pdf

[11] http://argo.na.infn.it/

experiment is to study cosmic rays, mainly cosmic gamma-radiation, at an energy threshold of ~100 GeV, by means of the detection of small size air showers.

A fully developed study of gamma-ray astronomy requires a telescope that identifies transient emissions and performs a systematic search of steady sources. In order to detect energies < 1 TeV it is needed to use an unconventional air shower array. At these energies the number of particles reaching the ground is too small for reconstructing the shower parameters with standard air shower arrays, made of several detectors spread over large areas which sample only a small percentage (< 1 %) of the shower particles. Since this kind of detectors triggers on shower size, it can operate at lower energies if it has the ability to detect small showers.

1.3.2 IMAGING ATMOSPHERIC CHERENKOV TELESCOPES

Cherenkov telescopes are designed with the aim to detect the Cherenkov light produced in the air shower induced by the primary γ-photon in the atmosphere, and not directly the gamma photon flux.

As any other optical or radio telescopes, an Imaging Atmospheric Cherenkov Telescopes (IACT) consists of three basic elements: a mechanical tracking system, which compensate the Earth's rotation, a collecting surface, which gathers the incident electromagnetic radiation and focuses it, and a receiver element, which converts the collected light in a recordable image of the observed field of view.

The technique of observation is referred as imaging because of the study of the image of the shower at the focal plane.

Light emitted in the Cherenkov cone reaches the ground within a circle of 100 m to 150 m radius depending on the height above sea level of the detection system.

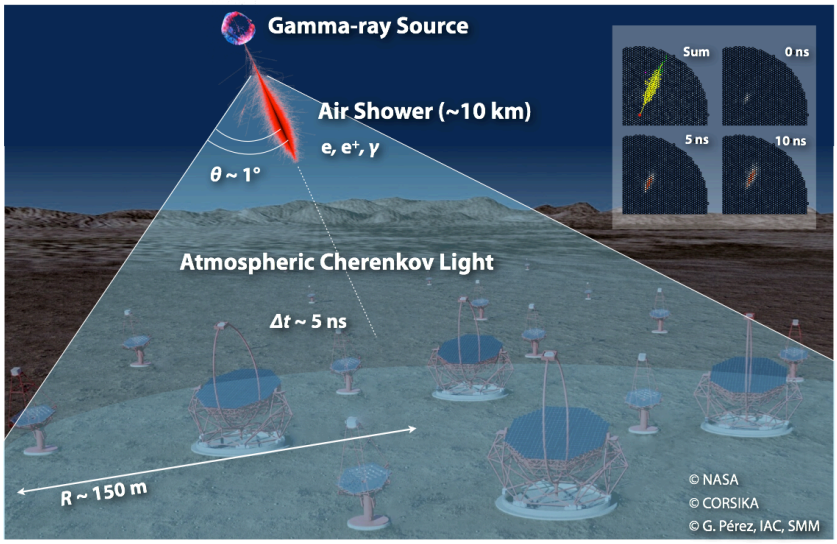

Figure 28: Pictorial representation of IACT observing a Cherenkov event.

Multiple scattering angles of shower particles near the Cherenkov threshold are comparable to the Cherenkov angle, resulting in a more or less uniformly filled light pool, with typically 10 detected Cherenkov photons per TeV shower energy per square meter of optical effective area. An optical telescope pointing to the source and located within the illuminated footprint of the shower can detect the air shower against the background light of the night sky, provided the camera is sufficiently fast to integrate only the short Cherenkov flash of the order of few nanoseconds, as longer integration time would add only noise.

With increasing energy, the central density in the light pool is enhanced due to deeper penetration of showers. Triggering and image reconstruction usually requires 50 to 100 detected Cherenkov photons and sets the scale for the dish size. The pixel size of the detection system should be matched to the size of features in air-shower images; simulation studies show saturation of performance for pixels much below 0.1° diameter, close to the typical root mean square (*rms*) width of a γ-ray image at TeV energies. The asymptotic collection area for IACT is determined by the maximum impact distance for which shower images still fall within a camera and hence by the camera field of view. At 2000 m above sea level the impact distance limitation is approximately 100 m per degree of the opening angle of the camera field of view (for showers close to Zenith).

Moreover, the measurement of the Cherenkov light provides a good indicator of the energy absorbed in the atmosphere, which is in fact acting as a calorimeter. Therefore, the

total amount of light contained in the image gives the energy of the primary particle. In addition, orientation and shape of the image also provide information on the incoming direction of the primary particle.

Cherenkov telescopes used to record these images are essentially rather simple devices, consisting of a large, segmented optical flux collector used to focus the Cherenkov light onto an array of fast photo-detectors. The optical specifications are not so strict; an optical point spread function width of typically $\sim 0.05^{\circ}$ is adequate. Cherenkov images of air showers are recorded at a rate of a few hundred Hz, and analysed offline.

There are quite a few different constraints that influence some design parameters, in comparison to optical telescopes [Doro, 2009].

Although in both cases the techniques are useful to study very distant objects, the light detected at their focal planes is very different. In cases of optical astronomical observations one observes stellar light, which originates approximately at infinity. In the case of VHE gamma-astronomy one detects Cherenkov light emitted by an extended air shower initiated by gammas in the atmosphere, i.e. from a "close by" (5-20 km) region with a diffuse transverse extension and a typical length of a few km. The Cherenkov light is emitted with a small angle off the shower particle tracks, therefore the single photons do not point directly to the source like in optical astronomy. Its position has to be determined by a complex shower image analysis. Multiple telescopes in an array, simultaneously observing the Cherenkov image of a single shower, observe it from different angles, and the parallaxes images allow stereoscopic reconstruction of the parameters, increasing the accuracy of the reconstruction in terms of angular and energy resolution and of background rejection.

In optical telescopes the mirror precision is of the order of arcsec, and can almost reach the diffraction limit in cases of adaptive optics. In IACT the observation of a "near" extended object allows for a mirror of lower optical quality and of a segmented construction, which may be composed of many small panels and therefore, less costly mirror facets that can even be staggered. Converted to the point spread function (PSF) requirements these conditions show that IACT mirrors can have a factor 100 – 500 worse PSF than in the optical telescopes. The PSF of the mirror facets typically is about 0.02° and that of the overall mirrors 0.05°.

The tracking precision must be highly precise for optical telescopes. The tracking and stability requirements for IACT are much less demanding compared to those of optical telescopes. Modern IACT achieve a pointing resolution from single showers of 0.01° – 0.1° (energy dependent).

The Cherenkov light flux from VHE showers is extremely low. Therefore, very large mirrors are desirable and the construction of the telescope should minimize the loss of photons in the optical system and their conversion into photoelectrons. The overall photon detection efficiency for state of the art IACT is about 10 - 15% when averaged over the spectral range between 290 and 600 nm.

In order to record the shower image in Cherenkov light one needs a "wide field" camera of at least 3 – 5° field of view (FOV). For observing significant sections of the sky one would in principle need an even wider field camera but this is very difficult to achieve. The use of Schmidt optics is not technically feasible while the use of a secondary mirror could be very costly. The optical image quality at the edge area of the 3–5° FOV camera should not be degraded too much. This requires a rather large f/D > 1) in cases of single mirror optics by using phototubes as detects. As cameras can be quite heavy, a strong and heavy camera support is needed, and consequently the structure has to be anchored to the mirror support dish resulting often in a large local mirror deformation.

In IACT the light sensors must have an ultra-fast response, of the order of a nanosecond, to reduce as much as possible the large Night Sky Background (NSB), as well as provide some information about the timing structure differences in showers originating from different types of incident particles, while in optical telescopes sensors can integrate source photons over rather long times but the spatial resolution must be high. State of the art IACT have pixels ranging between 0.05° – 0.2° diameter; therefore, a PSF of similar size is sufficient. This allows for a considerably cheaper mirror construction. For instance for CTA, a production cost of 1-2 kEuro per square meter is foreseen, much less than in the optical where higher accuracy is required.

Due to their very large dimension IACT, have no protective dome. They are constantly exposed to the atmosphere, to wind and rain, temperature and intense sunlight and suffer aging much more than optical telescopes. The reflectivity of the mirror surface is particularly affected by the impact of constant exposure to the ambient (see details in Chapter III).

Two main parameters characterize an IACT: sensitivity and energy threshold. Sensitivity is defined as the minimum detectable γ-ray flux in a given number of observation hours (usually defined as a 5σ excess during 50 hours of observation time). Most modern instruments use multiple telescopes to image the air-shower from different viewing angles for improved reconstruction of γ-ray direction and rejection of cosmic ray background and to apply a coincidence requirement rejecting single-telescope triggers caused by cosmic ray muons with impact points close to a telescope mirror, or by night sky background.

Telescope spacing needs to be large enough to provide a sufficient baseline for stereoscopic measurements, but small enough that multiple telescopes fit within the Cherenkov light pool; the exact spacing tends to be uncritical within a range of about 70 m to 150 m. The "effective detection area" of a Cherenkov telescope is therefore given roughly by the area of the Cherenkov light pool, about 50000 m^2.

The stereoscopic technique has become the standard for all current and future installations. With a single telescope providing a single view of a shower, it is difficult to reconstruct the exact geometry of the air shower in space. To overcome this problem, multiple telescopes are used observing the shower from different points and allow a stereoscopic reconstruction of the shower geometry [Hofmann et al., 1999]. In the following we will rapidly review the past, present and future IACT.

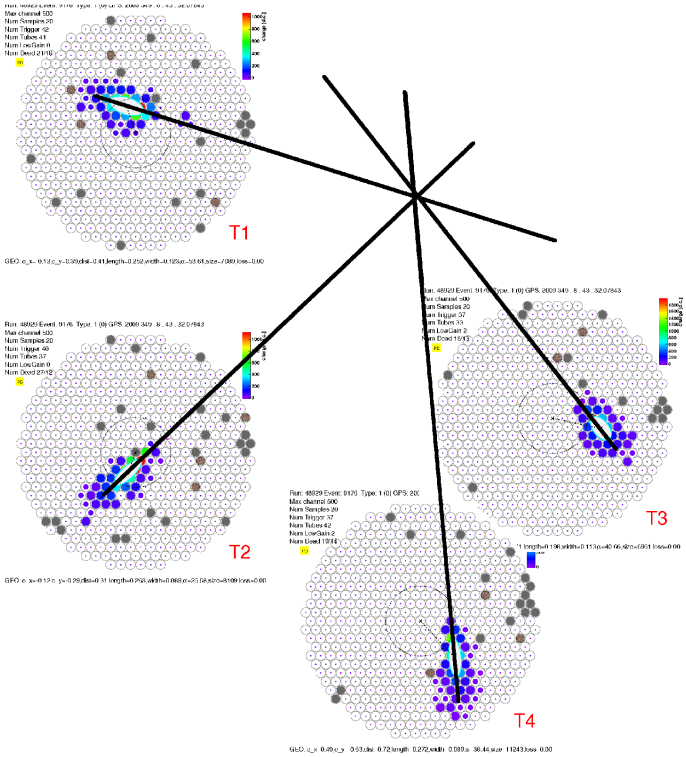

Figure 29: Example of stereoscopic detection of a gamma photon with the four VERITAS telescopes.[12]

1.3.2.a Past: WHIPPLE, HEGRA

The IACT technique for the detection of VHE gamma rays (in the energy range 100 GeV - 10 TeV) was first pioneered by the Whipple experiment since 1985. The Whipple 10 m gamma-ray telescope is located at the Fred Lawrence Whipple Observatory in Southern Arizona in the United States. This telescope has been in operation since 1968 and detected the first TeV gamma-ray source, the Crab Nebula in 1989 [Weekes et al., 1989]. The first result of Crab detection was followed by the discovery of the TeV emission from the first extragalactic source (Mrk 421), showing that acceleration processes are taking part in AGNs too. The third source, discovered in 1996, was still an extragalactic object (Mrk 501) that showed a violent flaring activity. In 1998 the Whipple Collaboration expanded and became the VERITAS Collaboration, described in the next section.

[12] www.nevis.columbia.edu/particle/veritas.html

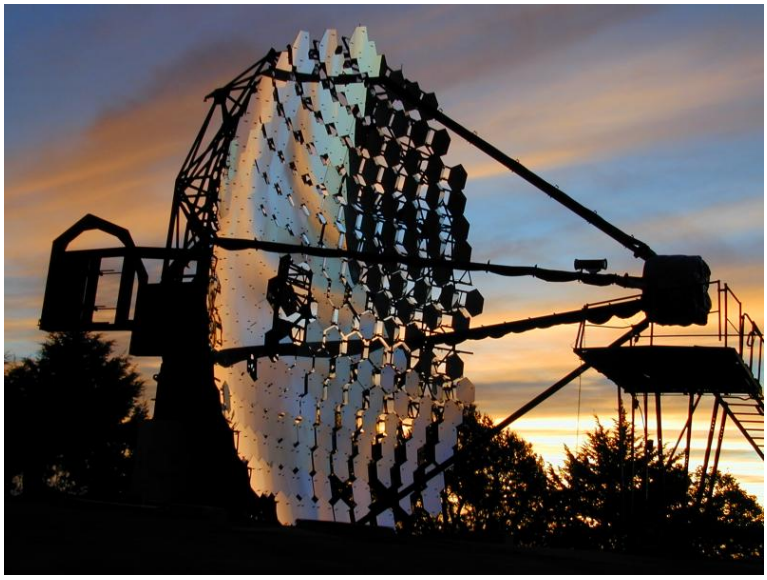

Figure 30: The WHIPPLE Telescope at the Fred Lawrence Whipple Observatory, Southern Arizona (US).

The HEGRA[13] (High Energy Gamma Ray Astronomy) Telescopes took place on the Canarian Island of La Palma in 90s. These telescopes are part of the planned system of five placed at the corners of a square, 75 m long, and one in its centre. The full Cherenkov Telescopes system consisted of 5 identical telescopes having 8.5 square meters mirror reflector area.

The stereoscopic imaging technique, pioneered by HEGRA, provides a simple geometric reconstruction of the shower: the source direction is given by the intersection of the shower image main axes in the camera, and the shower impact is obtained in a similar manner. The energy is then estimated from a weighted average of each single telescope energy reconstruction [Mirzoyan et al., 1994; Hofmann, 1999].

1.3.2.b Present: H.E.S.S., MAGIC, VERITAS

There are currently three major imaging atmospheric Cherenkov telescope systems in operation. Cherenkov Telescope systems like H.E.S.S., MAGIC, and VERITAS represent the second generation of IACT observatories for the ground-based gamma-ray astronomy.

[13] www.mpi-hd.mpg.de/hfm/CT/CT.html

MAGIC and VERITAS (in the northern hemisphere) and H.E.S.S. (in the southern hemisphere) allow imaging, photometry and spectroscopy of sources of high-energy radiation. They are typically working in an energy range spanning between 50-100 GeV to several tens of TeV. The performance of these telescopes is typically characterized by the sensitivity to detect VHE sources with an energy flux down to 10^{-13} erg · cm^{-2} · s^{-1} in 50 hours of observation time. This corresponds to a minimum detectable luminosity of $L_{min} \sim 10^{31}$ erg · s^{-1} for a galactic source at a distance of 1 kpc or $L_{min} \sim 10^{41}$ erg · s^{-1} for an extragalactic source at a distance of 100 Mpc. The angular resolution of each reconstructed primary γ-ray is typically better than few arcmin [Canestrari, 2009].

A large class of sources was detected at GeV-TeV energies both galactic (e.g. Galactic Center, Pulsar Wind Nebulae, Pulsars and Binary Systems) and extragalactic (e.g. Blazars, radiogalaxies, star-forming galaxies)

H.E.S.S.[14] is a stereoscopic system of IACT, where multiple telescopes view the same air shower [Hofmann, 2001].

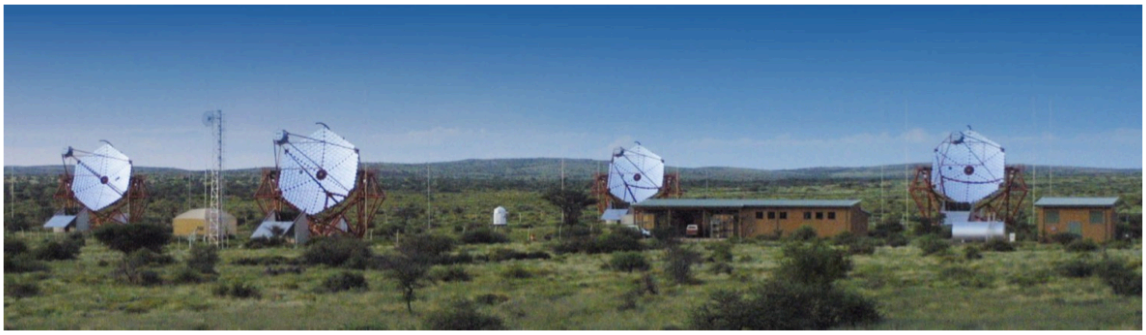

Figure 31: H.E.S.S. Telescopes Array, Namibia Desert.

The name H.E.S.S. stands for High Energy Stereoscopic System, and is also intended to pay homage to Victor Hess. It investigates cosmic gamma rays in the 100 GeV to tens of TeV energy range [Aharonian, 2006]. HESS is located in Namibia, near the Gamsberg Mountains, an area well known for its excellent quality of the site. The first of the four telescopes of phase I of the H.E.S.S. project went into operation in summer 2002; all four were operational in December 2003. In Phase II of the project, a single huge dish with about 600 m^2 mirror area has been added at the centre of the array (2012), increasing the

[14] www.mpi-hd.mpg.de/hfm/HESS/pages/about/telescopes/

energy coverage, sensitivity and angular resolution of the instrument. The four HESS telescopes are arranged in form of a square with 120 m side length, to provide multiple stereoscopic views of air showers. The telescope spacing represents a compromise between the large base length required for good stereoscopic viewing of the showers, and the requirement that two or more telescopes are hit by light generated by a shower. A larger spacing would make increasingly unlikely that multiple telescopes are illuminated simultaneously. The diagonal of the square is oriented North-South. The instrument allows scientists to explore gamma-ray sources with intensities at a level of a few thousandths of the flux of the Crab Nebula (the brightest steady source of gamma rays in the sky). Due the stereoscopic observing mode only air showers which generate images in at least two telescopes are recorded [Holder, 2012].

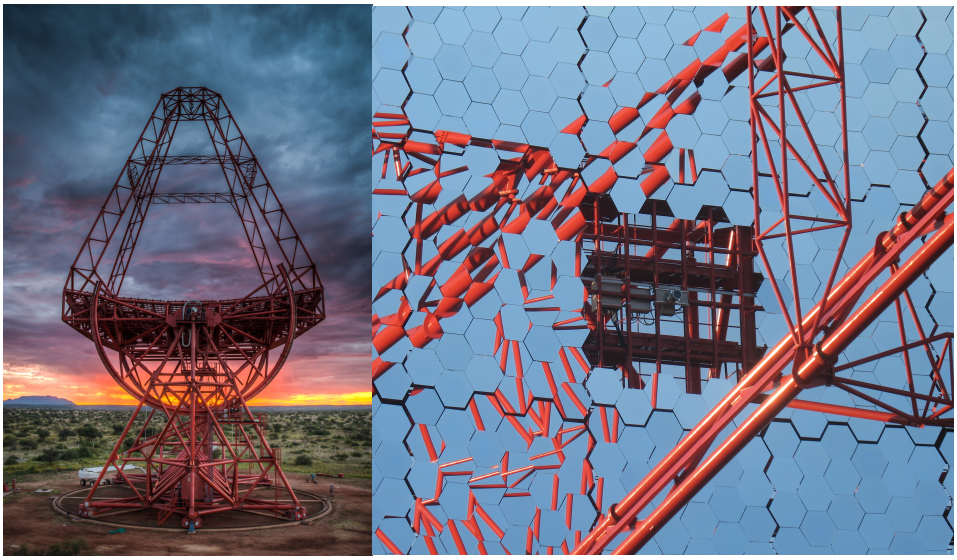

Figure 32: The 28 m Hess II Telescope. At right a detail of mirrors before alignment.

VERITAS[15] (Very Energetic Radiation Imaging Telescope Array System) is a ground-based γ-ray observatory located at the Whipple Observatory in southern Arizona. It is an array of four 12 meters reflectors deployed such that they have the highest sensitivity in the Very High Energy band (50 GeV - 50 TeV), optimized for the highest sensitivity to point sources in the 100 GeV -10 TeV band when the stereoscopic imaging technique is employed [Weekes et al., 1997; Finnegan, 2012].

[15] http://veritas.sao.arizona.edu/

Figure 33: VERITAS Telescope Array (Arizona, USA)

MAGIC[16](Major Atmosheric Gamma-ray Imaging Cherenkov) is one of the largest Imaging Atmospheric Cherenkov Telescope systems, situated on the Canarian Island La Palma, at 2245 m a.s.l. MAGIC is a system of two IACT. MAGIC I and II are two telescopes with 17 m primary mirror surfaces built at a distance of 85 meters from each-other. MAGIC I is operative since 2003, and MAGIC II since 2009. They have been realized by a collaboration of several institutes, mainly German, Italian, and Spanish. The telescopes work in stereoscopic mode in detecting Cherenkov showers [Lorentz, 1997; Doro, 2009]. The energy range of the detection is in a band ranging from 50 GeV up to several tens of TeV [Aleksić et al., 2015].

Figure 34: The MAGIC telescopes on top of the Taburiente Volcano at La Palma, Canary Islands, Spain (foreground). Telescopio Nazionale Galileo and Gran Telescopio Canarias (background) [Courtesy R. Canestrari].

[16] https://magicold.mpp.mpg.de/

The MAGIC Telescopes and their optical specifications will be discussed in details in the next chapter.

1.3.2.c Future: CTA and ASTRI

The Cherenkov Telescope Array[17] (CTA) is the ambitious international next-generation facility for VHE gamma-ray astronomy and astrophysics. The design of this new research infrastructure is implemented by an international collaboration with more than 1000 members from 27 countries in Europe, Asia, Africa and North and South America.

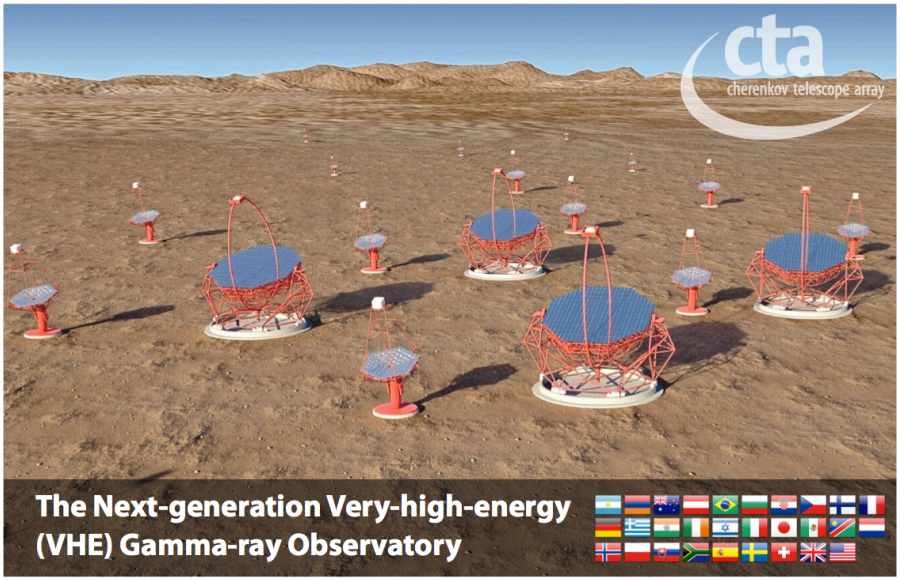

Figure 35: Rendering of Cherenkov Telescope Array Consortium.

CTA has the aims to provide a sensitivity of a factor of 10 higher than current instruments, extend the energy band coverage from below 50 GeV to above 100 TeV, and improve significantly the energy and angular resolution to allow precise imaging, photometry and spectroscopy of sources [Actis et al., 2011].

To achieve this goal, a design of an extended array composed of nearly 100 telescopes of large, medium and small dimensions is under development. The increasing detection area

[17] www.cta-observatory.org

compensates the decrease in the flux of very high-energy gamma rays with increasing energy.

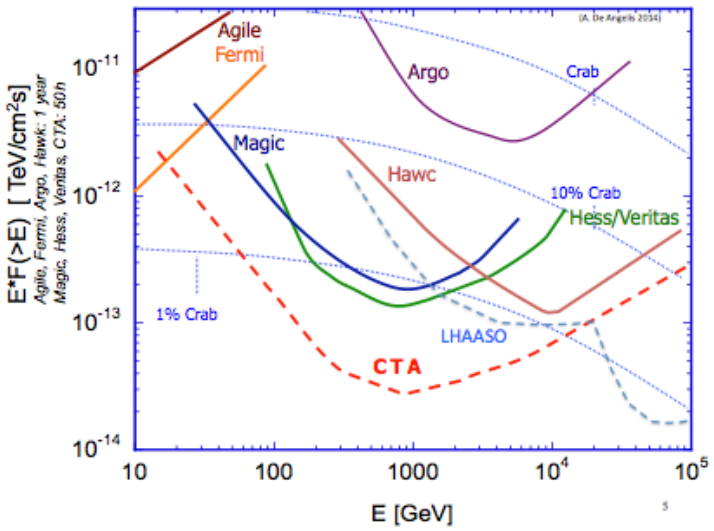

Figure 36: Sensitivity of some present and future HE gamma detectors, measured as the minimum intensity source detectable at 5 σ. The performance for EAS and satellite detector is based one year of data taking: for Cherenkov telescopes it is based on to 50 hours of data [De Angelis, 2014].

CTA is planned to include two sites, one in the northern and one in the southern hemisphere, thus assuring full-sky coverage. The main one in the southern hemisphere will cover the central part of the Galactic plane and the dominant fraction of Galactic sources. It will be designed to cover the full energy range. A second complementary northern site will be mostly targeted at extragalactic astronomy, and primarily devoted to the study of AGNs, cosmological galaxies, star formation and evolution, not requiring coverage of the highest energies. Determining the arrangement and characteristics of the CTA telescopes in the two arrays is a complex optimization problem, balancing cost against performance in different bands of the spectrum.

The basic concept for this kind of telescopes array is shown in *Figure 37* where are visible three different rings.

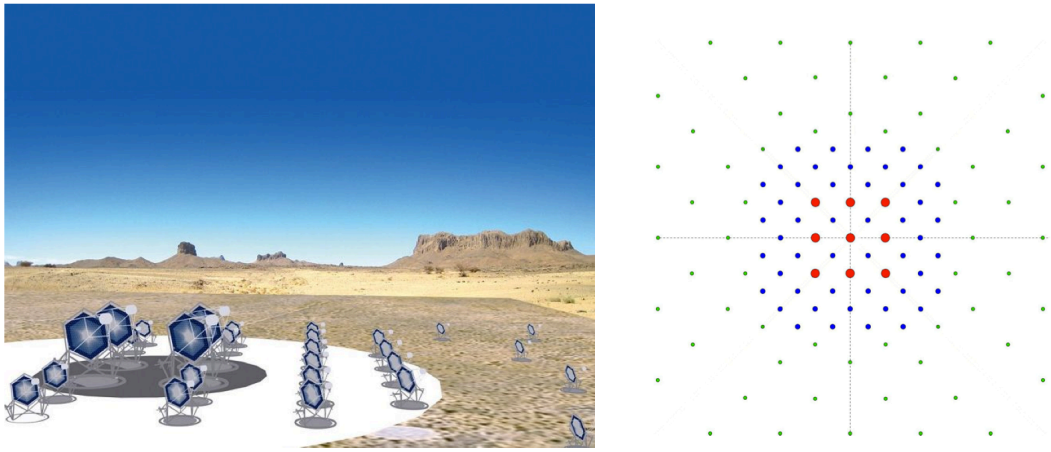

Figure 37: Conceptual array layout with three different classes of telescopes (not to scale).

The central part of this area will be composed by Large Size Telescopes (LST, diameter ~ 23 m) monitoring the sky in the lower energy band (10 GeV - 100 GeV) over a detection area of one square kilometre fraction.

An outer ring of several hundreds meters radius will be composed of Medium Size Telescopes (MST, diameter ~ 12 m) for the medium energy band (100 GeV - 10 TeV range) over about one square kilometre.

The last external ring, having a diameter of about 1 km will be filled with Small Size Telescopes (SST, diameter ~ 4-6 m, 10 TeV - 100 TeV range) installed on the CTA southern hemisphere site over up to 10 square kilometres.

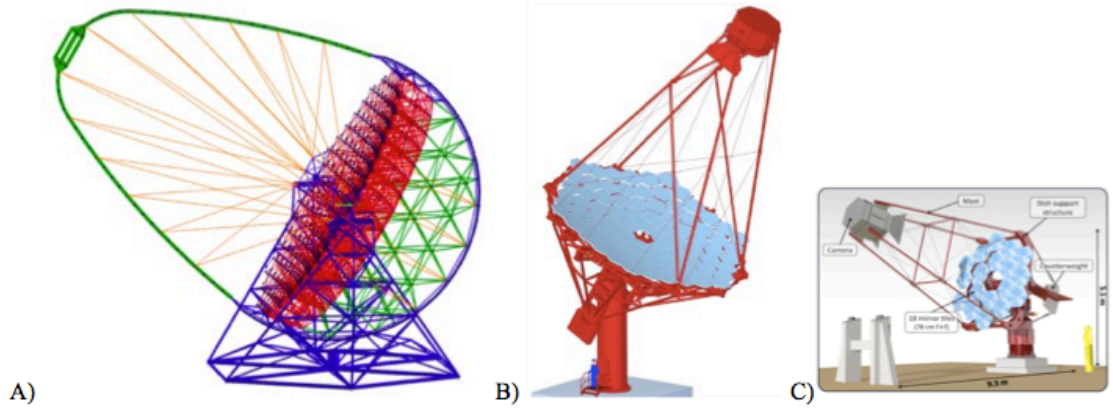

Figure 38: Single-dish telescopes being developed for the CTA arrays. A) Large Size Telescope (LST); B) Medium Size Telescope (MST); C) Small Size Telescope single mirror (SST-1M) [Credits: Pareschi et al., CTA Consortium].

These telescopes will be designed to cover the low, intermediate and high-energy regimes, respectively, and optimized for the detection of gamma rays over almost four orders of magnitude in energy distributed over a large detection area [Canestrari et al., 2012].

The aims of the CTA observatory are to increase sensitivity in the core energy range from about 100 GeV to about 10 TeV by roughly one order of magnitude, and at the same time to expand the energy range for very high energy gamma astronomy towards both lower and higher energies. In addition, CTA would provide both significant improvements in angular resolution and the field of view over the facilities operating today, revealing finer details in the sources and unprecedented detection rates, enabling researchers to track transient phenomena on very short time scales [Hermann, 2007].

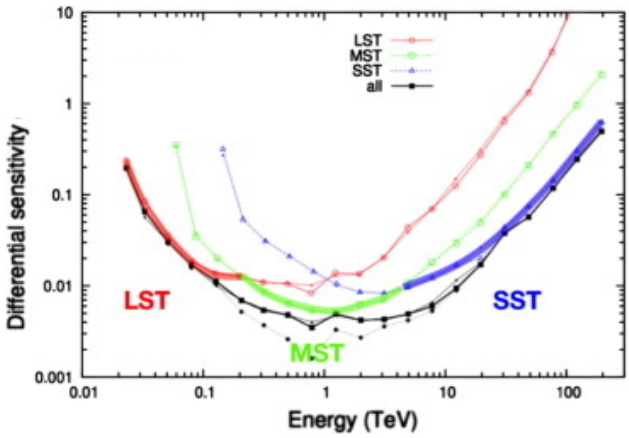

Figure 39: Differential sensitivity as combination of sensitivity of the three classes of telescopes [Lamanna, 2013].

Unlike current instruments, CTA will be operated as a proposal-driven open observatory, and will include a science data centre that will provide pre-processed data to the user, as well as tools for the common analysis techniques. This solution will facilitate worldwide collaboration in the context of simulation studies and in the processing and analysis of scientific data.

Within this framework, INAF is currently developing an end-to-end prototype of the CTA small-size telescope named ASTRI (Astrofisica con Specchi a Tecnologia Replicante Italiana), a flagship project of the Italian Ministry of Education, University and Research.

The ASTRI SST–2M prototype has been placed at Serra La Nave, 1735 m a.s.l. on the Etna Mountain near Catania, at the INAF "M.G. Fracastoro" observing station.

Figure 40: The ASTRI Telescope at Serra La Nave, September 2014. Courtesy of E. Giro.

For the first time, a dual-mirror Schwarzschild-Couder aplanatic optical design in a dual-mirror configuration has been adopted on a Cherenkov telescope, in order to obtain a compact optical configuration (F/0.5), and with a wider field of view (9.6° in diameter) [Vassiliev et al., 2007].

The proposed layout is fully compliant with the CTA requirements for the SST array. The telescope design is compact having a 4.3 m-diameter M1, a 1.8 m-diameter secondary mirror (M2) and a primary-to-secondary distance of 3.1 m [Rodeghiero, 2015].

A second challenging, but innovative technical solution consists of a modular focal surface camera based on Silicon photo-multipliers with a logical pixel size of 6.2 mm × 6.2 mm corresponding to an angular size of 0.17° [Vercellone et al, 2013].

The primary mirror M1 is segmented into 18 tiles; the central one is not used because fully obstructed by the secondary mirror M2. The segmentation requires three types of segments having different surface profiles. M1 mirror segments have been manufactured with the glass cold-shaping technology. Each segment will be equipped with two actuators plus one fixed point for alignment. Only tilt misplacements will be corrected. The secondary mirror is monolithic, and has a radius of curvature of 2180 mm and

diameter of 1800 mm. M2 will be equipped with three actuators. The third actuator also makes the piston/focus adjustment for the entire optical system available [Canestrari et al., 2011].

Although ASTRI SST–2M will mainly be a technological prototype, it will perform scientific observations on the Crab Nebula, MRK 421 and MRK 501.

Chapter II

CHERENKOV TELESCOPES AND THEIR MIRRORS

2.1 Optical Design

Cherenkov telescopes involve large collectors for very quick flashes (duration of few nanosecond) of UV light generated into the Earth atmosphere from high-energy particles or photons due to Cherenkov effect.

As for other instruments, also for IACT the main requirements to select an optical design are based on temporal resolution and spatial sampling.

Time dispersion introduced among Cherenkov photons due to different light paths should be significantly smaller than the intrinsic typical temporal spread of a Cherenkov, image of an extended air shower, of the order of 5 nanoseconds [Hillas, 1982; Heß et al., 1999]. The arrival time of Cherenkov photons on the camera should not depend on the point where they hit the reflector, but an optical path difference could be present, depending on the optical design of the telescope. Another reason to design telescopes as much isochronous as possible is to get the best effective suppression of the background.

An adequate angular resolution of the telescopes is required to reach the necessary spatial sampling of the Hillas ellipsoids and characterize them in terms of their parameters.

In order to distinguish between gamma and hadron showers the resolution required is about 0.1 - 0.2 degrees for the TeV energy range and something better for the 100 GeV energy range. As for the isochronicity, the requirement on angular resolution is more stringent for energies below 100 GeV [Mirzoyan et al., 2009]. This has an impact also on the signal to noise ratio in the shower images and on the accuracy of the reconstruction of shower parameters, resulting in a higher sensitivity and better spatial resolution in the gamma-ray skymap.

The third important parameter in the telescope design is the field of view (FoV). The choice of the field is a balancing to quantify gains and the cost and increased complexity. From the science point of view, large fields of view are of course highly desirable. On the

other hand, large FoV represent a technical challenge regarding the telescope optics. In addition a large FoV generally helps in improving the uniformity of the camera and reducing background systematics. Even in on-axis observations of a point-like source, IACT require a few degrees of FoV due to the need of containing the full Cherenkov image of the air shower, which can be longer than 1° for primary gamma rays below 1 TeV, and even more above one TeV Moreover, a wide field of view clearly enhances the possibility to observe simultaneously a wide portion of the sky, particularly crucial for the aim of producing a VHE sky survey, which is one key issue for CTA.

All single mirror configurations used up to now have a f/d ratio of the order of 1 and deliver an acceptable PSF out to 4° to 5° of field of view. With single mirror configuration larger fields of view require increased f/d ratios, in excess of 2 for a 10◦ field of view to limit of axis aberrations.

Pixel size of the camera in the focal plane is another parameter requiring careful design since the cost of focal plane instrumentation is primarily driven by the number of pixels scaling like the square of the inverse pixel size.

Related to pixel size and angular resolution is the Point Spread Function (PSF). In the ideal case, reflector quality should be such to provide a small, compared to the pixel image size, and constant spot size for a distant point source of light anywhere in the field of view of the camera. In this case *image quality* does not depend on the position of an image in the FoV [Mirzoyan et al., 1996]. This criterion is quite different from the Nyquist sampling typically used in common use optical instrumentation. A reflector should be able to concentrate light from a point source into a single pixel, implying a rms width of the PSF less than half the pixel diameter, better 1/3 of the pixel diameter. In general in an IACT design the PSF should be maintained as constant as possible along the field of view to ensure a good image reconstruction. This is particularly important in case of wide field instruments [Canestrari, 2009]. The pixel size is dependent by the typical detectors used. Up to now detectors have been photomultiplier tubes (PMT) and more recently silicon photomultipliers (SiPM). Phototubes have a typical size of the order of 25 mm (1 inch), and the last generation silicon photomultipliers are about 6 mm large. In this scenario, alternative solutions could be adopted. In fact, most modern Cherenkov telescopes use non-imaging light concentrators in front of the detectors, i.e. the Winston cones [Bernlhör et al., 2003].

The camera is basically a kilo-pixel sensor covered, depending on the optics design, from few to less than one meter-square area. Detector sensitivity must be tuned to detected Cherenkov light with sensor response that should match the peak in the spectrum around 350 nm. At large wavelengths, beyond about 550 nm, the signal to noise becomes increasingly unfavourable because of the increasing intensity in the night sky background [Canestrari, 2009]. For engineering reasons a reflector can be segmented into smaller mirrors. If the single panels are spherical and their radius is equal to the local radius of curvature of the dish, the composite surface coincides with the main shape [Schliesser et al., 2005]. This technique is a good way to realize large reflecting surfaces not necessary spherical by using smaller spherical mirrors. The production of spherical panels is simple and cost-effective.

In the next section we will describe how these concepts are adopted in the realization of the main optical schemes used for IACT.

2.1.1 DAVIES-COTTON

Davies-Cotton reflector is the most commonly used configuration for IACT and originally it was developed as a solar concentrator [Davies & Cotton, 1957]. The Davies-Cotton configuration foresees a large primary mirror dish, of the order of ten meters in diameter composed by a number of small, identical, spherical segments to achieve a very large collecting area. Davies-Cotton telescopes are relatively inexpensive to build and the alignment of the optical system is easy.

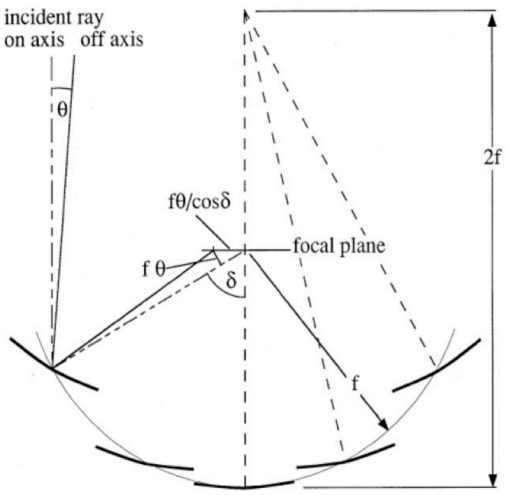

Figure 41: Davies–Cotton optical design.

In this design, the spherical mirror elements are arranged on a spheroid with the radius being just the focal length of the telescope *f*. As shown in Figure 41, the radius of curvature of the individual mirrors is constantly *2f*. The optical axes of the mirrors do not coincide with the normal of the local radius of curvature *R* (equal to the focal length of the telescope *f*), while all of them point to (x, y, z) = (0, 0, 2f) and the composite surface does not coincides with the main shape of the spheroid.

In order to find z_m-coordinate and the tilt angle θ_m of the single mirror *m,* the following relations have to be fulfilled:

$$z_m = 2f - \sqrt{4f^2 - x_m^2 - y_m^2}$$

$$\theta_2 = arctan\frac{R}{2f - z_m}$$

where the generic radius of curvature *2f* is the same for all the facets [Akhperjanianet et al., 1998]. The z_m term is often referred as staggering parameter, introduced in this configuration to focus all the panels in the same focal plane.

In this configuration there is a spread in photon arrival time in the focal plane between the light rays which hit the reflector on axis and those that hit the edge. [Schliesser & Mirzoyan, 2005]. In order to achieve a good isochronicity, considered that the maximum

time spread is an interval $\Delta T \approx 5$ns, an upper limit of diameter and focal length is fixed by the formula:

$$\Delta T \approx d^2/(8fc) \approx 5 \text{ ns}$$

[Bernlhör et al., 2003]. This leads to an upper limit of about 12 m of diameter for a DC F/0.5 configuration. In case of larger diameter, different configuration shall be to take into account.

Due to the large FoV and the single optical surface, the focal spot for these types of telescopes is not aberration-free and hence the angular resolution requirement is quite relaxed, of some arcmin.

The DC configuration shows smaller off-axis aberrations than a parabolic and spherical reflector so that it has constant and good image quality out to a few degrees from the optical axis. The predominant aberration for the DC model is the distortion.

Typical examples of Davies-Cotton layout are the 12-meters reflectors of the H.E.S.S. experiment, and the Medium Size Telescopes (MST) of the Cherenkov Telescope Array (CTA).

2.1.2 PARABOLIC DESIGN AND THE MAGIC CASE

In order to maintain the temporal structure the overall profile of the reflector for telescope with diameter larger than 12 meters, the most suitable solution is a parabolic segmented configuration.

Due to the not constant curvature radius along the parabolic profile of the main dish, this configuration foresees that the optical surface is covered by several spherical panels with different curvature radii fitting the local curvature of the parabola.

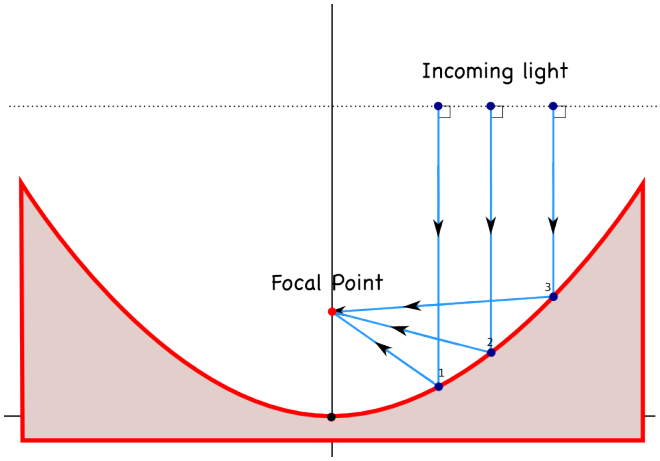

Figure 42: Parabolic configuration. This design is by definition isochronous, as the parabola is geometrically defined, given a focal point and an external straight line (the directrix), as the set of the points that are equidistant from both.

Main advantages of the parabolic configuration are:

- simple optical configuration;
- aberration free on axis;
- easy to fit with spherical panels;
- isochronicity.

Drawbacks are:

- off-axis aberrations;
- a difficult fitting of the parabolic shape with the spherical panels;
- the field of view is aberration free just close to the optical axis, while in the outer region of the FoV coma and astigmatism aberrations are relevant.

The surface of the paraboloid has a single radius of curvature only in the vertex. Excluding the centre, curvature changes in all the other positions and directions, in a not negligible amount in the outermost portion of the dish. In fact, for each position a single local curvature cannot be defined. Because curvature radii in the two perpendicular directions should be different, the facets used are spherical surfaces with a radius of curvature defined as geometrical average of the two different ones. For this reason, a spherical panel is not able to fit satisfactorily the surface, and astigmatic mirrors could fit better a parabolic surface, but their production is not a suitable solution for budget reasons.

MAGIC telescopes have been designed with a parabolic shape, with an F/1 optical configuration with a dish diameter of 17 m. The profile is fitted by 247 spherical panels with different focal lengths, to match the local curvature of the parabola.

Figure 43: MAGIC II Reflector [Canestrari, 2009].

The curvature radius of the mirrors varies from 34 meters in the centre to 36.4 meters in the outermost ring [Pareschi et al., 2008].

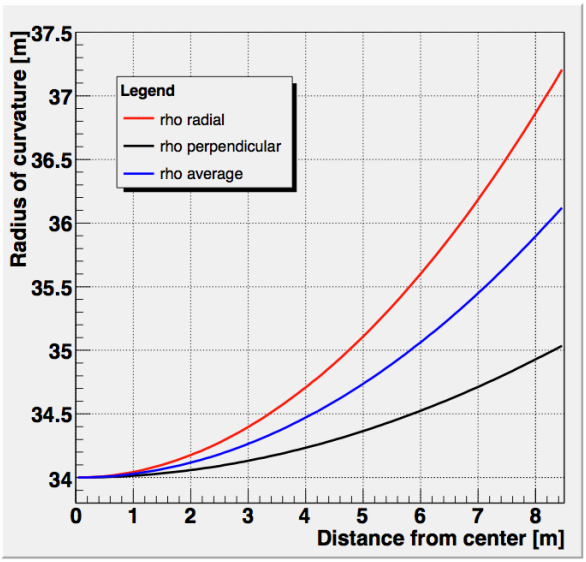

Figure 44: Principal and average radii of curvature of a paraboloid as a function of the distance from the optical axis for MAGIC telescope (on-axis incidence) [Credits: M. Doro].

Due to the effect of the coma aberrations of its parabolic design, mostly of the outer pixels in the camera are affected by image blurring.

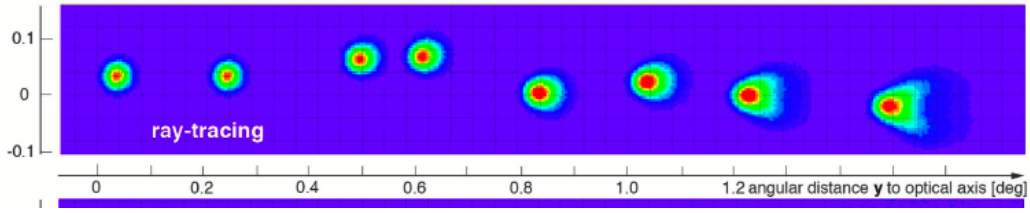

Figure 45: Image deterioration going off-axis [M. Doro, 2007].

For this reason, there is no strong justification to employ small-size pixels. For MAGIC I telescope two pixel sizes have been chosen: 396 inner pixels with an angular size ⌀ = 0.1° and the remaining 280 outer pixels ⌀ = 0.2°.

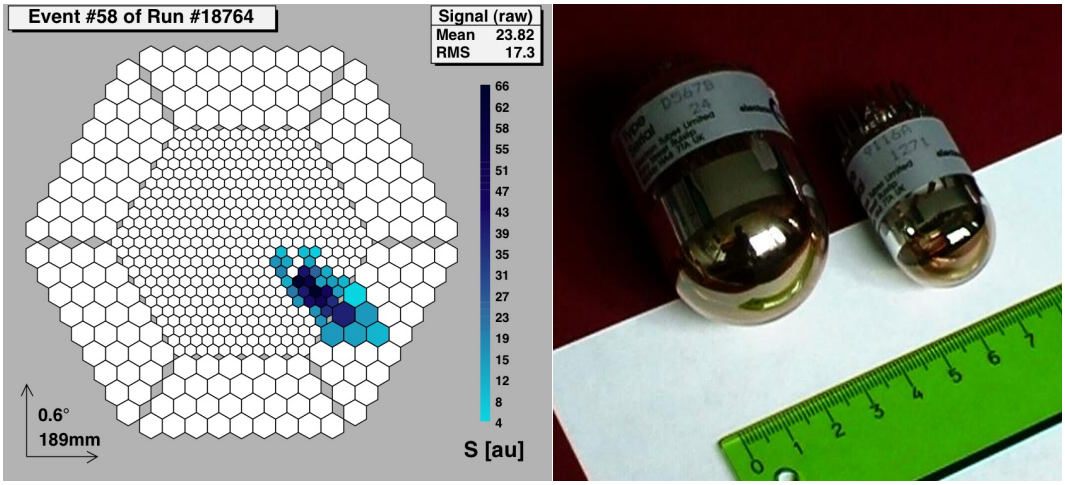

Figure 46: Pixel configuration for MAGIC camera (left); samples of phototube used to populate the focal plane of the camera (right). [Credits: M. Doro, 2007].

Whereas the mechanical structure of the telescopes is the same, different solutions have been proposed for the reflecting surfaces.

MAGIC I reflecting surface is composed by 964 square aluminium diamond milled mirrors (0.5 m x 0.5 m large), while MAGIC II is composed by 247 square mirrors (1m x 1m), with 104 glass mirrors realized with the cold-slumping technique (outer coronas). The remaining 143 (central part of the reflector, about 240 m^2 surface) have been realized in aluminium, upgrading the diamond- milling approach used for MAGIC I. The

aluminium mirrors are mounted on panels composed by four facets [Bastieri et al., 2005; Bastieri et al., 2007; Doro, 2007].

2.1.3 SCHWARZSCHILD-COUDER: A NEW DESIGN FOR THE ASTRI CASE

The principle of the Schwarzschild-Couder optics was first developed by Karl Schwarzschild in 1905 [Schwarzschild, 1905]. He proposed a two-mirror design for optical telescopes with the aim to simultaneously remove spherical and coma aberrations inherent in reflection telescopes. He found an analytic, aplanatic solution that minimizes aberrations near the optical axis. André Couder [Couder, 1926] improved upon Schwarzschild's design by adding curvature to the focal plane, which eliminates astigmatisms [Willstrop, 1984; Wyman et al., 1975].

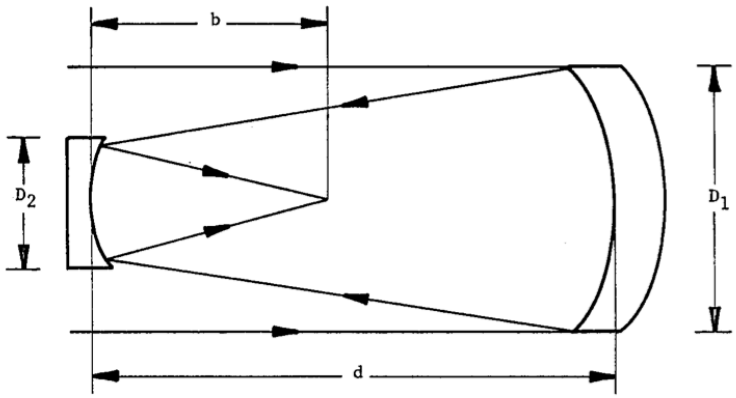

Figure 47: Geometry of Schwarzschild-Couder telescope [Wyman & Korsch, 1975].

The Schwarzschild-Couder optical configuration has ben proposed for the Small and Medium Size Telescope (SST and MST) for CTA Project. For the first time, this optical configuration has been proposed for application in gamma-ray astronomy with IACT by Vassiliev [Vassiliev et al., 2007].

The development of this peculiar design based on two highly aspherical mirrors promises wide-field, aplanatic telescopes characterized by small f-numbers and compact structures. Dual mirror solutions allow use of smaller camera pixels (~ 3-6 mm) based on Silicon Photo Multiplier technology in substitution of the larger Photo Multiplier Tubes (~ 1

inch) currently in use. The increased complexity in terms of optics manufacturing, replication and alignment is motivated by the attractive capabilities of such configuration.

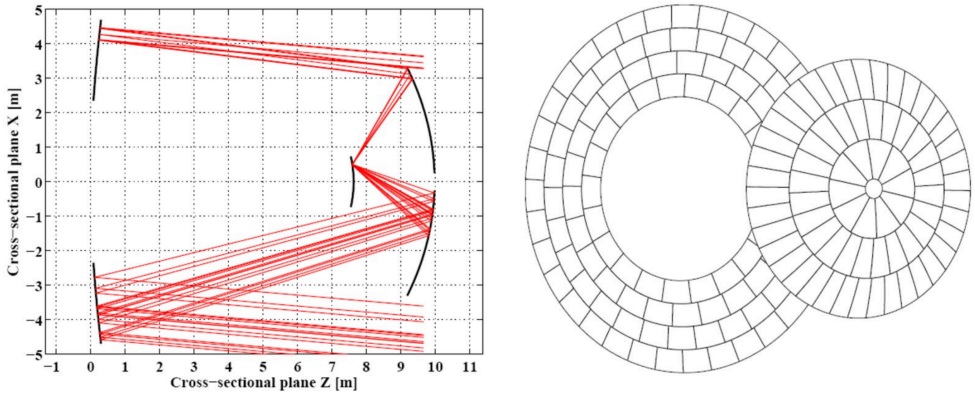

Figure 48: Scharzschild-Couder optical design proposed for AGIS [Vassiliev et al., 2007].

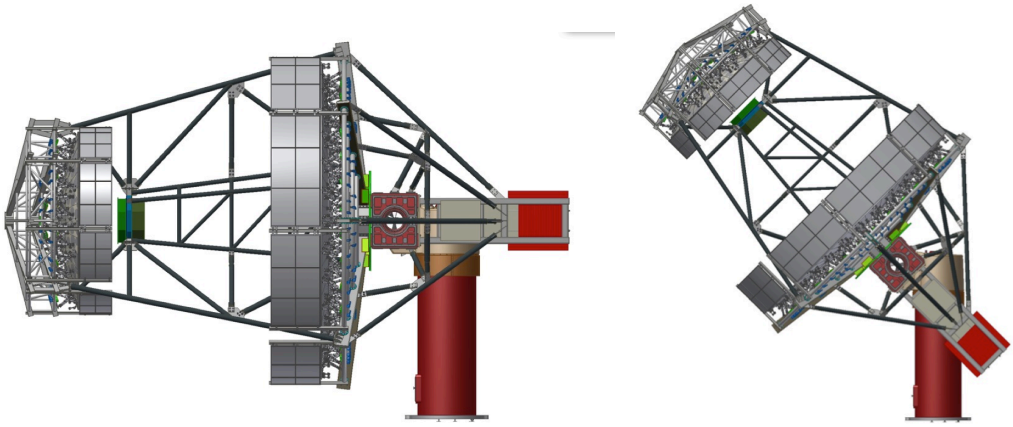

Figure 49: Schwarzschild-Couder Prototype proposed by Vassiliev for MST-CTA [Vassiliev, 2015].

The ASTRI project is the Italian proposal for the Cherenkov Telescope Array (CTA), and to implement a Schwarzschild-Couder configuration to create a wide-field and compact small size telescope prototype.

Figure 50: A rendering of the ASTRI telescope as proposed by GEC[18] Consortium.

As above described, the optical configuration foresees a double reflection; the main mirror is composed by 18 panels so to fit an optical surface of about 4 meters in diameter with a radius of curvature of about 7 m, while the secondary mirror has a diameter of about 1.8 meters with a curvature radius of about 2 m.

The optical design allows a significant reduction of the plate scale with respect to single-mirror solutions, making it compatible with compact, lightweight, finely pixelated cameras. ASTRI explores this new technology using Silicon Multipliers, with pixels having a physical size of 6.2 x 6.2 mm [Rodeghiero, 2015].

2.2 Panel production technologies

In the new technology telescopes segmented optics are used because of their capability of coupling low-cost and low-weight together with respect to monolithic mirror solution.

[18] Galbiati EIE Consortium - ASTRI Project CTA - Cherenkov telescope prototypes assembly and test plan; Doc. Ref.: ASTRI-PLA-GEC-3100-009c.

Despite the variety of the scientific targets, the wavelengths of light observed and the technology adopted, segmented optics generally require a common process. To the manufacturing process is required to deliver several panels in a time, cost and requirement frame well defined. Furthermore, each mirror is no more a unique piece like in the past but rather one in a series of identical pieces [Pareschi et al., 2009].

The Imaging Air Cherenkov Telescopes (IACT) is a class of telescopes that use segmented optics into the domain of the extremely low-cost and -weight but with the discount of moderate angular resolution requirement.

Because of high number of mirrors, it is needed to develop technologies easily transferable to industrial mass production, effective in terms of repeatability and production time, while maintaining the optical quality and cost-effectiveness requirements. For this reason proper manufacturing technologies have been developed in the framework of technical requirements of the new generation of TeV telescopes [Canestrari et al., 2010].

In the next sections the main ways used to produce Cherenkov panels will be discussed pointing out highlights and difficulties of the different methods.

2.2.1 ALUMINIUM MILLING

Aluminium milling process is one of the first techniques used for IACT. In this technique panels are a composite structure made up by a layer of AlMgSi, an aluminium honeycomb and an outer aluminium box.

These layers are assembled together with aeronautical glue in a high-pressure tank making up the so-called *raw blank*s, pre- shaped to spherical profile. The curvature is obtained by laying the raw blanks on a curved mould. Then they are polished with a diamond-milling machine.

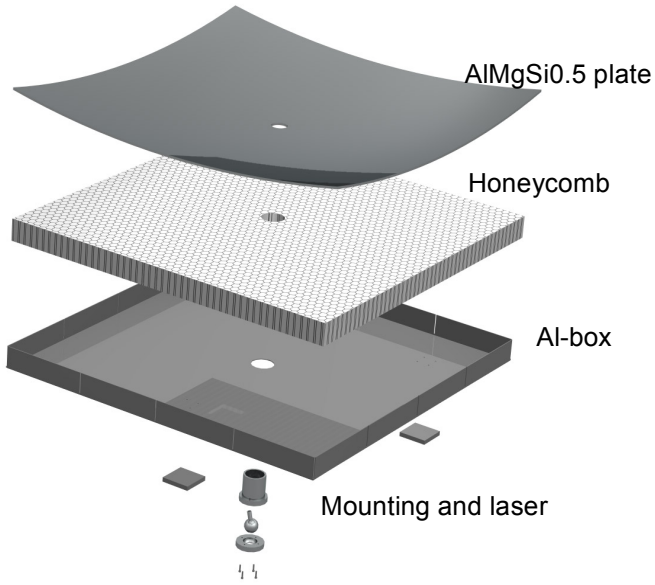

Figure 51:Exploded sketch of Aluminium diamond milled mirror [Doro, 2007].

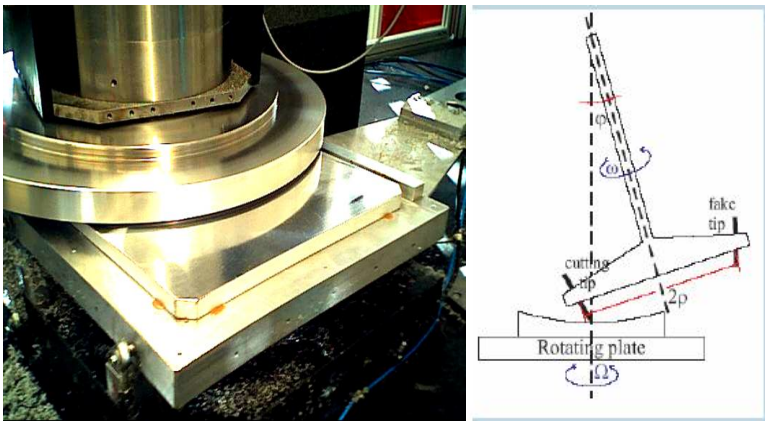

Figure 52: Diamond milling machine. A diamond tip mills the surface to give spherical shape, rotating on two axes. Mirror rotates around optical axis while machine axis rotates tilted [Credits Doro].

After polishing operation, front plates are coated with a hard and transparent protective layer (Quartz SiO_2, thickness ~100 nm) against scratches and aging. The produced mirrors weight around 18 kg/m^2 and it has been demonstrated that their lifetime is at minimum 10 years. Mirrors of MAGIC I and part of MAGIC II are realized by this technique [Bastieri et al., 2007].

2.2.2 HOT SLUMPING

Slumping is used to describe an ensamble of techniques for the forming of glass by applying heat to the point where the glass becomes plastic. The increasing fluidity of the glass with temperature causes the glass to "slump" onto a mould under the force of gravity. Through this process the glass sheet will copy with a very high degree of fidelity the shape of a mould. The mould can be used again to produce many substrates, one identical to each other, exploiting the concept of "replication process" [Canestrari, 2009].
In the hot slumping process, a thin flat glass sheet is placed above a master mould previously optically figured and polished at the desired shape. Then a suitable thermal cycle is applied (T≈650° C at constant pressure). When sufficiently heated the glass will soften enough to slump onto the mould surface and adapts to the mould's shape. When the system is cooled down to room temperature, the slumped glass shell is released from the mould and coated with the proper reflecting layer.

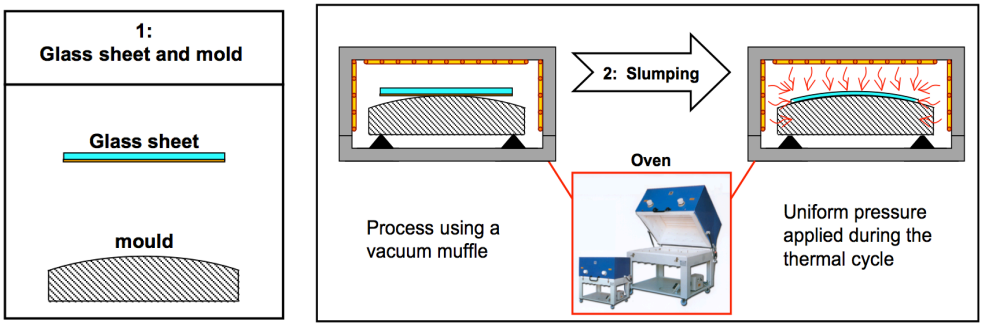

Figure 53: Steps of hot slumping process [Credits: M. Ghigo].

To ensure the full (optical) contact of the glass against the mould, a pressure is applied during the slumping process, when it reaches the maximum predetermined temperature. This gives to the process the capability to copy the overall geometry, included possible imprecisions and micro-roughness of the mould surface [Ghigo et al., 2009].
The copy process can be direct or indirect. With the direct slumping approach the optical surface of the glass is placed directly in contact with the convex mould surface.

Figure 54: Two possible setups for the hot slumping of a glass, with the direct and indirect method where the optical surface in contact (or not) with the mould [Illustration by Ghigo et al., 2009].

The dust trapped between the mould and glass during the process could be a problem and hence a clean room environment is necessary during the preparation of the process.
In the indirect approach advantages are a high uniformity of the reflecting surface that keeps the same local optical properties never touching the mould surface.
The contact between glass and mould is forced only by gravity, with no additional pressure. More the glass is thick the more inaccurate will be the copy. On the other hand, larger thickness assures stiffness and stability to the mirror. The production of high quality mirror of one-meter size could be difficult with this process.

2.2.3 COLD SHAPING

The concept of cold shaping method is to form a thin sheet of glass on a very precise mould that gives the exact curvature of the mirror, at room temperature and hence without using heat. The cold glass slumping is a method derived from a similar technique proposed for the manufacturing of X-Ray optics of the XEUS mission [Ghigo et al., 2008].
Astronomical Observatory of Brera INAF-OAB has developed in collaboration with Media Lario Technologies Company this technique for the manufacturing of stiff and lightweight segmented optics. This new method is commonly named *cold slumping*, inheriting this definition from the other well known hot slumping technique.
The cold-shaping technique has been developed over the past years with the goal to address the problems of replication of a master shape at room temperature for mass production in order to reduce both the costs and the production time, while maintaining the quality of the products. In the cold-shaping process, a glass foil copies the shape of a mould with a high degree of fidelity, in particular for low spatial frequencies. Dust and imperfections on the surface could be replicated on the mirror. The mould can be used

again to produce other identical panels without suffering evident surface deterioration [Canestrari, 2013].

This concept works considering the elasticity of the glass and it accepts small deformations without introduce other distortions. For this reason technique is suitable when using long radius of curvature (> 7 m for thickness ~1 mm). A possible effect is named spring-back and it consists in a spread of possible curvature radii from the same mould.

The process starts shaping a thin (1-2 mm thick) sheet of glass on a convex Aluminium master mould. The master typically is in aluminium and its surface is diamond milled in the same way discussed in the previous section [Pareschi et al., 2008].

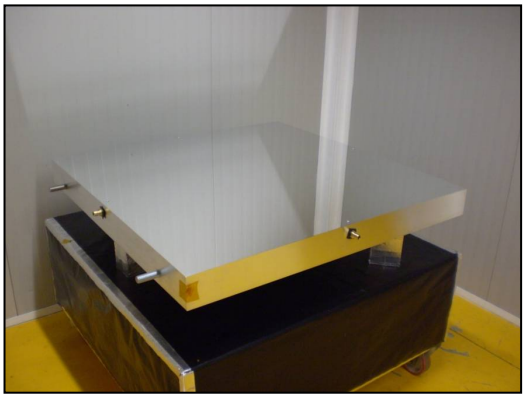

Figure 55: Aluminium Mould with spherical shape obtained with a diamond milling facility. Master used in Media Lario Technologies production and produced by the LT-Ultra Company.

Several ways are used to apply the necessary pressure to the glass foil, for example by means of a vacuum suction or weights to obtain the requested concave curvature.

The glass is glued to a honeycomb structure to provide stiffness and hence sandwiched using another glass sheet applied to the back of the panel for symmetry reasons. Quantity and curing of glue permits to tune curvature radii by the spring-back effect. The sandwich technique with honeycomb can provide panel with weights in the order of 10 kg/m^2.

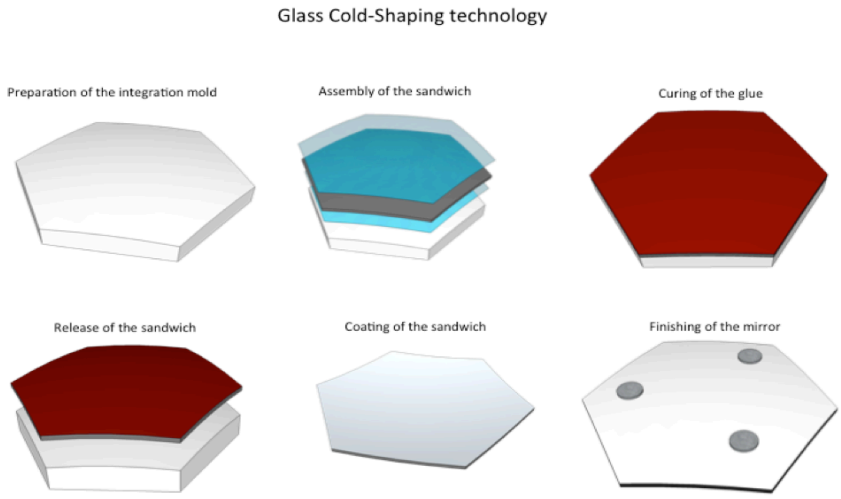

Figure 56: Main production steps of cold-shaped mirrors [Giro E., 2011].

After the polymerization of the glue, the glass surface is coated. The coating consists of two layers deposited by plasma vapour deposition. First, there is an Aluminium coating, and the latter one is a thin Quartz layer as protection against reflectivity losses and scratches (more complex recipes can be actually be used, details on coatings are discussed in the next chapter). The mirror is then finished by sealing its edges to prevent damage from water infiltration.

This is a very competitive approach for productions of mirrors for the Cherenkov telescopes with a Davies Cotton optical layout (this is the case of CTA for LST, MST and SST-1M) [Pareschi et al., 2013].

2.2.4 HOT SLUMPING WITH SANDWICH TECHNIQUE

As discussed in hot slumping section, the production of large mirrors with a high quality could be difficult. In order to overcome this problem a combination of hot slumping and cold shaping could be a good solution.

This technology is similar to the previous one but the thin glass is modelled with hot slumping before to be assembled with sandwich. In this way a small correction can be applied to the hot pre-shaped surface. Initially the procedure foresees to manufacture a

panel using the hot slumping technique to obtain an optically good thin glass shell. Due to the low thickness, this step produces a glass shell with an accurate profile but highly floppy. The mirror structure reaches the requested stiffness by means of the sandwich assembly.

The curved shell has to be frozen, then assembled and glued to a stiff substrate of Aluminium honeycomb or foamed material. On the back of the substrate it is also glued a flat sheet of the same glass [Canestrari et al., 2009].

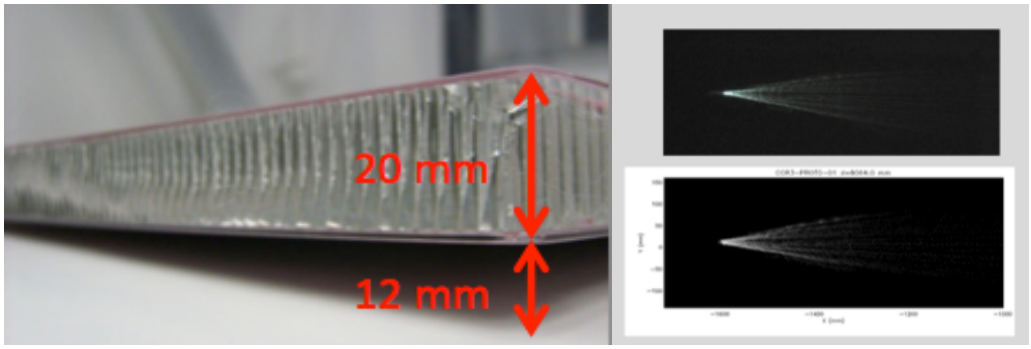

Figure 57: Left: a prototype for the ASTRI telescope primary mirror obtained with hot-slumping glass sandwich. Right: comparison between optical measurements and ray-tracing from surface measurement [Credits: E. Giro].

It is important to underline that small profile errors in the hot-slumped shell can be corrected by applying cold-shaping procedure.

Hot-slumped glass sandwich matches the good optical performances achievable on optics produced by means of the hot slumping technique with the lightweight and stiffness of the foamed material and, finally, the good structural properties achievable in sandwich-like structures [Canestrari et al., 2008].

2.2.5 OPEN GLASS-STEEL STRUCTURE

The open glass-steel structure is the technique ~~under investigation~~ developed in Padova by INFN (Istituto Nazionale di Fisica Nucleare). This technique could be a good candidate for the production of LST-CTA mirrors.

Plane glass sheets are shaped under low pressure on a diamond-milled aluminium mould.

On the rear two thick glass foils (thickness ~1.8 mm) are glued together, before being assembled with a third glass foil and the reflecting surface (2 mm thick). This mirror is mosaic-like, composed by six glass triangles, collected to obtain a hexagonal shape. Surface losses at junction of reflective elements could be considered negligible.

The relevant innovation of this method is the replacement of the honeycomb element with an open structure consisting in some tenths of stainless steel cylinders (see Figure 58) as interspacers between the rear and front glass sheets. In order to compensate pressure and humidity with external environment each cylinder is drilled with four holes (Ø 5mm). Open structure solution provides stiffness, lightweight and limit water trapping.

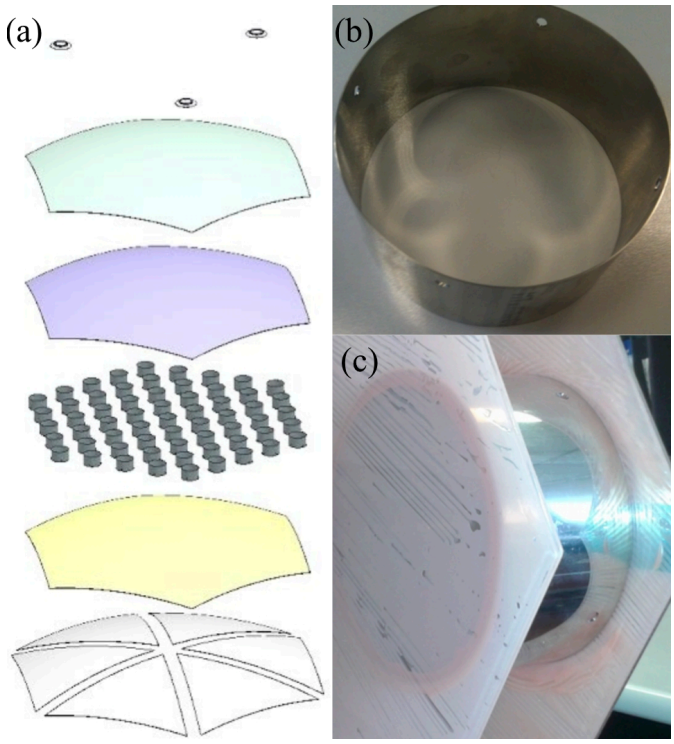

Figure 58: (a) Exploded view drawing of the open structure mirror. (b) Stainless steel cylinder. (c) Detail of assembly with glass sheets interspaced by a cylinder [Schultz et al., 2015].

The optical surface is Al/dielectric coated before the shaping and final assembling phases. Due to the requirement of coating uniformity, its application on a plane surface results easier to calibrate than on a curved shape. During the shaping phase of the optical surface a protective foil is applied, in order to limit the replication of high-frequencies errors due to dust, scratches, digs, etc. possibly present on the mould. At the end of this process the protective foil is removed. All the operations take place at room temperature.

Main advantage of this method is the lightweight (~21 kg/m^2): lower thickness than in sandwich techniques and the absence of the aluminium honeycomb allows to reduce the quantity of glue [Schultz et al., 2015].

2.3 COATINGS

Mirrors developed for Cherenkov telescopes are different from the optical ones in several aspects. First, they are not protected by a dome, therefore the mirror facets are always exposed to the environment with no protection. This makes it necessary to have a protective coating over the reflective layer of the panels. Moreover, mirror coating plays a crucial role in defining its optical response and hence its sensitivity.

The current standard (e.g. H.E.S.S., VERITAS and part of MAGIC) are glass mirrors coated on front surface with aluminium (Al). In the case of the MAGIC I and large part of MAGIC II reflector, the aluminium honeycomb structure is diamond milled and no further reflective coating is needed: only a protective Al_2O_3 layer is applied [Doro et al., 2008].

Aluminium based coatings with a single protective layer (e.g. SiO_2, Al_2O_3) on the top of the mirror is until now the most common solution.

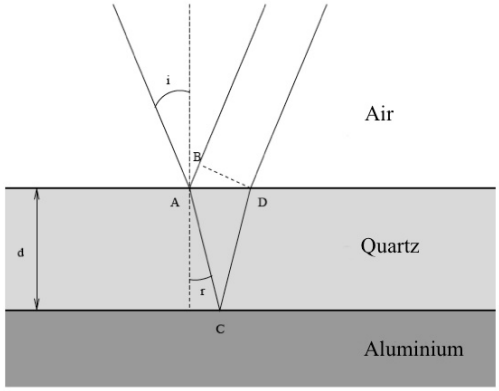

Figure 59: Light propagation in coating layers: SiO_2 + Al [Doro, 2007].

This kind of layer shows a reflectance of 80 to 90% in the range 300-600 nm (light emission peak of the Cherenkov observables). These mirrors usually lose 4-5% of their reflectance per year of observation, which requires re-coating every few years. An

important requirement is in fact keeping all optical and mechanical properties stable during for long period. On the other hand, due to the flat spectral reflectivity of these recipes, no Night Sky Background (NSB) suppression is achieved in the "red" (wavelengths >700 nm) portion of the visible spectrum. This is quite relevant for SiPMs, as these sensors are sensitive up to ~ 900 nm, in a region where NSB is dominant on a vanishing Cherenkov signal. A further drawback is the limited lifetime of the mirrors to few years. Since Cherenkov telescopes are usually exposed to severe environments without any protective dome, detachment from the substrate may occur, leading to a general reflectance drop [Bonardi et al., 2014]. However the actual ageing rate is fairly dependent on the details of the deposition process, which happens to be slower than reported in some cases. How to reach control of this behaviour is crucial and well under investigation in CTA since the Observatory is intended to have a lifetime of many decades and mirror stability is crucial not only for performance but also for keeping technical overheads and maintenance costs as low as possible.

In order to improve reflectance and durability, it is under investigation the possibility to use a three-layer protective coating (SiO_2 + HfO_2 + SiO_2) on top of Al coatings, enhancing the reflectance by about 5%. Furthermore, new dielectric coatings have been developed aiming to enhance mirror resistance to environmental impact and to extend their possible lifetime. In addition, these customized coatings reach an average reflectance up to 95% in the 300-600 nm band while at the same time they are designed to significantly lower the NSB contribution at longer wavelengths [Förster, 2013].

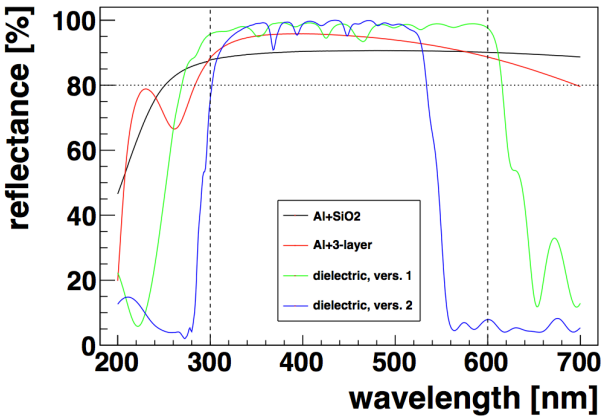

Figure 60: Comparison among the spectral reflectance of different coatings. Version 1 and 2 are referred to different designs: v.1 is optimized for the range 300-600 nm, v.2 presents a cut-off around 550 nm [Förster, 2013].

A dielectric coating consists of a stack of many alternating layers of two materials with different refractive indices, without any metallic layer. Properly optimized, this results into a pure interference filter that allows a box-shaped reflectance curve to be custom-made with > 95% reflectance in a defined wavelength range and < 30% elsewhere.

Dielectric coatings use interference of several material layers of different refraction index to achieve high reflectivity at a specific wavelength range. In addition to this, it is commonly believed that one of the advantages of dielectric coatings is durability. The main technical challenge with this kind of coating is to obtain homogeneous thickness over large surfaces. Moreover, an accurate control of the process is needed to grant homogeneity across different batches of panels. This leads to increased costs with respect to the baseline solution to cover baseline solution of quartz-overcoated aluminum coatings that have to be evaluated as well as the performance improvement.

When light passes from a dielectric material to another one, it is reflected according to Fresnel's law. The reflectance for small incident angles is equal to

$$R = \left(\frac{n_1 - n_2}{n_1 + n_2}\right)^2$$

where R is the reflection coefficient, and n_1 and n_2 respectively the refractive indexes of the first and second material [Hecht, 2002]. In a multi-layer coating design, the reflectance value depends also on the wavelength of the incident light because of interference.

For a light ray passing from one layer to a second one, the highest reflectance value is obtained for

$$\lambda = \frac{4 n_1 L_1}{cos(\vartheta)}$$

where λ is the incident light wavelength in vacuum, θ the incident angle, and L_1 and n_1 the thickness and the refractive index of the first layer.

By alternating several dielectric layers with different thickness and refraction index, it is possible to achieve very high reflectance within the desired wavelength range and very low reflectance outside of it. Furthermore, since no metallic layer is used, no deterioration due to oxidation will occur, and then the mirror lifetime is expected to be longer [Bonardi et al., 2014].

A proper tuning of the materials and of the layer thicknesses can approach closely an ideal band-pass filter, with transmittance (or reflectivity) approaching 100% in the band of interest and negligible values elsewhere [Bonnoli et al., 2013].

As said, most of the present generation of IACTs are composed by solid glass mirrors or by an aluminium honeycomb structure, with a front-coated glass substrate. The sandwich technique provides panels as sandwich structures of different materials glued together. Most of these glues cannot be heated to temperatures above 80° C without damage. Al-based coatings can be applied without heating the substrate but with only limited heat impact from the evaporation sources during the coating process. A special process is required for the dielectric coating to keep the substrate temperature below the required limit, but it needs longer coating times and therefore higher costs. In parallel, the option is being investigated to construct the sandwich with a front-coated glass sheet rather than coating the final mirror.

In the laboratory tests the three layer protective coating (SiO_2-HfO_2 -SiO_2) on top of an aluminium coating performs better than the standard Al + SiO_2 coating. The dielectric coating shows a significantly better performance. A significant problem of the dielectric coating is believed to be the increased probability of forming condensation on the reflective surface due to a much higher emissivity of the dielectric coatings in the infrared (8-14 μm).

In conclusion, both the Al + SiO_2 + HfO_2 + SiO_2 and the dielectric coating are available alternatives to the standard Al + SiO_2 coating. This aspect is under investigation within the ASTRI (and CTA) collaboration.

It is interesting to discuss the main specificity of the ASTRI SST-2M coating design. Due to the choice of Silicon Photo Multipliers (SiPMs) as sensors instead of the long-standing standard constituted by Photo Multiplier Tubes (PMT), to avoid some of the disadvantages of PMT such as the large dimensions, weight and power consumption. Photon detection efficiency of the SiPMs adopted for ASTRI prototype has a not negligible tail above 700 nm and up to 900 nm. This implies a strong contamination with the Night Sky Background light (NSB) where the Cherenkov signal is relatively dim. As shown in the Figure 61 while Cherenkov signal is dominant at low wavelengths, Night Sky Background is dominant above 700 nm.

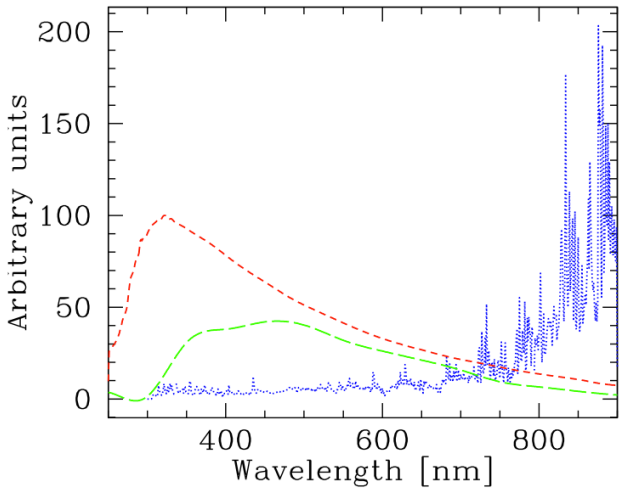

Figure 61: Comparison between the spectra of Cherenkov light (short dashed red line) and of Night Sky Background light (dotted blue line). Arbitrary units.

In order to solve this problem, it is possible the introduction of a low-pass filter, capable of filtering out the noise-dominated red portion of the optical band. Such behaviour can be obtained by means of interferential coatings deposited onto glass substrates, for instance, by means of physical vapour deposition of dielectric materials such as SiO_2, TiO_2, Ta_2O_5, MgF_2 and others. In this technique multiple layers of materials characterized by different refractive indices, are deposited onto the glass substrate with uniform thicknesses ranging from tens to hundreds of nanometers.

Chapter III

CHARACTERIZATION OF CHERENKOV MIRRORS

In order to qualify a generic optical system, it is needed to quantify some properties related to global and local features of the optical surfaces and their substrates. Such geometric and mechanical properties affect the light concentration in the focal plane of the optical system, due to the difference of the optical paths of rays impinging on different regions of the system.
In this section, we will discuss how to qualify reflecting panels to be mounted at Cherenkov telescopes.

3.1 Opto – Geometric Properties

In order to evaluate the quality of a mirror, first of all it is important to define a set of convenient measurable parameters.

3.1.1 POINT SPREAD FUNCTION

The Point Spread Function (PSF) is defined as the distribution on the focal plane of the light of a point source, imaged on the focal plane by a generic optical system.
Considering an optical system and its geometric configuration is possible to quantify the PSF by calculating the normalized intensity distribution of the point-source image. This estimation depends on diffraction-limited image in aberration-free case. Due to presence of aberrations, geometrical PSF based on ray-tracing of the optical system is commonly used.

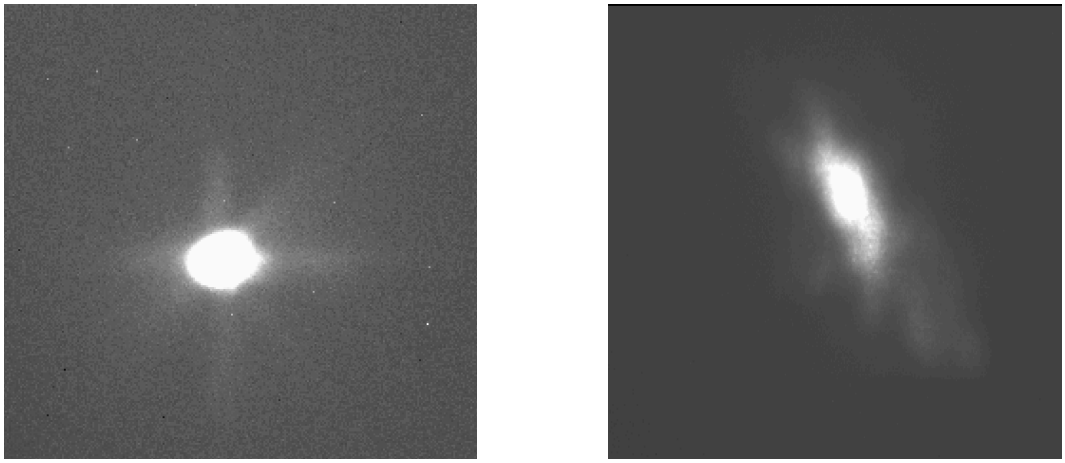

Figure 62: Examples of PSFs. Left: a PSF with evident tails due to edge effects. Right: a strongly astigmatic PSF.

The PSF size in the diffraction-limited case is of the order ~λ/D (D is the aperture diameter, and λ the wavelength of light). Conventionally, the width of the PSF is measured from the *full width half maximum* (FWHM) of the spatial distribution of the light intensity.

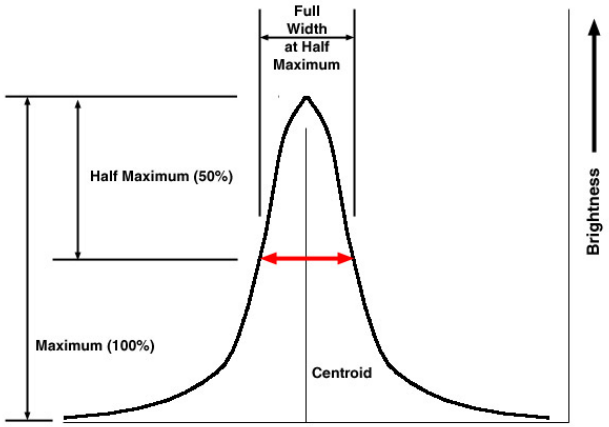

Figure 63: PSF distribution and its FWHM.

FWHM is defined as the width of the distribution of the PSF at a level that is just half the maximum of its peak. In the diffraction limited case the PSF size is λ/D. In the most general case, aberrations increase the FWHM well above this limit. A practical way to measure it is to fit with a Gaussian profile the PSF and estimate its sigma. The ratio between FWHM and sigma is about 2.3548. The drawback of this method is that irregular

PSF not always are fitted in a reliable way by Gaussian profiles. In case of regular PSF the method is highly sensitive for tracing degradations of optical performance (see chapter IV).

Due to the observation technique adopted by the Cherenkov telescopes, FWHM is not the best parameter to describe the optical performance of the system. Since the major part of the light should be contained into a single pixel of the Cherenkov camera, it is more convenient to define a different parameter derived from the PSF: the encircled (or ensquared) energy fraction (EE). EE is defined as the fraction of the total energy E in the image enclosed within a circle of radius (or square edge) *r* centred on the PSF peak [Schroeder, 1999]. R80 (or R90) is the radius of the circle containing 80% (or 90%) energy of the overall PSF. This value can be expressed both in linear and angular units; in the second case the focal length of the optical system must be known.

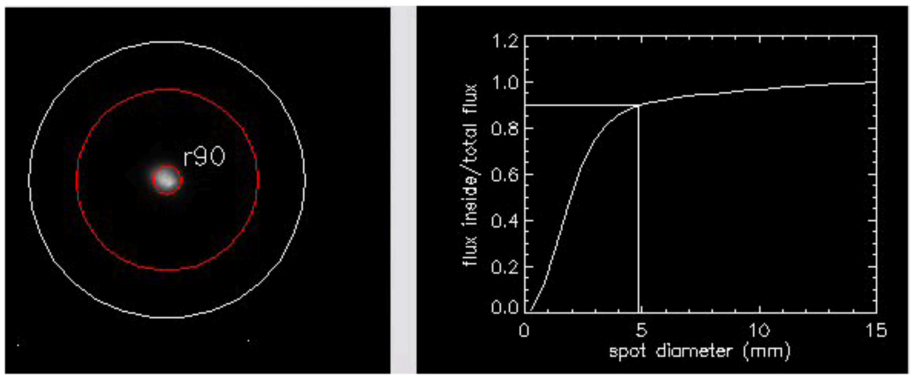

Figure 64: Example of R90 estimation and relative plot [Credits: M. Doro].

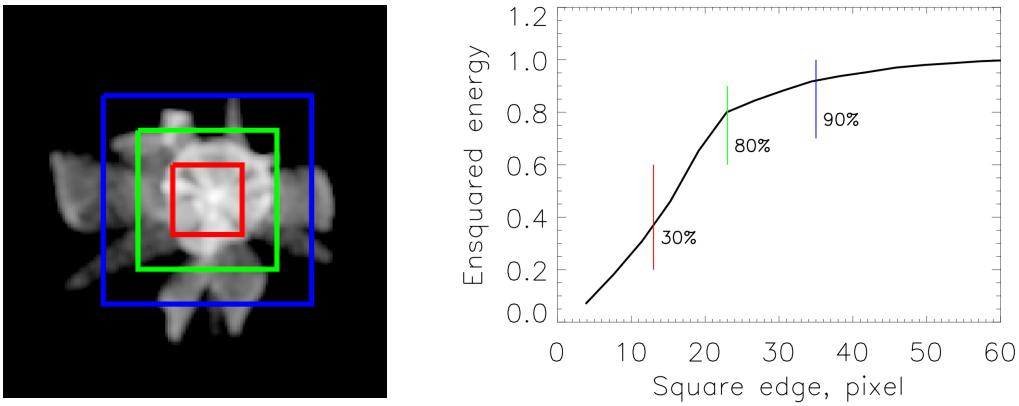

Figure 65: Example of Ensquared Energy estimation with relative plot [Credits: G. Rodeghiero].

The R80 is determined by the optical configuration, and it can be deteriorated with respect to the expected one by several factors, such as shape accuracy and roughness of the surface.

PSF of an IACT is usually larger than the one of the optical telescopes. Typical R80 values for Cherenkov mirrors are of the order of 1 mrad (a few arcmin).

3.1.2 Focal Length

To measure the focal length of a spherical mirror the *Gaussian lens formula* can be used:

$$\frac{1}{f} = \frac{1}{p} + \frac{1}{q} = \frac{1}{2R}$$

where f is the focal length of the optical system, defined as the distance of the image of a point source object place at infinite distance, $R = 2f$ and it is the radius of the sphere defining the mirror surface (namely radius of curvature *RoC*), p is the distance of a point source from the mirror vertex and q is the distance always from the vertex of the image generated by the reflection on the mirror [Born & Wolf, 1999].

This formula is valid only in the Gaussian approximation, i.e. if the mirror size is small if compared with the sphere size defining its surface and rays hitting the mirror surface define small angles with respect to the optical axis of the system. Of course these circumstances are verified in the case of spherical facets for Cherenkov telescopes where panel sizes are small in comparison with their RoC and if mirrors are illuminated from a large distance compared with their size.

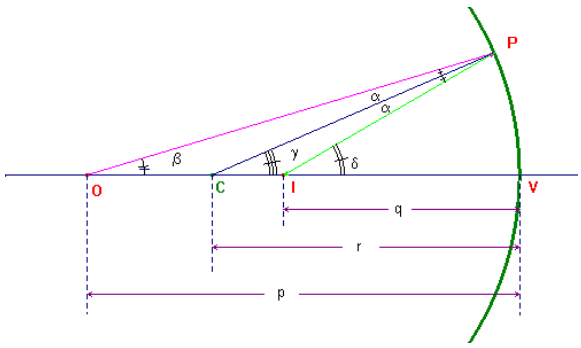

Figure 66: Optical scheme of the reflection in the spherical mirror case.

The easier way to apply the formula is to set-up the light source at a distance from the mirror vertex approximately equal to the RoC (*2f* configuration). In such a way the image produced by the mirror will be close to this position. This is a cost-effective solution that permits to qualify in relatively small places panels with quite long focal length. The drawback of this setup is that is when panels are mounted in the outer part of the dish of the telescope are not illuminated in the same conditions. For this reason to have a better qualification of the facets together with this method, often a surface shape analysis is performed as discussed in the next section.

In the case of MAGIC mirrors the PSF and radius of curvature measurements, the mirror was placed at a distance of about (the assumed radius of curvature of the mirror) and illuminated with a point-light source. The point-like light source can be simulated by a laser diode with a microscope objective and a pinhole in front. A screen is placed close to the diode, at the same distance to the mirror. The distance from the mirror and the diode was adjusted searching for the best image position [Canestrari, 2009].

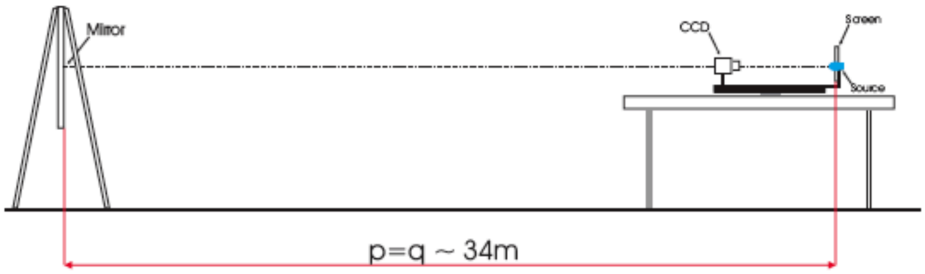

Figure 67: Optical set-up to measure focal lengths in the MAGIC panels case [Doro, 2007].

Practical realizations of this set-up will be discussed in details in the section III.4 and in the chapter IV.

3.1.3 SHAPE ERRORS

Any discrepancy from the ideal shape affects system performance in different ways. In general referring to Figure 68, surface form error falls into one of three categories, where each category represents a portion of the spatial frequency domain. Low frequency errors

(Figure 68) are irregularities in mirror surfaces and represents a macroscopic error on full aperture, while roughness looks at errors on a microscopic, sub-aperture, high spatial frequency level. Mid-spatial errors occur between the Figure and Roughness categories.

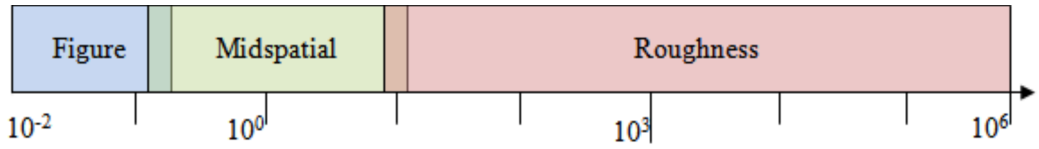

Figure 68: Classification of surface errors. Unit: [mm^{-1}].[19]

Following this classification, deviations from the original shape can be summarized:

- in case of low frequency error (~10^{-3} - 10^{-1} mm^{-1}) the radius of curvature of the panel could be modified and as consequence its focal length;
- in case of mid-frequency error (~10^{-1} - 10^{2} mm^{-1}) the mirror shows a deformation of the original pattern due to its own local shape. Consequences are deterioration in PSF and enlargement in R80 value, modifying the optical quality;
- very high frequencies errors (~10^{2} – 10^{6} mm^{-1}) influence the amount of wide-angle scatter. This aspect is typically related to surface roughness, as discussed in the dedicated section.

Low and middle frequency deviations from designed shape can be measured with ad hoc system to qualify surface profiles for free-form optics.

The output of the surface characterization is a map showing the difference between the desired profile and the real one. Typical values representing the data-set are the "Peak to Valley" (P-V), defined as the maximum difference measured on the overall surface, and *rms* defined as root mean square of the values in the map.

In *Figure 69* the output of qualification for a panel produced for MAGIC telescope and the mould used to produce it is reported.

[19] www.optimaxsi.com

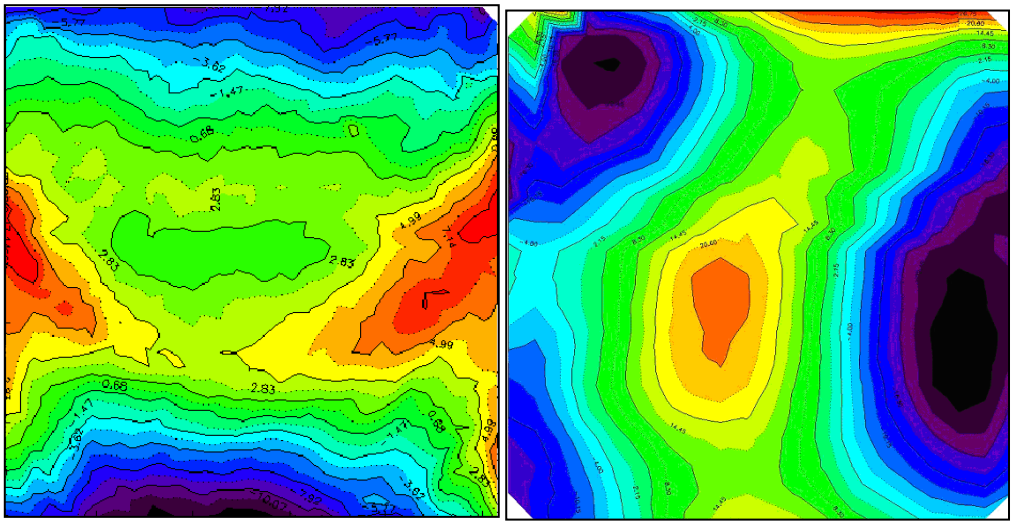

Figure 69: 3-D Metrology of a MAGIC mirror and its relative mould obtained by 3D touching probe method [Giro, 2011].

In particular, Phase Measuring Deflectometry (PMD) and touching probe are the elected methods to scan areas of the order of the Cherenkov panels. These methods will be described in details in the section III.4.

3.2 Surface Properties

The quality of an optical surface describes its cosmetic appearance and involves the evaluation of imperfections such as in scratches, digs (little pits), sleeks (tiny scratches), bubbles, edge chips, and coating blemishes. Surface quality describes the level of imperfections that can be visually noted on the surface of an optical component. In most cases, these surface defects are purely cosmetic and do not significantly affect system performance, though, they can cause a loss in system throughput and an increase in scattered light. The major concern instead is that they may constitute weak points where structural cracks (e.g. from an edge chip) or coating degradation (e.g. from a coating defect) may start and develop compromising the whole panel. Surface properties concern both over layers and substrates devoted to optimize the optical performance and to protect the glass mirror.

3.2.1 ROUGHNESS

As reported above, surface roughness is a shape error on a microscopic, sub-aperture, high spatial frequency level. Surface roughness influences optical performance, by influencing the amount of wide-angle scatter and reducing image contrast [Bennett, 1993]. Roughness strictly depends on the technological process of mirror production.
If the diamond milling technique is used, the resulting roughness of the surface is below about 10 nm rms. In *Figure 70* one can see a typical surface profile analysed with a commercial tester. From the same picture one can also see one step of the milling machine that can follow the desired profile until the level of the micron [Bastieri et al., 2007].

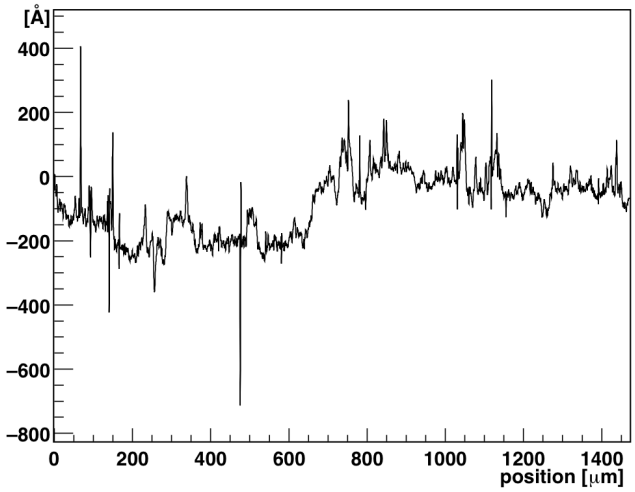

Figure 70: Roughness diagram of a sample taken from a MAGIC mirror after milling and coating. The profile [Å] is plotted against the position [μm][Credits: D. Bastieri et al., 2007].

If the cold-shaping technique is used, typical roughness is about 3 nm. In this case the master mould used to shape the mirrors has to be worked with the same optical precision needed for the mirrors, because every defect on its surface in principle is reproduced on the glass [Pareschi et al., 2008]. Indeed, there are some evidences that for very high spatial frequencies mould defects are not replicated. On the contrary, the presence of dust on the mould could represent a critical point in errors replication on local region of the mirror. An example of the consequences of a dusty environment is reported in the Figure 91 of the chapter IV.

3.2.2 COATING CHARACTERIZATION

Due to intimate connection between coating technology and local reflectivity, we already treated this topic it in a previous section (II.2.3) although it is actually a surface property.

Coating is a thick film, usually applied after the polymerization of the glue in order to make the glass surface reflective and resistant to environmental conditions. The processes of aluminization and deposition of protective quartz layer via physical vapour are performed under high vacuum environment (about 10–6 mbar) in a dedicated chamber [Canestrari, 2009]. Cleanness of the glass is important to have a good adhesion of the coating on the surface [Giro, 2011].

It is possible to perform several mechanical and environmental tests on small mirror samples to determine the robustness of the coating. The most important ones are: coating adhesion, abrasion tests, sand blasting, temperature and humidity cycling, bird faeces, salt fog.

The *coating adhesion test* is performed to prove the perfect adhesion of the coating to the substrates where it is applied in various points and around the edges of mirrors. Coating adhesion consists in applying a clear sticky tape with an adhesion power of 16 N per 25 mm to the coated surface of the samples and ripping off it at a rate of < 1 s per 25 mm (so-called "snap test"). The tape and mirror are inspected for coating loss. Coating adhesion tests can be performed also after weathering and salt-fog tests on representative samples. The test is passed if samples do not show indication of detachment of the coating.

Different *abrasion tests* can be performed on sample mirror. A known force is applied on the coated surface by using a standard abrasive tool (i.e. cheesecloth or an eraser). The surface is inspected after the test to evaluate the damage of the coating.

Figure 71: Coating samples after a severe abrasion test. Upper: Al + SiO_2. Middle: Al + SiO_2 + HfO_2 + SiO_2. Lower: dielectric coating [Förster, 2013].

In the *sand blasting test* silicon carbide of a known minimum grain size is forced onto the surface of the sample via a pressurized airflow at an angle of 45° to the sample. The resulting abrasion ellipse is measured. Usually this is a relative test, and simply grades coatings according to their robustness. There is not an absolute pass/fail.

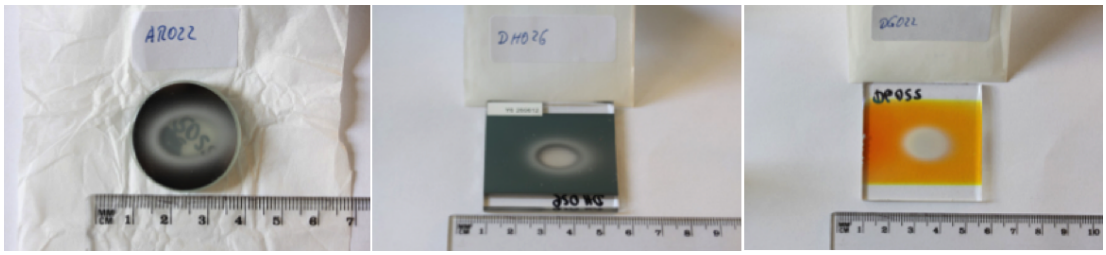

Figure 72: Coating samples after the sand-blasting test. Upper: Al + SiO_2. Middle: Al + SiO_2 + HfO_2 + SiO_2. Lower: dielectric coating [Förster, 2013].

It is possible to simulate the effects of bird feaces by treating the samples with pancreatin. The coated surfaces are then "baked" for 4 weeks at 40° C in a climate chamber. In this way the effects are similar to exposition of the mirror surface for some time in a hot and dry environment, as is typical for locations of Cherenkov telescopes.

Salt-fog test is performed by exposing the sample mirror for 72 hours to a salt-fog atmosphere at a temperature of about 20° C with a salt concentration of 5%. After testing, samples are washed with distilled water and inspected for corrosion and changes in reflectance. This is a standard test for paint coatings in automotive industry [COM-TDR, 2015[20]].

3.3 Mechanical Properties

As described above, performances of the mirrors are strictly related to shape, surface and stability on time scale of the lifetime of the panels. In particular, surface properties are influenced by coating interactions with panel substrate, while shape properties are

[20] Common Technology Evaluation, Testing and Calibration Technical Design Report, COM-TDR/140721 | v.5.1 | CTA Consortium, May 2015

affected by the stability of the substrate itself. The following properties have to be taken into account in developing technology for mass production of mirrors for CTA:

- Weight < 20 kg/m^2 is desirable;
- Mirror deformation under gravity must be small enough to maintain the specifications for the PSF and the alignment;
- Mirrors should not suffer mechanical deformation during their expected lifetime;
- No damage in temperature range between extreme temperature values (i.e. from -15 ° C to 60 ° C);
- No significative elastic change in shape in the operational temperature range (i.e. between -10° C to 30° C).

Cherenkov mirrors need to survive to particular aggressive weather conditions and so it is necessary to test them for mechanical performances in robustness and stability. Long-term effects caused by stress relief in the glass could in principle lead to figure changes, such as additional stresses due to environmental conditions (i.e. strong winds, large temperature shifts) as well as elastic deformations due to operative conditions (i.e. axial gravity, moderate wind and temperature gradients across panel thickness).

The choice of commercial glass material for the sandwich faceplates is favourable in terms of cost, but it requires a careful evaluation in terms of mechanical strength. Major worries are associated with possible insufficient stability to impacts and water ingress. The last inconvenience may have severe consequences on panels, as in the rigid mountain climate water may freeze within the structure permanently deforming it.

For this reason the weight of the mirrors before and after the test has to be checked: penetration of water inside the sandwich structure shall not occur [Giro, 2013].

As a matter of fact, the strength of glass is not an intrinsic property of the material, but on the contrary, it strongly depends on the whole processing method. In fact, strength depends on several parameters such as: distribution of cracks (or surface flaws), entity of stressed surface area (or volume), stress distribution, residual internal stresses from manufacturing process, nature of the loads (static or cyclic), fracture toughness, humidity, temperature. Furthermore, glass materials are susceptible to sub-critical crack growth in monotonic tension due to the influence of moisture. Handling, glass cutting and edge finishing can also affect the surface defects and so the strength. Finally, further strength degradation can occur due to the exposition to the environment.

Figure 73: The MAGIC II telescope during a strong winter season.

The facets must be rigid enough to contrast gravity deformations without changing their optical characteristics, considering the wide range of elevation that the telescopes span during operation.

Optical testing should be repeated to check for changes in PSF or reflectance, if the mirrors are not irreparably damaged by mechanical tests.

It is possible to perform several mechanical and environmental tests: water tightness testing/rain simulations, impact testing, temperature and humidity cycling, solar radiation testing (UV-A irradiation).

Temperature and humidity cycling is one of the test performed to investigate to what extent the performances of the mirror are affected by climatic stress. This may result in both reversible elastic deformation changing the PSF and irreversible plastic deformations. Typical thermal cycles are performed in the extreme range from -15° C up to +60° C. Degradation of the order of the 3% on the focal spot dimension could be acceptable.

The mirrors may occasionally be subject to mechanical impact, such as birds flying or picking on the mirrors, or possibly hail fall. The mirrors have to show resistance to stress from mechanical impact. A typical test is performed dropping a steel ball over the optical surface of the mirror with different degrees of severity meaning both different weights

and different starting heights. No cracks, bumps or defects on the optical surface shall not found in a visual inspection performed after the impact [Canestrari et al., 2013].

Figure 74: Impact test on a MAGIC mirror. Courtesy of M. Mariotti.

To measure the hardness of small volumes of materials (glass, coating), nanoindentation could be applied to samples under test. During an indentation test, for example a diamond tip of known geometry is pressed into the sample surface, while the indentation load and depth are recorded. The evaluation of hardness and elastic modulus is based on the analyses of the load-displacement curves. Also the scratch and the wear tests represent a method for testing mechanical resistance of thin films and coatings. The generated stress-fields under the indenter result in different failures including coating detachment, through-thickness cracking, plastic deformation or cracking in the coating and/or substrate. Visual analyses of the effects suffered by the tested samples are generally used for evaluation [COM-TDR, 2015].

3.4 Mirror Test Facilities

A Mirror Test Facility (MTF) is devoted to characterize mirrors and test equipment, and to evaluate mirror technologies. The tests performed should be, as far as possible, independently by mirror manufacturers and developers. The optical quality as well as the mechanical stability and the long-term durability of the different mirror technologies need to be evaluated in a consistent and systematic way.

In the framework of the CTA Project other tasks of the MTFs are:

- design and operate test procedures for the performance, stability and durability of the mirrors;

- conduct comparable tests of all mirror and coating technologies considered for use within CTA;

- provide documentation of the test results including an evaluation of whether the mirror/coating technology tested that fulfils the needs of CTA.

The mirrors of a Cherenkov telescope have less demanding imaging properties than mirrors for optical astronomical telescopes. The Cherenkov mirrors are permanently exposed to the environment but need to maintain a good performance over many years of lifetime. Underperformance or rapid degradation of mirrors, which are usually custom-designed but industrially manufactured products, directly decrease the performance of a Cherenkov telescope, and in consequence reduces the sensitivity of the array.

The most relevant parameters to be measured are PSF of the single panel, usually expressed in terms of R80 and the absolute reflectance on the focal plane [COM-TDR, 2015].

A common approach to measure these quantities for spherical mirrors is the *2f method* as illustrates in Figure 75. A point-like light source is placed at twice the focal length of the mirror, together with a detector (photodiodes or a CCD) recording the returned light. The PSF and the absolute reflectance into the focal spot can be determined easily in such a setup.

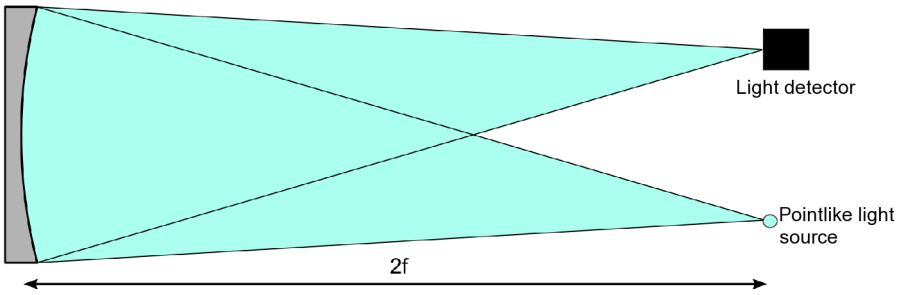

Figure 75: 2f test set-up.

This test setup is rather simple to implement, but has several disadvantages: the need of a sufficiently large room (R ≈ 34 m in the MAGIC case), as well as the rather difficult alignment of the mirror. Another disadvantage of the 2f method is that the testing conditions differ from the operation conditions on a telescope: the testing is done with an on-axis point source at ~ 30 m while the mirrors on the telescope are mainly operated off-axis and the light source, in this case the air-shower, is at a height of about 10 km [Schulz, 2011].

The 2f test does not easily work for aspherical mirrors designed for the Schwarzschild-Couder type telescopes (i.e. ASTRI telescope, CTA SST-2M).

Furthermore 2f method does not provide any information about surface of the mirrors. On the other hand, Phase Measuring Deflectometry method (PMD) can give a detailed map of the mirror shape down to micrometer level and of its curvature [Knauer et al., 2004]. The deflectometry test is a modification of the classical Ronchi test [Ronchi, 1927] based on local slopes measurement and performed by illuminating a mirror with a known light pattern and acquiring pictures of the reflecting surface. It consists in observing the distortions of the defined pattern after the reflection by the examined surface and from them eventually reconstructing the surface shape [Sironi et al., 2014].

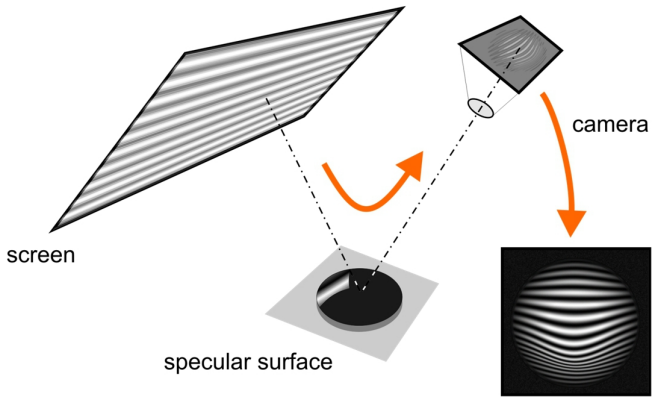

Figure 76: Typical PMD test system. The camera takes pictures of the distortions of the pattern after the reflection on the mirror [COM-TDR CTA Consortium 2015].

The accuracy of this method can reach about 1 μm. The resulting distortions are recorded by CCD cameras and can be used to calculate the exact slope on each point on the mirror surface and, by numerical differentiation and integration, the curvature and shape of the surface. Raytracing is then employed to calculate the PSF. It is worth noticing that PMD method can only determine the PSF, not the reflectance of the mirror.

The touching probe system is an alternative method to evaluate shape errors. It retrieves a 3D map of a sample by using a scanning head that measures the distance between the surface under testing and a reference plane (usually built in granite). In this case the accuracy reached is about 10 μm.

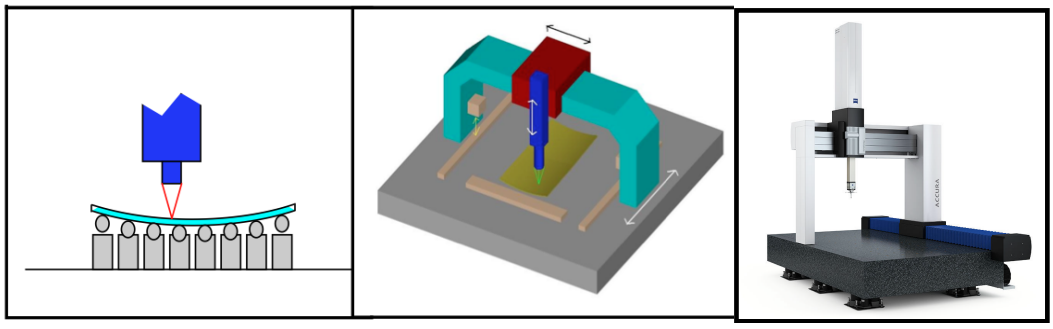

Figure 77: Left: Profilometry on astatic support [Ghigo et al., 2008]. Right: 3D touching machine (ZEISS ACCURA Series).

3.4.1 Overview of CTA Facilities

All the institutes involved in CTA mirror development usually have a setup to measure optical and mechanical/environmental performances. The optical quality as well as the mechanical stability and the long-term durability of the different mirror technologies need to be evaluated in a consistent and systematic way.

Test Facilities perform independent testing and participate in cross-calibration operations, to ensure that the main requirements are met. Two classes of facilities can be distinguished. Optical facilities are designed to implement 2f and PMD methods, while and the other ones are devoted to mechanical/environmental tests on samples.

There are two prototype PMD stations: one in Zeuthen and one in Erlangen. The Erlangen-Zeuthen test facility uses Phase Measuring Deflectometry (the basic principle is shown in Figure 76) to inspect large-sized spherical mirrors using a compact setup. The equipment in Zeuthen is set up within a climate chamber to allow the changes in optical characteristics due to temperature oscillation to be measured. An additional measurement of the local reflectivity with an optical spectrometer is possible. In Figure 78 the compact setup of PMD called SWD-PMD ("short working distance") occupies a space of about 6m x 3m x 3m.

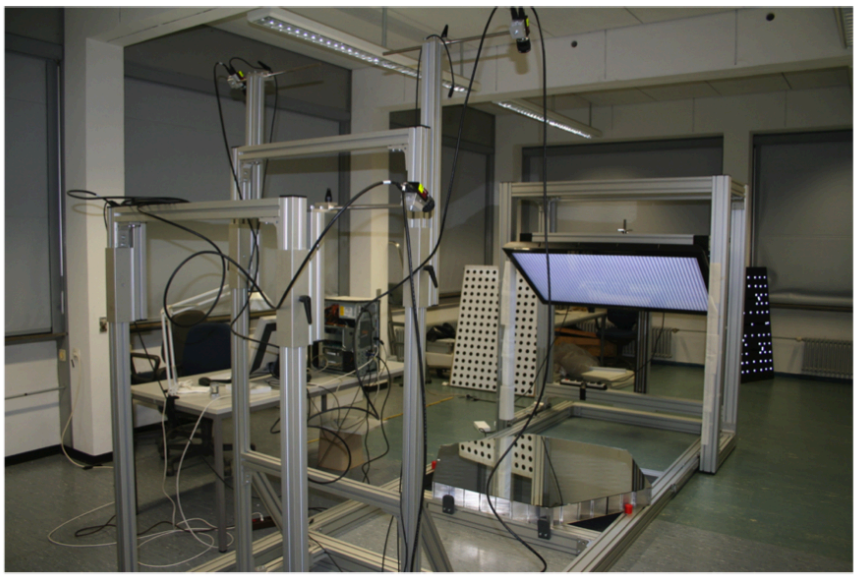

Figure 78: Picture of the short working distance PMD set-up.

The “Institut für Astronomie und Astrophysik Tübingen” (IAAT) operates a Cherenkov mirror test facility using the 2f method in the basement of the Sand campus building.

Figure 79: Tübingen Optical Test Facility [Schultz, 2012].

The equipment was developed by Max Planck Institute for Nuclear Physics (MPIK, Max-Planck-Institut für Kernphysik, Heidelberg, Germany) and was relocated to Tubingen where all 900 facets of the HESS II telescope were measured before shipment to Namibia. In addition, a newly adapted and improved setup has been developed by IAAT and is currently being tested and finalized. It has already been used to measure CTA mirror prototypes.

The test bench hosts a halogen lamp with an aperture close to point-like light source, and a scanning table carrying a photodiode which points towards the mirror. The setup is used to scan the light spot in a grid. Measurements can be performed at several wavelengths (from 310 to 600 nm) by using a dedicated filter wheel. The absolute reflectance measurement of the mirror under test is possible with an ad-hoc calibration of the photodiode. In the same set-up is possible to mount a CCD camera instead of photodiode, in order to perform direct imaging of the PSF.

In this framework INAF proposed Merate as optical test facility. In the chapter IV of this work this topic will be discussed in details.

Mechanical/environmental characterization requires different set-ups and approaches. For this reason specialized laboratories have been optimized to perform simple tests based on standard specifications that simulate as closely as possible the environmental conditions of CTA sites. Many of the tests are also designed to create some accelerated aging in the samples.

Mechanical/environmental CTA facilities are listed with their relative activities:

- Durham University (UK) for coating adhesion, water tightness test, impact test, temperature cycling, solar radiation testing, abrasion (mild and severe), sand blasting, and salt fog;

- Olomouc (Czech Republic) for scattering, reflectance and nanoindentation tests;

- MPIK (Heidelberg, Germany) for coating adhesion, abrasion (mild and severe), sand blasting, nanoindentation, temperature and humidity cycling, bird faeces and salt fog.

3.4.2 FACILITIES CROSS-CALIBRATION

Cross-calibration of the facilities proposed for CTA Project has been scheduled in 2015.
The aim of cross-checking is to assure that the measurements performed by different facilities are coherent, in order to confirm the robustness of the results obtained and the accuracy of the measurement performance. This ensures that the facilities are well designed and procedures are not flawed.
Furthermore, in order to exclude possible discrepancies among the measurement results due to different analysis software, a cross-analysis can be performed on the individual data sets obtained from the facilities when possible. For this purpose, both individual analysis routines and standard astronomical analysis software can be used.

Chapter IV

CALIBRATION IN MERATE FACILITY

In this chapter we are going to describe in detail the Test Facility in Merate (Brera Astronomical Observatory, INAF OAB) and discuss its measuring capabilities. The facility is part of the CTA network to test and characterize the mirrors to be mounted on the telescopes of the array. Due to its features, this test facility is devoted to the Medium Size Telescopes (MST) panels. The Merate Test Facility has been put in operation in 2015 after a cross-calibration with the other facilities [Canestrari et al., 2015].

4.1 Detailed description of the facility

4.1.1 SPECIFICATIONS

The facility in Merate has been built to test spherical mirrors with curvature radii in the range 30 – 36 meters. The facility is designed to qualify the following properties:

- focal length;
- R80;
- astigmatism
- scattering light.

For these measurements the set-up is named *2f,* as shown in the scheme below.

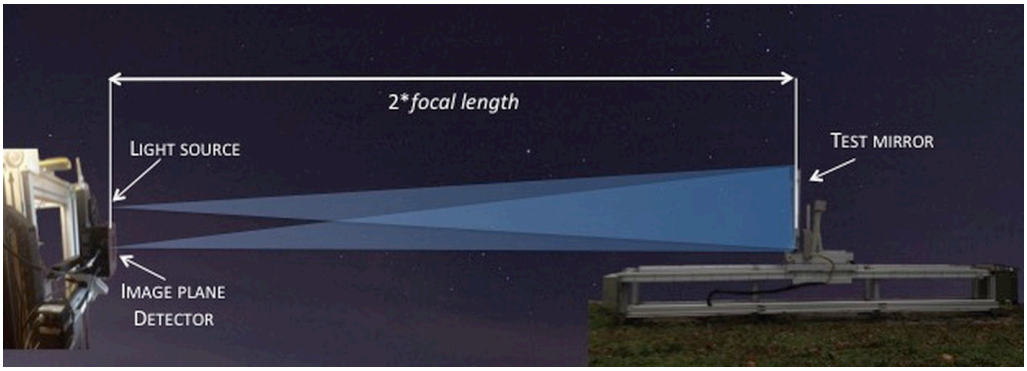

Figure 80: Optical set-up for the 2f configuration.

Four main elements compose the assembly:

- the point-like source devoted to the illumination of the mirror;
- the mirror holder;
- the detection unit, composed by a CCD camera and its filter wheel;
- a laser meter.

The facility is located in open air, and the ancient dome of the meridian circle houses the detection unit and the control room. The CCD detector sees through a small window the optical bench supporting the mirror.

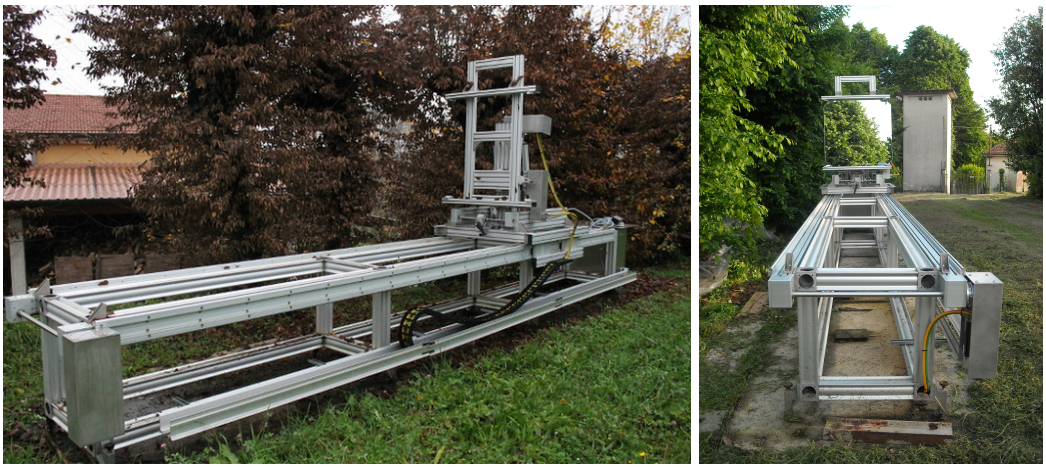

Figure 81: The facility in plein-air: the optical bench.

In the next section we will describe the main components of the system and their functions.

4.1.2 SERVO-MECHANISMS

The mirror holder (outside) and the detection unit (inside) are mounted on two stages servo-controlled stages. In this way both focus tuning and focal-plane scanning can been automated to permit a remote control thus allowing swift, quick, reliable, safe and manpower-saving operation.

The outdoor stage has been conceived and designed at the INAF-OAB. The engineering, realization and installation activities were performed by the Officina Opto-Meccanica Insubrica and Automation One companies[21].

The rail subsystem is composed of a couple of 6 m long stainless steel linear guides. This technical solution, although economic, ensures a positioning of the carriage well below 1 mm on the full travel range of the rail. The actual distance of the carriage from the indoor stage of the facility is measured by an external laser distance meter, suitable for outdoor measurements over large distances. This guarantees measurement accuracy of the optical path within a few mm over more than 30 m.

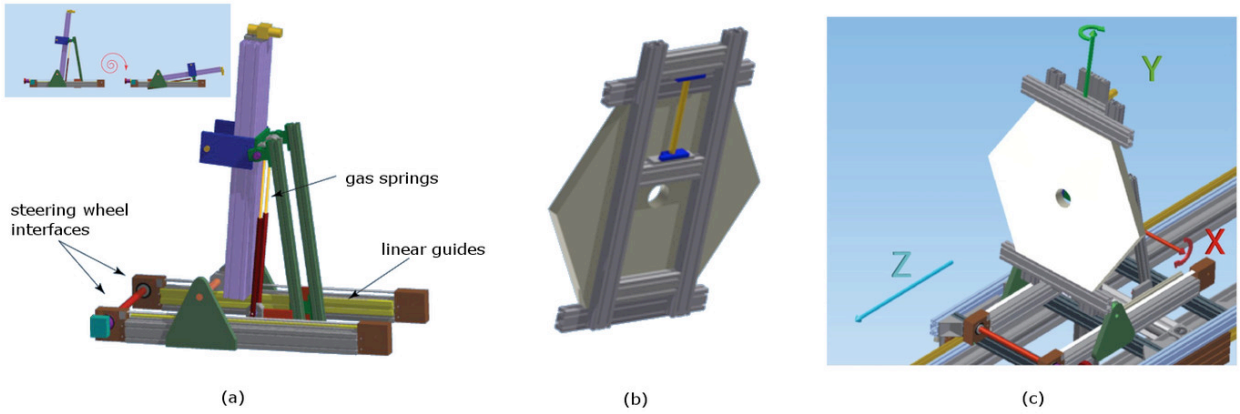

Figure 82: Detailed view of the mirror support subsystem. Panel (a) shows the support itself, the box in mounting/dismounting configuration; panel (b) shows the holder with a mirror template; panel (c) shows the reference axes for the three motorized motions of the outdoor stage of the facility.

The mirror support, shown in Figure 82, is installed over the carriage and is designed to ease the mounting and dismounting operation of the mirror under test as well as to facilitate the alignment of the mirror itself over the optical baseline of the entire facility. It

[21] http://www.automationone.it

can be divided into two subsystems: the mechanical jig and the motorized holder. The jig can be horizontally reclined to execute the loading and unloading of the mirror. This movement is performed manually by means of a small steering wheel and it is supported by gas springs. The holder of the mirror is obtained by means of an adjustable system of aluminium beam profiles and soft clamps. This holding system can be moved in such a way the mirror tilts with respect to two axes.

The drive system for tilts adopts the same solution of the rails. Again, this solution has been adopted since it represents a good trade-off between cost and performance. It guarantees a wide angular range for alignment purposes of 5 *deg* along the X-axis and 10 *deg* along Y, with a resolution better than 12 *arcsec*. This resolution corresponds to a translation of about 1.9 mm at the indoor position with the carriage at 33 m (half of the rails traveling length). The mirror support can be loaded with panels up to 45 kg having different tile shapes (e.g. squares, hexagons, rounds) up to 1.5 meters in diameter.

The indoor stage is based on a carriage with a two-axis system. The scanning plane is perpendicular to the optical axis of the facility. The two-axes X e Y permit an excursion with range of 30 cm and a resolution of 100 microns. In this way, a raster scan of 4x4 CCD images permits to cover a focalization area of 20x20 cm, fully sampling the outer wings of the mirror PSF. A control software is devoted to acquire the images in batch mode.

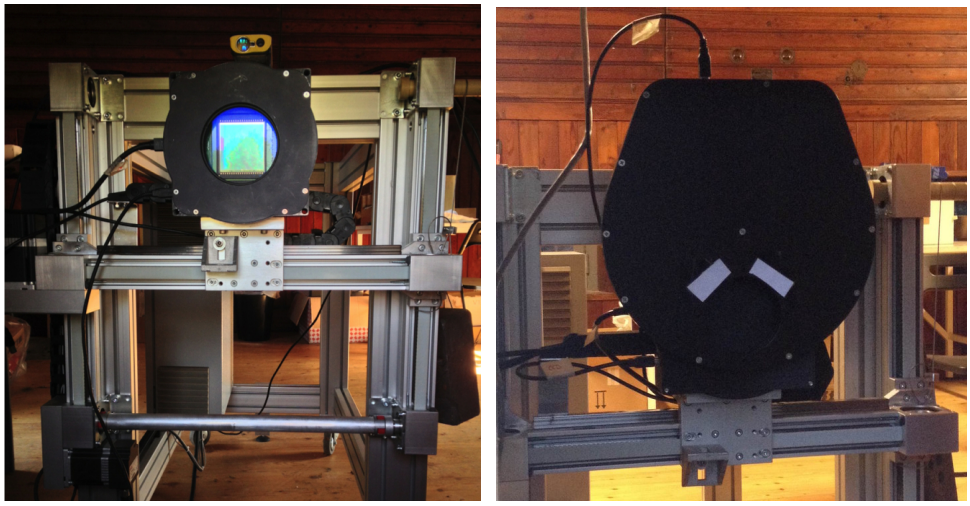

Figure 83: Left: the detection unit on the scanning carriages. Right: filter wheels and the illumination system.

The motion is controlled with 2 belt-teethed linear guides equipped with hybrid bipolar high torque stepper motors. The resulting resolution of the motion is 0.1 mm. The communication interface is through the CAN open protocol. The raster scan is a relevant tool in the scattering evaluation. In fact scattering effects typically arise because of surface irregularities. This induces angular deviations from the specular one generating broad diffused light component centred on the core of the PSF.

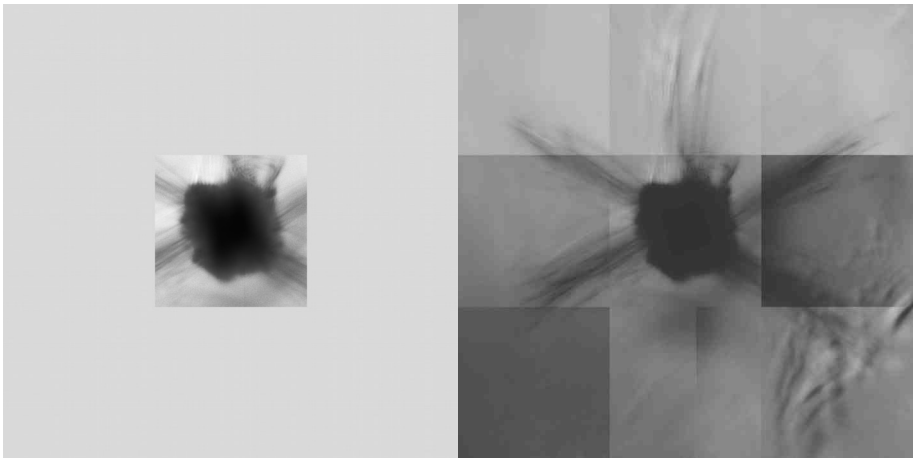

Figure 84: PSF acquired by a single frame of the CCD located at the center of the detector plane (left) and PSF raster scan on the detector plane 15x15 cm (3x3 frames). Six tails are quite evident correspond to the hexagonal shape of the mirror. Acquisition of the full mosaic allows proper evaluation of the background and of the shape and width of the PSF that would be underestimated if the outer images were neglected (right).

4.1.3 LIGHT SOURCE

The light source is a compact device designed to generate an appropriate wavefront in order to illuminate the mirror under test.

As show in Figure 85, a pattern of five ultra-bright LED covers the full range of optical spectrum:

- red: 626 nm;
- green: 525 nm;
- blue: 470 nm;
- white;
- RGB (composition of red/green/blue, mixed or single colour modalities).

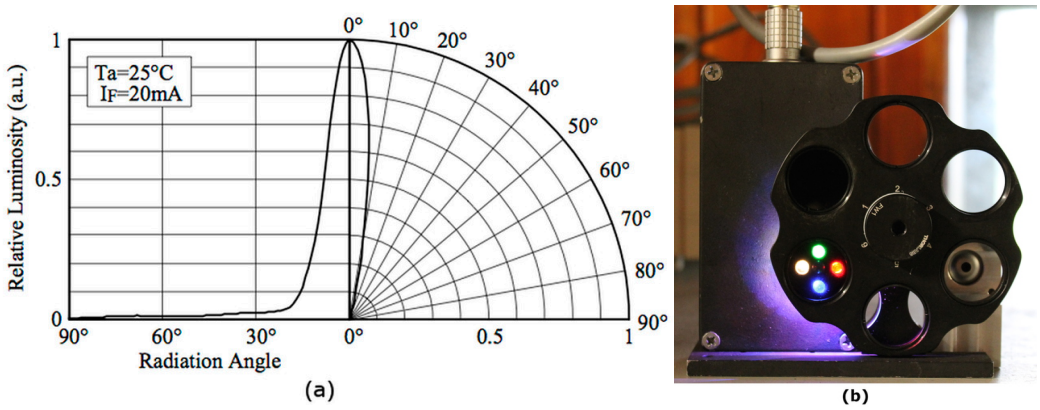

Figure 85: Pattern of five ultra-bright LED (right). Light emission diagram (left).

The light source is remotely controlled with a dedicated PC. In the light emission diagram, the cone angle is about 10 degrees with intensity of about 12000 mcd. In front of to the light source a filter wheel equipped with several logarithmic neutral filter takes place and permits to illuminate the mirror with a suitable light flux. A semi-conductor laser is mounted on the other side with respect to the LEDs for alignment operations.

4.1.4. DETECTION UNIT AND ITS CHARACTERIZATION

The optical configuration of the facility is designed to detect directly the mirror PSF into its focal plane by means of a large size CCD camera. Usually, the PSF is re-imaged by using a translucent screen and a devoted optics in front of CCD camera[22]. This configuration has the clear advantage to allow using of small size CCDs, with the downside of an inaccurate photometry that is avoided in our configuration.

The camera is commercially available for astronomical applications from the Finger Lakes Instrumentation producer. The model is PL4301E from the Pro Line serie characterized by low noise, high sensitivity and resolution and deep cooling. The sensor is a KAF-4301 from Kodak now commercialized by Semiconductor Inc. producer[23,24]. It is a large format CCD with 2048 × 2048 pixels 24 μm side for a total diagonal of 70.7 mm. It is equipped with a 90 mm shutter to avoid any vignetting of the detector. A filter wheel (Figure 83) can be mounted on top either to dim the incoming light or to select a particular wavelength, if needed. The PL4301E has a thermoelectric cooling system capable to cool down the detector temperature to about 50° C below the ambient one in about fifteen minutes (Figure 86).

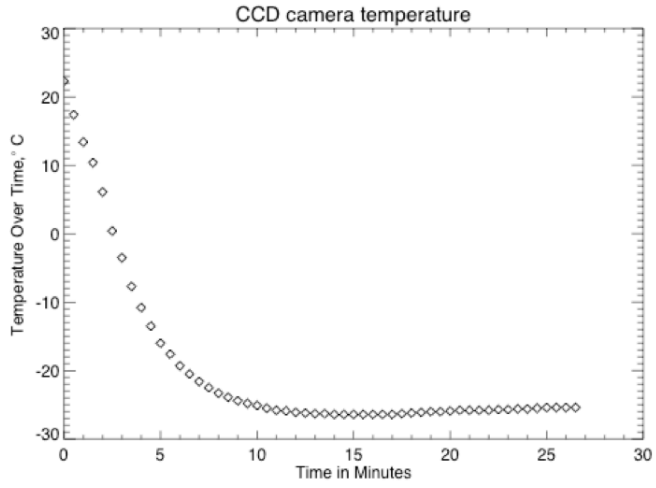

Figure 86: Cooling down of the CCD detector used in the facility

[22] www.flicamera.com
[23] www.ccd.com/pdf/ccd_43.pdf
[24] www.onsemi.com/PowerSolutions/

The CCD camera has undergone a careful characterization in terms of gain and read-out noise (RON), linearity, dark current and Charge Transfer Efficiency (CTE). The gain has been evaluated acquiring a series of images with increasing exposure times followed by a series with decreasing ones. For each image the variance is computed and plotted against the median counts of the image itself. The gain is hence the angular coefficient of the best-fit line, while the RON is obtained by multiplying the gain and the mean value of the bias frame (shot noise curve).

Each image used is the mean of two subsequent acquisitions A and B, both corrected by dark and bias signals. This procedure guarantees to check both shot- and long-term variations of the camera. Linearity and dark current are evaluated by varying respectively the exposure time for a number of bright and dark acquisitions, and then taking the median value. All these parameters depend from the read-out speed. We report in Table 2 the results for the 1 MHz high gain setup, typically used, that shows the full set of calibration results.

Download speed	**Gain** [e^- /counts]	**RON** [e^-]	**Dark currents** [e^- /pixel/s]	**CTE** [%]
1 MHz high gain	1.95699	10.8632	< 0.03	99.999878
1 MHz high range	12.6399	37.4377	< 0.2	99.99973 1
1.7 MHz high gain	1.73786	13.0477	< 0.3	99.99976 9

Table 2: Analytical results of the CCD calibration for different read-out speeds [Canestrari et al., 2015].

CTE has been derived by the cosmic rays impacts detected on a long dark exposure. Cosmic rays impact the detector like stochastic events with casual angles and energy but they can be used to diagnose the CTE of the detector [Riess et al., 1999].

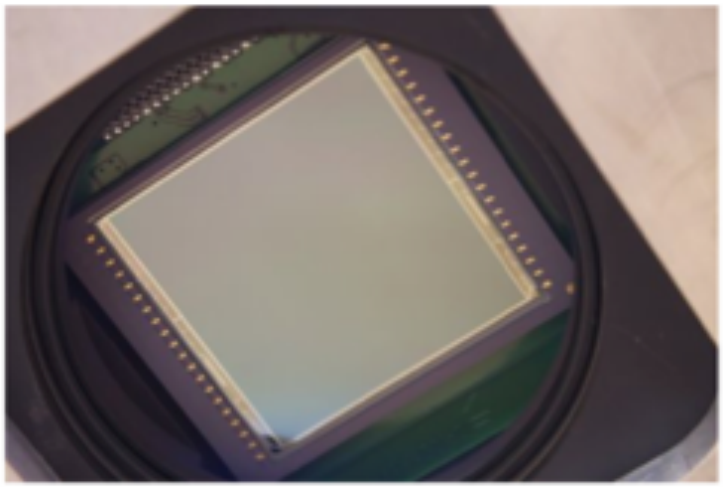

Figure 87: CCD camera inside its housing.

4.2 A case study: The mirror replacement of MAGIC I and II

During the period January 2014-June 2015 Media Lario Technologies Company built on behalf of INAF 72 mirrors for replacing the deteriorated ones in MAGIC I and II telescope in La Palma (Canary Islands, Spain). This brought the possibility to cross calibrate the new facility with measurements obtained during the production pipeline. In the next sections we will describe the dish surface of the two MAGIC telescopes and which mirrors had to be replaced, the production pipeline of the new mirrors, the cross calibration of the facilities using a small sample of the production and how the installation distribution has been decided and proposed.

4.2.1 THE REFLECTING SURFACE OF MAGIC

As reported in the section II.1.2 the two MAGIC Telescopes have a parabolic optical configuration (f/1). Each dish is composed by 248 panels mounted on three supports, two actuators and one fixed point. Due to the parabolic shape, the position on the dish of the single panel defines the required focal length of the spherical mirrors. There are differences between the two telescopes:

- In the case of MAGIC II the mirrors are mounted directly on supports, and have a square shape with a one-meter size. In the inner part of the dish are mounted 140 diamond-milled aluminium mirrors, while in the outer corona 108 mirrors have been produced with the cold-shaping technique (section II.2.3).

- The panels on the MAGIC I reflector are mounted in a chessboard assembly. The two layers of panels are separated in height (60 mm) in order to avoid collisions between neighboring panels during operation. This feature has to be taken into account if glass mirrors (designed for MAGIC II) have to be mounted on MAGIC I instead of Aluminum mirrors. A specific adapter is designed for each telescope assembly.

- The optical surface of MAGIC I has been completed at the telescope in 2004, while for MAGIC II case the installation occurred in 2007-2008. In 2014, after a period of 10 years, a refurbishment of the reflecting surface has been considered necessary to have the original performances.

As discussed by Garczarczyk [2014], a criterion of quality degradation has been introduced to select the mirror to be replaced. This criterion takes into account the deformation of the mirror surface and the local reflectivity with the former representing the most crucial source of degradation. A list has been produced with the position of the mirror to be replaced.

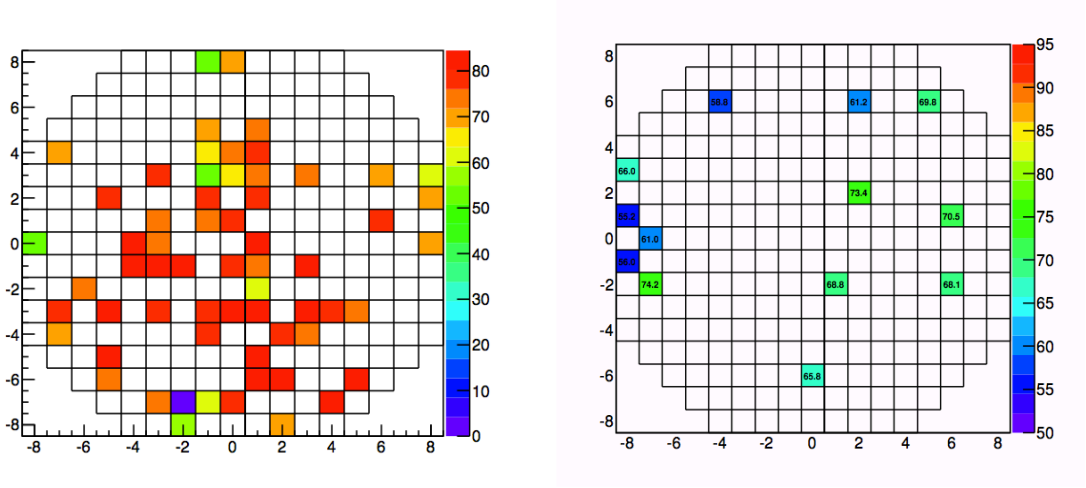

Figure 88: Mirror panels to be substituted by new m^2 mirrors. Left: selection for MAGIC I, Right: selection for MAGIC II. The color code represents the mirror quality (reflectivity folded with the surface deformations) [Garczarczyk, 2014].

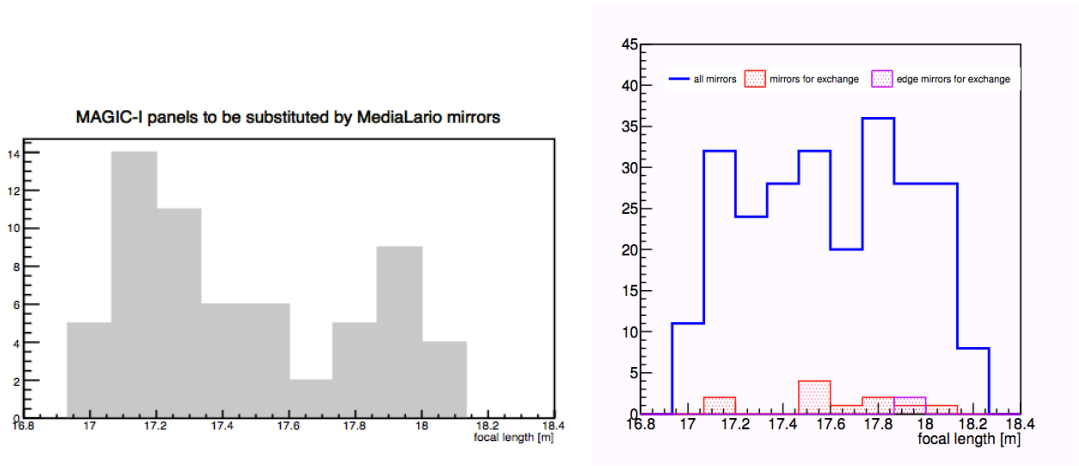

Figure 89: Focal length distribution of the selected mirrors. Right: for MAGIC I. Left: for MAGIC II [Garczarczyk, 2014].

Looking at Figure 88 and Figure 89 we can observe the spatial distribution of the damaged mirrors. While in MAGIC I case the deterioration of the mirrors is due to aging factors (the central portion of the dish seems more degraded), in MAGIC II the selection of the mirrors seems to be driven by production failures.

In fact, the damaged aluminium mirrors show shape deformation, while the glass ones show coating detaching. These latter cases can be adducted to "infant mortality" of the bathtub curve of the pipeline production process.

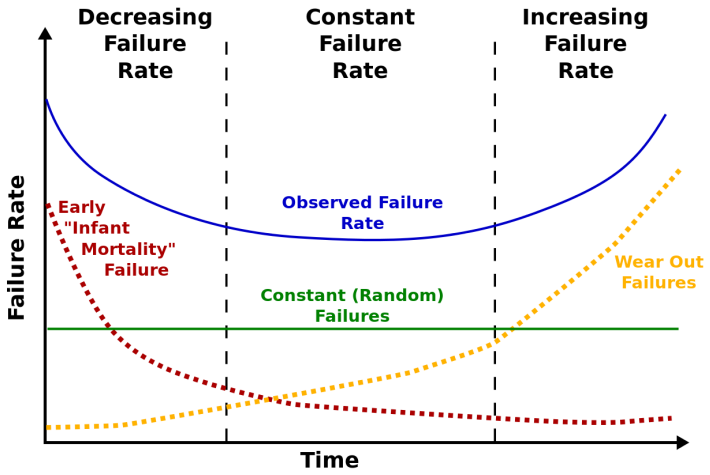

Figure 90: "Bathtub curve" for the failure rate as a function of time.[25]

[25] www.chemicalprocessing.com

4.2.2 MEDIA LARIO PRODUCTION

Considered the specifications requested by MAGIC collaboration [Garczarczyk, 2014] INAF signed a contract with Media Lario[26] for the production of the replacements of 72 mirrors at the end of 2013.

These are the milestones of the contract:

- Delivery of Radius of Curvature (RoC) table;
- Manufacturing of the moulds;
- Manufacturing of the pads;
- Production pipeline;
- Coating pipeline;
- Tests and mirror identity card delivery;
- Packaging and shipping.

A specific RoC table gives constrains on the set of moulds to be used for the production. A compromise is needed in order to minimize the production cost and optimize the distribution of the RoC produced by different moulds. In fact using the spring back effect is possible to use the same mould for different radii of curvature. In this production case two moulds have been used with RoC of 36.3 m and 35.0 m. The first one was used the 2008 production and is a diamond turning mould. The second one has been manufactured for this production, and is not diamond-lapped. For this reason its shape is affected by higher roughness and circular patterns. In both cases the moulds are inside specifications, but the circular patterns can be seen observing the replicated mirrors from their pupil plane of the replicated mirrors (Figure 91).

[26] www.media-lario.com

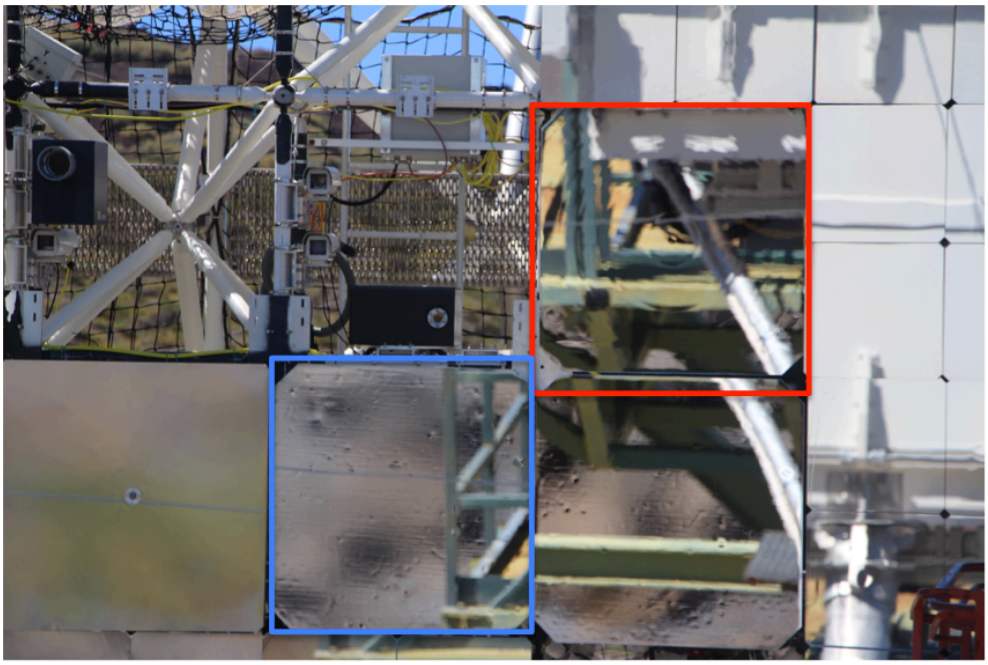

Figure 91: Circular patterns due to ripples present in the mould (in red). Bubbles due to dust particles present in the mould during the assembling phase (in blue).

A related activity is the manufacturing of pads and adapters, which has to be designed for the two mechanical arrangements of the telescopes.

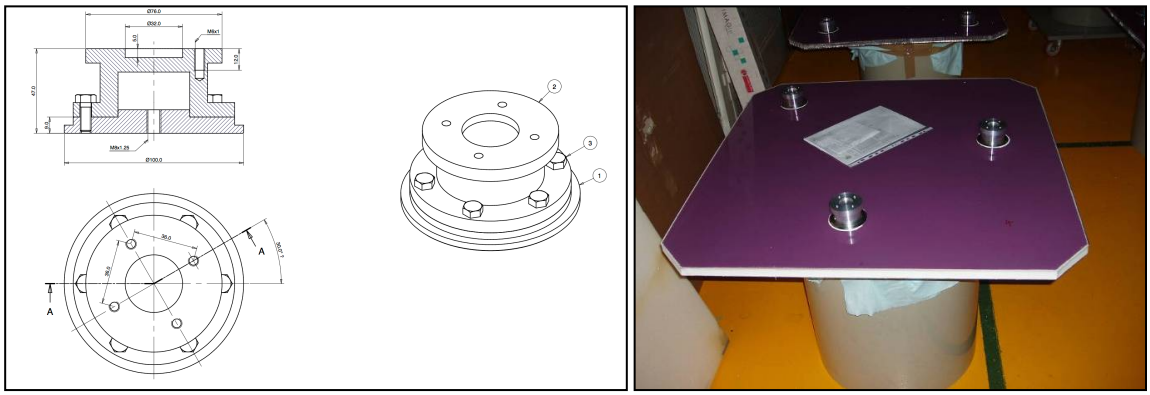

Figure 92: Left: mechanical drawing of a generic pad and its adapter. Right: pads and adapter on the panel.

The thermal expansion coefficient of the glass (CTE) leads to some constraints for the material and the glue chosen for pads and adapters. While pads are built in stainless steel and glued directly on the glass by a structural silicone (Dow Corning 7091), for a mass budget reason the elected material for adapters is aluminium.

The coating of the mirror (Al + 100 nm SiO_2) has been performed by *ZAOT* Company[27], with the same coating chamber used for the first MAGIC II production in 2008.

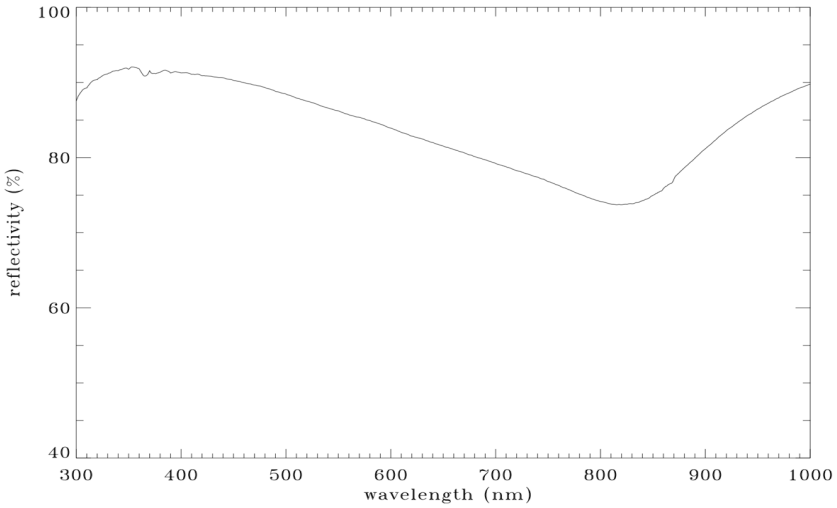

Figure 93: Plot of the reflectivity of MAGIC coating (Al+SiO_2).

For each mirror several tests are reported in an identity card used also for quality assurance purpose. This important topic will be addressed in the next section.

4.2.3 TEST, CHARACTERIZATION AND IDENTITY CARD OF THE MIRRORS

An important requirement for Cherenkov mirror production is long-term stability of the mirror performance figures. This goal can be approached applying quality assurance rules and procedures. In this context an identity card for each mirror shall describe tests and procedures applied during its production. Figure 94 shows a typical identity card delivered by Media Lario for each panel, shows a typical identity card delivered by Media Lario for each panel, while Table 3 summarizes the qualification and tests at which each panel is subjected.

[27] www.zaot.com

Parameter	**Criterion**
Visual inspection	Completeness, Integrity, Cosmetics OK (no stains, no scratches wider than 2 mm, summed length of all scratches & digs < 30 cm)
Panel reflectivity	Reflectivity > 80% from 300 to 600 nm
Coating Resistance	Tape lift off test ISO9211-4 (cond. 2 / sev. 2) successful
Panel mass	Less than 18 Kg
Spot size	Measured @ 80% Encircled Energy @ nominal focal length of 34500 mm < 1,5 mrad Target < 1 mrad

Table 3: Qualifications and tests performed on panels and satisfaction criteria.

Media Lario Technologies	**MAGIC** Glass Panels **IDENTITY CARD**	**PANEL** 164
	Doc. N° **MG–RP–ML–056 Issue 1**	Pag. 1/1

CLIENTE/ Customer	CONTRATTO / Contract	FIRMA PA / PA Signature	DATA / Date
Fundacion G. Galilei INAF	INAF PO 661/2013 Dated 19/12/2013	V. Laureanti	2014-06-19

Panel Identification and Reference Documents			
Panel Configuration:	0304-0005 Rev.1 – Central panel	*Panel identification*	164
Data Base ID:	Magic_Panels Identity_Card_DB.xls		
RFDs:			
NCRs/RFWs:	/		

Summary of Inspections and Results

Inspection ***Parameter***	***Required***	***Achieved***	***P / F***	***Remarks***
Visual inspection	Completeness, Integrity, Cosmetics OK (no stains, no scratches wider than 2 mm, summed length of all scratches&digs < 30 cm)	H/W Complete No damage, cosmetics OK	**Passed**	See observation details below.
OBSERVATIONS	corners&edges OK in terms of mechanical and coating integrity. No digs. Whitish haloes due to coating process close to the lower left corner. Small scratch close to the upper right corner.			
Panel reflectivity	*reflectivity > 80%* *from 300 to 600 nm*	R_{470nm} = 91.03% (centre) R_{470nm} = 88.77% (edge) R_{530nm} = 85.28 % (centre) R_{530nm} = 82.55% (edge) R_{650nm} = 80.44%(centre) R_{650nm} = 79.87% (edge)	**Passed**	Reflectivity measured on the panel with the MLT IRIS 908RS scatterometer.
Coating Resistance	Tape lift off test ISO9211-4 (cond. 2 / sev. 2) successful	No removal of coating from the panel	**Passed**	
Panel mass	≤ 18 Kg	< 12.5 kg	**Passed**	
Spot size	Measured @ 80% Encircled Energy @ nominal focal length of 34500 mm < 1,5 mrad Target < 1 mrad	0.68 mrad	**Passed**	Optical bench

Figure 94: Identity card delivered by Media Lario Techn. for panel 164.

The parameters taken into account in the identity card are:

- Visual inspection: several standards discuss how to quantify the visual inspection.[28,29]

In the Cherenkov case a such detailed standard of specifications is not necessary. For this reason, cosmetics for visual inspection can be considered passed if the criterion indicated in Table 3 is fulfilled.

- Panel reflectivity: Due to the peculiar spectrum of the faint Cherenkov light, a very high reflectivity in the blue part of the spectrum (300 – 600 nm) is required. Local reflectivity tests are performed on the surfaces of each mirror. The threshold criterion of 80% in the considered band has been imposed.

- Coating Resistance: Ten-years lifetime of the coating could be guaranteed by Tape lift off test ISO9211-4. The purpose of this test is to evaluate to what extent the mechanical properties of optical coatings on components and substrates are affected when subjected to specific tensile or shear stress conditions at ambient atmospheric conditions. A standard adhesive tape (12 mm wide x 25 mm width, strength on steel of at least 9,8 N per 25 mm width) is used to peel-off the coating. The requested degree of severity for conditioning method 02 is 2 (≈ 1 s to remove 25 mm of tape). The examination of the specimen shall be performed as in ISO 10110-7. The coating shall not show any evidence of coating removal.

- Panel mass: The MAGIC requirement for the panel mass is 18 kg. This value is easily fulfilled by Media Lario mirrors (≈ 12 kg). Weight panel can increase if water leaks in the honeycomb. For this reason the mirror is designed to be watertight.

- Spot size: Due to importance of this property, the discussion is addressed to the next section.

---

[28] International Standard ISO 10110

[29] MIL-O-13830

4.2.4 THE CROSS CALIBRATION WITH MERATE FACILITY

The production qualifications have been performed in Media Lario labs. Similarly to the 2007 production a cross-calibration has been carried out, measuring again a sample of mirrors with the Merate facility. In the present production the new facility has been used to characterize PSF, radius of curvature (RoC) and astigmatism of 5 mirrors (namely number production 134-135-136-137-138). All data have been collected in April 2014. The data set with its analysis will be discussed in the next section.

Figure 95: Pipeline production of the mirrors in Media Lario labs.

4.2.4.a Data set and analysis

We used *2f* set-up moving the mirror carriage to scan in an interval close to the curvature radius of sample. For each mirror we performed at least 9 CCD frames acquisitions minimum with step of 50 mm centered at its nominal curvature radius. Data have been taken both moving the mirror toward the CCD camera beyond the focal plane and coming back. We illuminated the target with a blue LED and a logarithmic neutral filter (class 2, ND2) to avoid saturation on the CCD.

First operation in set-up preparation is mounting of the mirror on its support and the alignment of its optical axis with respect to that of the light source and detector units. The following step of the procedure is the rough localization of the best focus position. This will be referred as the local origin. The evaluation of the distance between this origin and the camera is obtained from averaged multiple measurements with the laser. Particular

care must be taken in the choice of the reference point, for the local origin measurement, to avoid systematic errors. Single positions of the data set are instead obtained using the encoder mounted along the shaft of the z-axis motor. The random error to be associated to the distance measurement between CCD and mirror will be that one reported by the data-sheet laser meter. At distance of about 35 meters the error will be in the order of 5 mm. The error associated to the encoder is negligible (tenths of microns).

Data reduction of the single image follows standard photometry procedure and software routines (Daophot Photometry Library[30]). After dark and bias frames subtraction, background is evaluated and removed. Due to highly uniform sensitivity of the CCD and not so high requirement in photometric accuracy, flat fielding is not required.

Statistics used to treat the photon flux is Poisson like. So, for a flux of n photons, a photometric error $\sqrt{n}$ is associated [Taylor J., 1996].

The photometric evaluation is obtained with standard aperture photometry (function APER in DAOPHOT). DAOPHOT[30] is designed to work with crowded star fields and small PSF (≈ 10 px). We tested in several conditions that it is well performing also with larger PSF (≈ 500 px) as our mirror case [Bastieri et al., 2007]. The typical PSF image is shown in Figure 96.

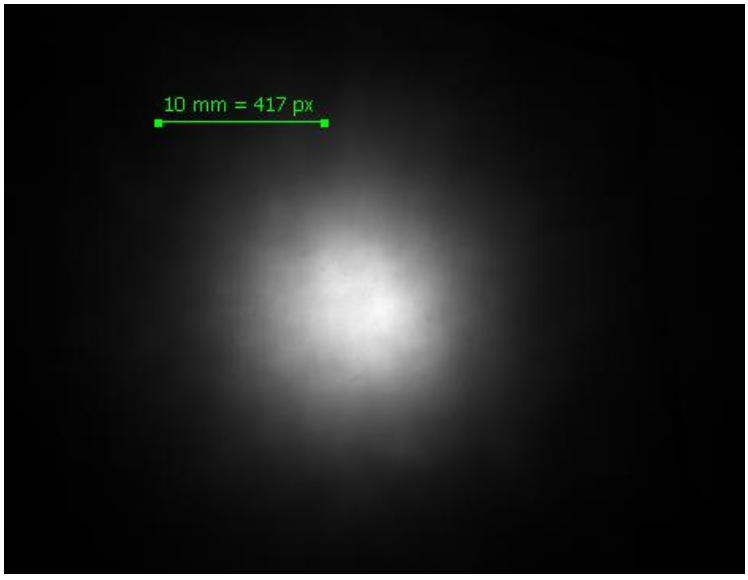

Figure 96: Typical PSF image obtained with the Merate facility.

[30] Daophot Photometry Library (www.star.bris.ac.uk/~mbt/daophot/)

The typical PSF in our frames is spread in about 500x500 pixels per area, with intensity decreasing in Gaussian way across the frame. APER estimates photon counts contained into circular apertures with increasing radii. R80 is defined as the radius of the circular aperture containing the 80% of the total photon flux. The more PSF photons are spread on the CCD frame, the more R80 will increase.

As already said the routine APER also estimates background and subtracts its value from PSF counts. The slope in the outer part of the photometric curve of Figure 97 is very sensitive to this estimation, and it can be used to check if some systematic effect is present. Only photometric curves with asymptotic behaviours in the outer parts are correct (central curve). We can note that in the upper curve we underestimated the background of about 150 counts, while there is an overestimation of 600 counts for the bottom curve.

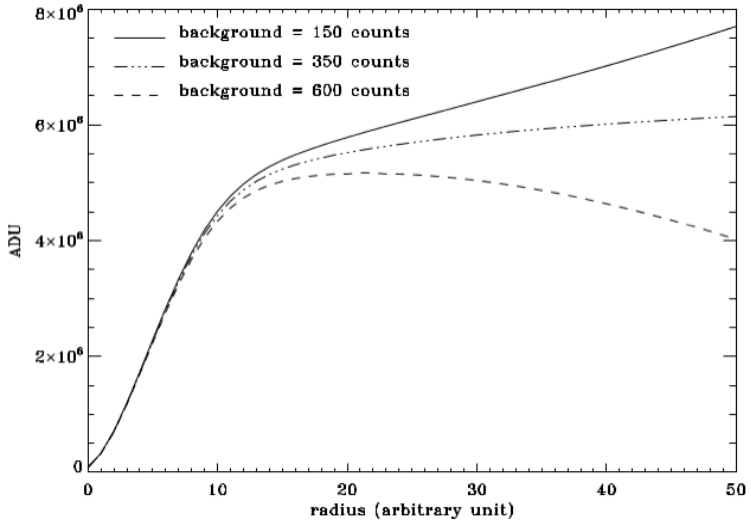

Figure 97: Example of output plot in photometric aperture measurements with different background estimation

The photometry is very sensitive to background because the facility is outdoor. For this reason an independent measurement of the background has been obtained by acquiring images with the mirror shaded. If the weather conditions are stable, only one background estimation for each PSF data set is enough, otherwise several checks along the full acquisition have to be recorded. In order to avoid instrumental bias due to temperature drift of the CCD, the camera shall be cooled and thermally controlled (as shown in Figure 86).

The discussion about the estimation of the R80 error is articulated. We have two contributions to be added in quadrature (independent errors):

- Poisson noise $\sqrt{n}$ related to the photometric counts *n* measured over all PSF area;
- Poisson noise related to the background estimation (for single pixel) [Taylor, 1996].

To convert this estimated error from photon counts into linear units related to R80, a simple operation is performed: using the photometric curve (like in Figure 98) it is possible to define a ring with thickness corresponding to the photometric error.

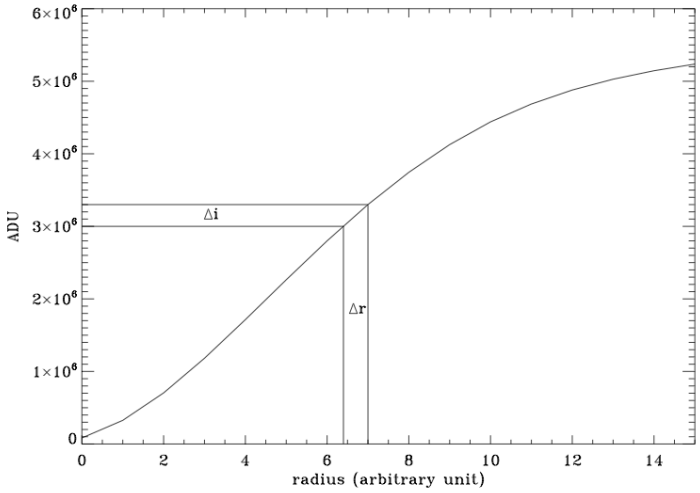

Figure 98: Plot showing error propagation between photometry and R80.

In the tables below, we present the raw data of the five tested mirrors. These measurements will be discussed in the next section.

Mirror 134				
Z [mm]	**R80 [mm]**	**FWHM x [mm]**	**FWHM y [mm]**	**FWHM**
35609	9.72	14.61	8.88	11.39
35659	9.36	13.21	8.21	10.42
35659	9.36	13.23	8.23	10.43
35709	8.93	11.96	7.96	9.76
35709	8.93	12.12	7.91	9.79
35759	8.78	11.19	7.95	9.43
35759	8.71	11.05	7.95	9.37
35809	8.64	10.58	8.34	9.39
35809	8.71	10.60	8.38	9.43
35859	8.85	10.36	9.11	9.72
35909	9.14	10.35	10.18	10.27
35959	9.65	10.67	11.37	11.01
36009	10.15	11.29	12.98	12.11
36059	10.80	12.11	14.52	13.26

Table 4: Data acquired with the Merate outdoor test facility for Mirror 134. Distance from camera to mirror (Z), R80, FWHM (averaged and projected along two reference axes) are reported. All units are in mm.

Mirror 135				
Z [mm]	**R80 [mm]**	**FWHM x [mm]**	**FWHM y [mm]**	**FWHM**
35609	11.37	14.73	10.56	12.47
35659	10.80	14.08	10.48	12.15
35709	10.29	13.71	10.88	12.22
35759	10.08	13.44	11.43	12.39
35809	10.08	13.24	12.01	12.66
35859	10.29	12.91	12.85	12.88
35899	10.51	12.61	13.47	13.04
35909	10.37	12.69	13.63	13.15
35959	10.80	12.64	14.58	13.55
36009	11.16	12.70	15.36	13.97

Table 5: Data acquired with the Merate outdoor test facility for Mirror 135. Distance from camera to mirror (Z), R80, FWHM (averaged and projected along two reference axes) are reported. All units are in mm.

Mirror 136				
Z [mm]	**R80 [mm]**	**FWHM x [mm]**	**FWHM y [mm]**	**FWHM**
35469	12.09	19.43	16.44	17.87
35519	11.52	17.59	15.11	16.31
35569	10.94	16.01	13.92	14.93
35619	10.51	14.58	13.03	13.78
35669	10.01	13.26	12.33	12.79
35719	9.79	12.25	12.01	12.13
35769	9.65	11.53	11.96	11.75
35819	9.57	11.03	12.19	11.51
35869	9.65	10.89	12.67	11.75
35919	10.01	10.92	13.37	12.08
35969	10.37	11.28	14.31	12.71
36019	10.87	11.86	15.43	13.53
36069	11.37	12.61	16.63	14.48
36119	11.66	13.69	18.05	15.72
36169	12.09	14.98	19.39	17.05

Table 6: Data acquired with the Merate outdoor test facility for Mirror 136. Distance from camera to mirror (Z), R80, FWHM (averaged and projected along two reference axes) are reported. All units are in mm.

Mirror 137				
Z [mm]	**R80 [mm]**	**FWHM x [mm]**	**FWHM y [mm]**	**FWHM**
35409	10.80	14.69	13.61	14.15
35459	10.51	13.75	13.01	13.37
35509	10.37	12.98	12.56	12.77
35559	10.22	12.21	12.28	12.29
35609	10.15	11.91	12.20	12.05
35659	10.29	11.65	12.35	11.99
35709	10.44	11.78	12.61	12.19
35759	10.73	12.10	13.05	12.57
35809	11.02	12.68	13.67	13.17

Table 7: Data acquired with the Merate outdoor test facility for Mirror 136. Distance from camera to mirror (Z), R80, FWHM (averaged and projected along two reference axes) are reported. All units are in mm.

Mirror 138				
Z [mm]	**R80 [mm]**	**FWHM x [mm]**	**FWHM y [mm]**	**FWHM**
35359	10.94	13.40	13.90	13.65
35409	10.51	12.41	13.17	12.78
35459	10.08	11.59	12.65	12.10
35509	10.01	11.00	12.25	11.61
35559	10.08	10.57	11.97	11.25
35609	10.08	10.38	11.88	11.11
35659	10.29	10.49	11.97	11.21
35709	10.51	10.89	12.19	11.52
35759	10.87	11.58	12.65	12.10
35809	11.23	12.49	13.17	12.83

Table 8: Data acquired with the Merate outdoor test facility for Mirror 138. Distance from camera to mirror (Z), R80, FWHM (averaged and projected along two reference axes) are reported. All units are in mm.

4.2.4.b Results and Discussion

From the data displayed in the tables above we can analyse properties measured for the five mirrors. An ad hoc IDL routine fits and calculates RoC, R80, FWHM and Astigmatism.

All the data have been evaluated with a second order fit. As usual the minimum of the parabola for RoC, R80, FWHM (in x- and y-axis) has been considered as the measured value for each parameter. The astigmatism has been estimated as the difference between the difference in FWHM along x direction and y one. All the results are reported in the plots of Figure 100- 104.

Comparison with Media Lario results for the same mirrors is the straightforward way to cross calibrate the two measurements methods and facilities. To do this it is important to understand how Media Lario data have been taken. The qualification method is a standard procedure with low requirements in terms of time and manpower. For each mirror, a raster scan 1.5 m deep is obtained, with a discrete distribution of focus positions (step of 10 cm). The PSF is evaluated at each step, and the position corresponding to minimum is

assigned as RoC. This procedure is simple and quick, but leads to a rough estimation of the focus position. Moreover, Media Lario does not report an estimation of the error related to PSFs. For this reason, a comparison in terms of cross-calibration of the two facilities is not trivial.

Plots of the measurements obtained with the facility for the individual mirrors are reported below. Looking at our dataset and the reduced measurements (PSF, FWHM, RoC, Astigmatism), we infer the following general consideration:

- While an automated fit is used in our method the evaluation of RoC, in Media Lario procedure the measured RoCs are produced by a discrete distribution. In our case the estimation of our measurements is affected by an error at maximum of $\pm$5mm;
- RoC range is very similar in the two data sets, and it spans roughly between 35600 mm and 35800 mm and our evaluations of RoCs have differences at maximum of 10 cm with respect to Media Lario ones (last column). The reason is easily associated with the measurement process performed by Media Lario. Merate facility shows a higher precision in the RoC evaluation than Media Lario one.

Only our dataset has been exploited for measuring astigmatism. Most of the mirrors show this effect (an example is shown in

Figure 99). As discussed previously this aberration is due to a different behaviour of the honeycomb supporting the glass in the two perpendicular directions. Astigmatism range is 150 - 600 mm. The minimum astigmatism measured in our sample is about 15 cm, but likely astigmatism of 5 cm could be easily detected. In particular mirrors 135 and 137 are affected by a severe astigmatism.

- R80 range is [9.5 – 12] mm in Media Lario dataset and [8.5 -10] mm in our measurements. R80 evaluated by Media Lario shows a systematic increase of about 1 mm with respect to our measurements. This can be due to the lower accuracy in focus determination in the Media Lario procedure. Moreover any error estimation on this dataset is not provided, so further more accurate considerations are not possible.
- The plots underline an important consideration: for regular PSF (circular patterns and symmetric structures) the FWHM fitting is a better method to evaluate focus position. R80 method is a noisy but robust process when not Gaussian profiles of the PSF are present. For this reason both procedures must be carried out in data reduction.

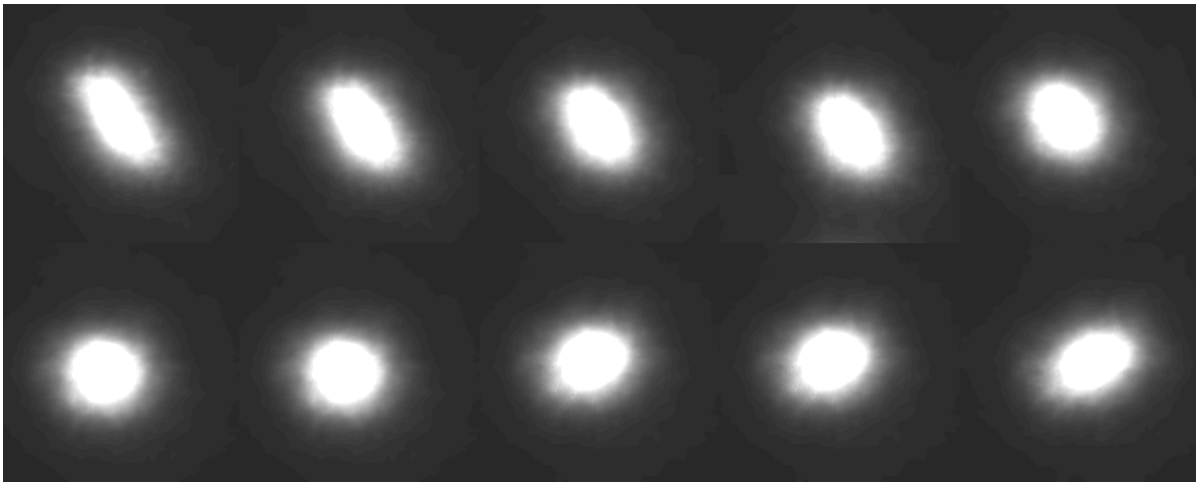

Figure 99: Sequence of frames taken at different focus depths for an astigmatic mirror.

Mirror ID	RoC (R80 meth.)	RoC (FWHM meth.)	Astigmatism |RoC x-RoC y|	R80	FWHM	RoC (by R80) MLT	R80 MLT	.RoC (R80 method)-RoC (by R80) MLT
134	35794	35792	157	8,73	9,41	35700	10,25	94
135	35810	35670	480	10,11	12,29	35800	9,75	10
136	35808	35828	157	9,71	11,66	35800	10,55	8
137	35592	35641	616	10,2	12,02	35700	12,15	108
138	35560	35608	174	10,02	11,15	35600	10,15	40

Table 9: Report of the properties measured for five mirrors under testing, and comparison with Media Lario numbers. All quantities in units of mm.

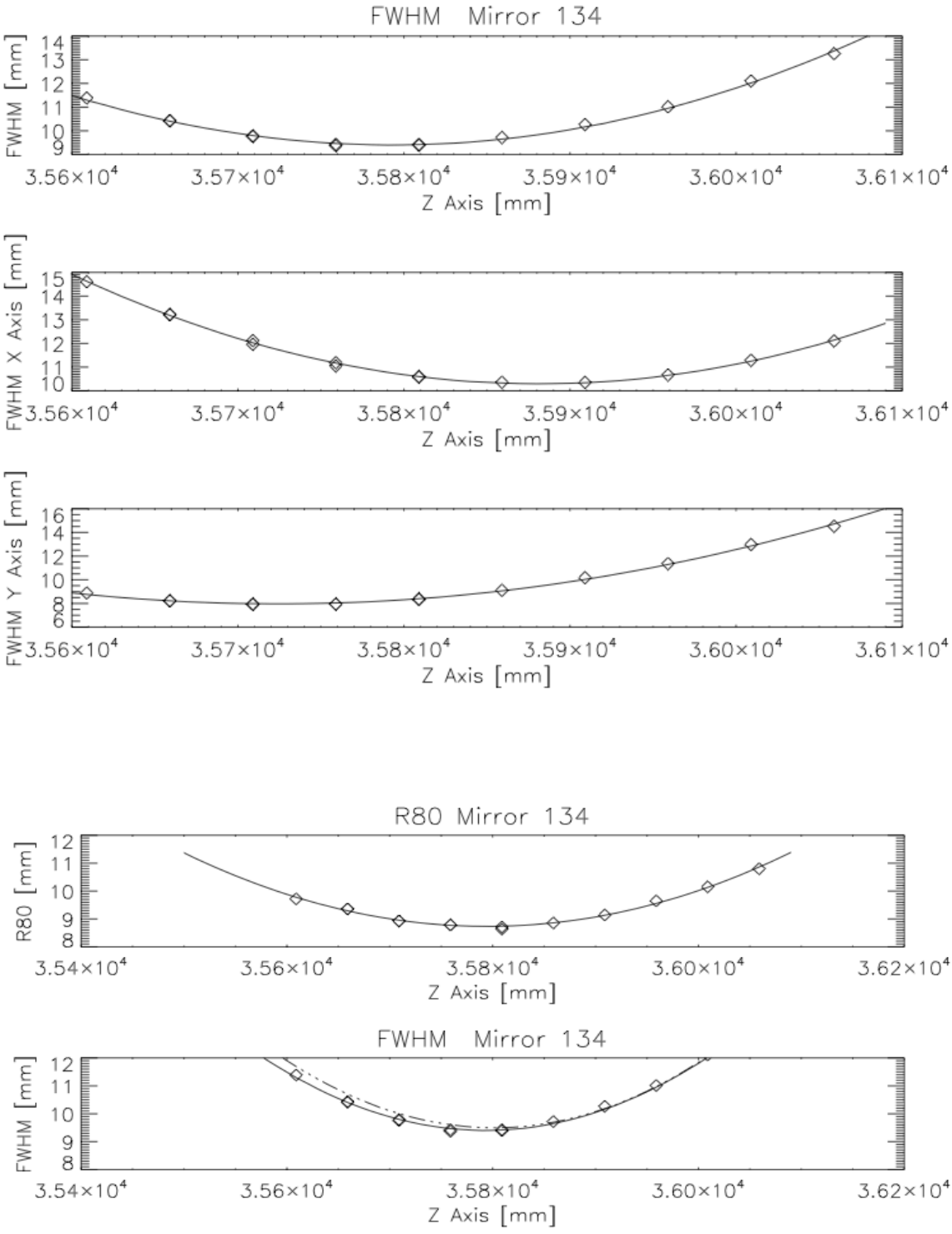

Figure 100: Mirror 134. Top: Estimation of astigmatism (Integral FWHM, along x and along y). Bottom: Comparison between R80 and FWHM.

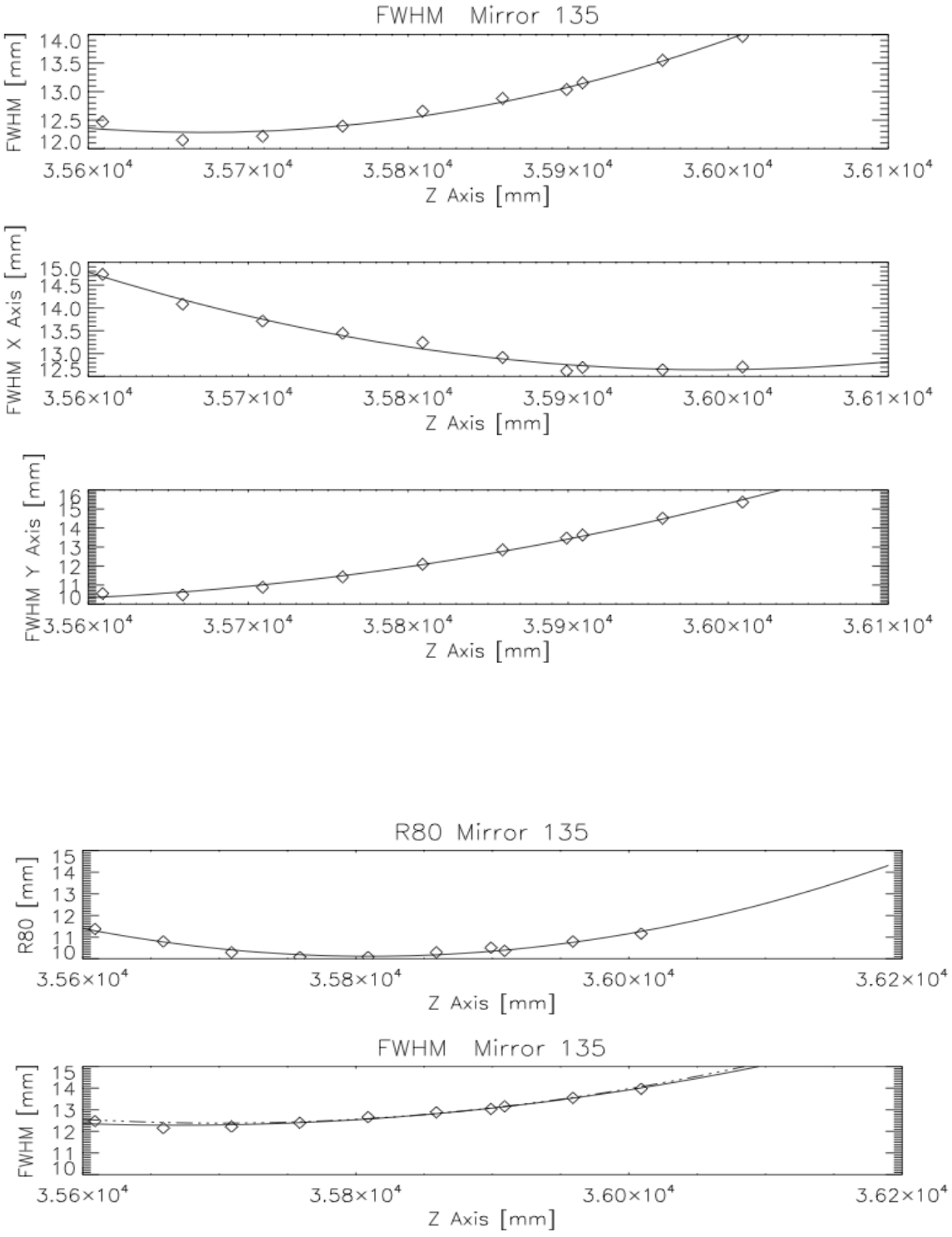

Figure 101: Mirror 135. Top: Estimation of astigmatism (Integral FWHM, along x and along y). Bottom: Comparison between R80 and FWHM.

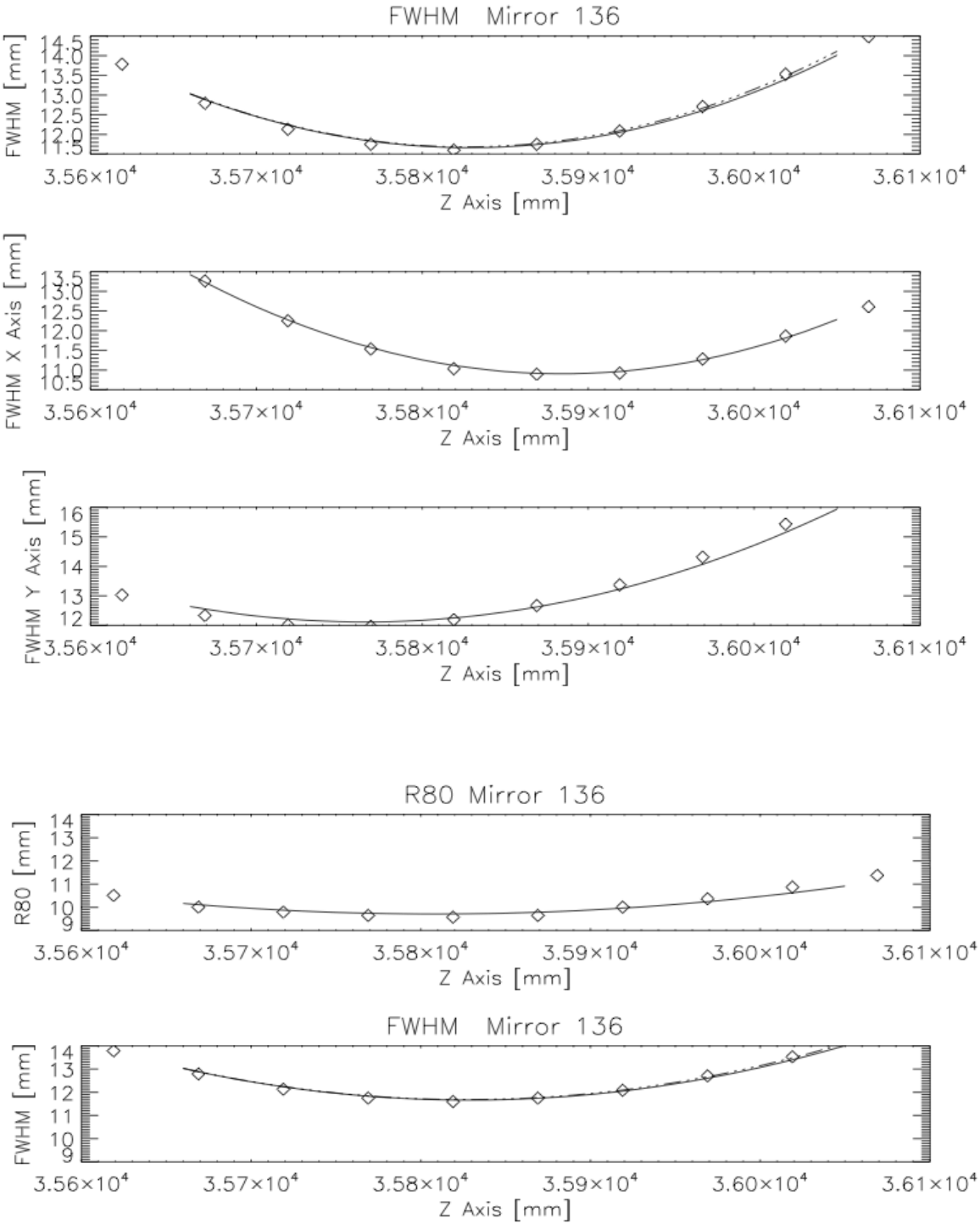

Figure 102: Mirror 136. Top: Estimation of astigmatism (Integral FWHM, along x and along y). Bottom: Comparison between R80 and FWHM.

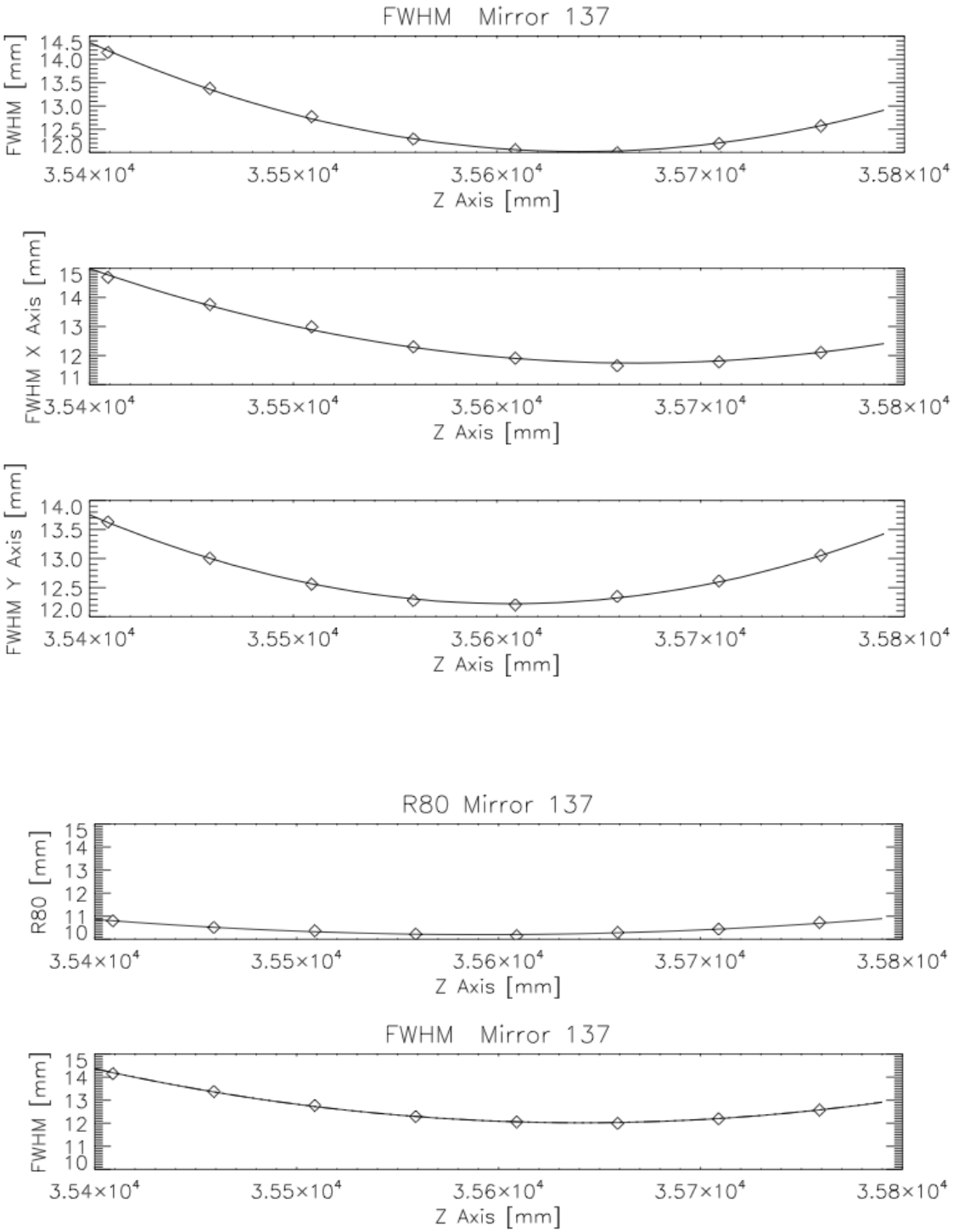

Figure 103: Mirror 137. Top: Estimation of astigmatism (Integral FWHM, along x and along y). Bottom: Comparison between R80 and FWHM.

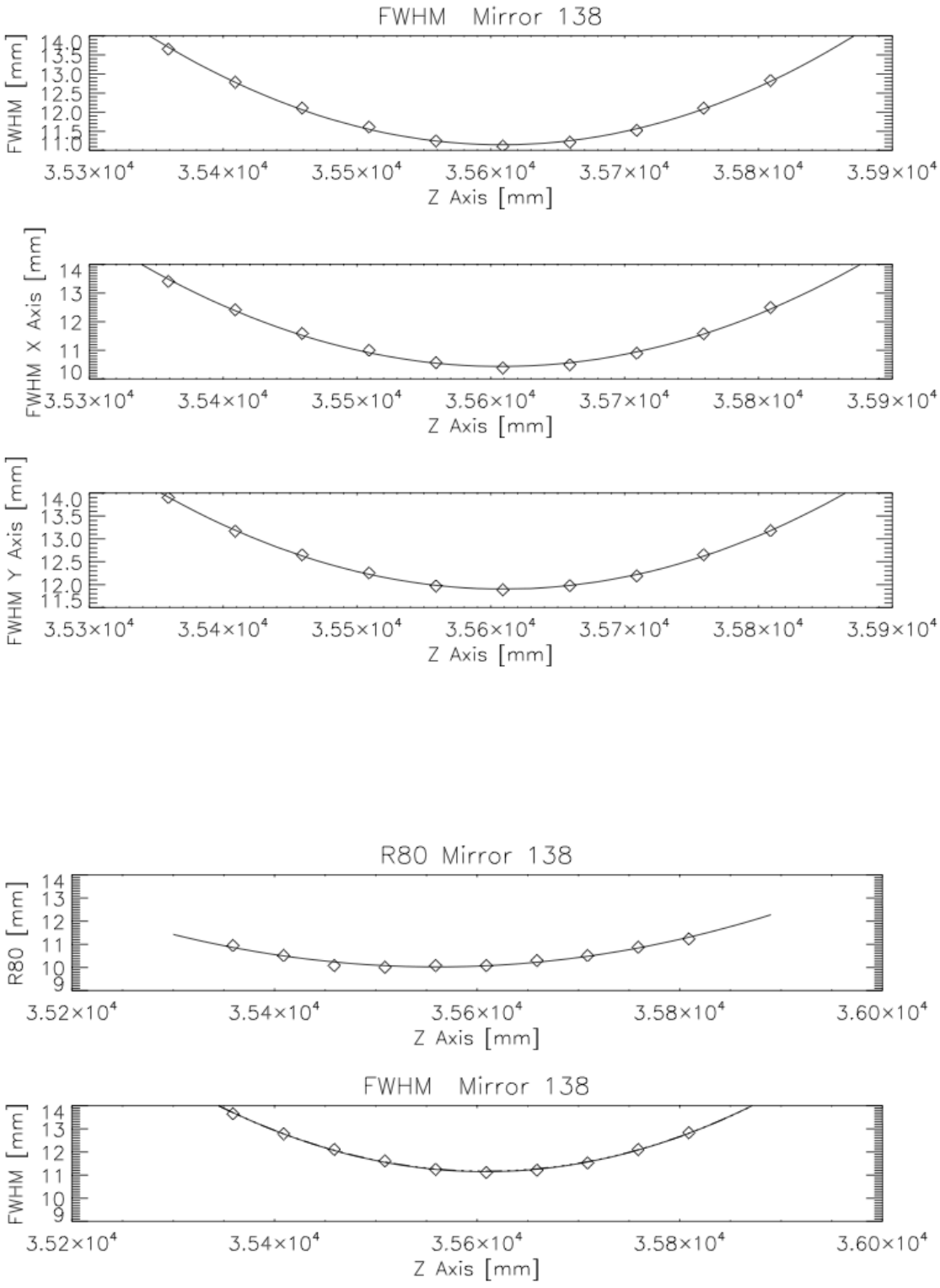

Figure 104: Mirror 138. Top: Estimation of astigmatism (Integral FWHM, along x and along y). Bottom: Comparison between R80 and FWHM.

4.2.5 DISH DISTRIBUTION AND PSF STATISTICS OF THE MIRRORS

Due to the relatively large number of mirrors that has been produced, some statistical analysis of the distribution of the curvature radii and PSF can be carried out. Indeed, these two properties are correlated to the dish distributions. In fact, the angular PSF measured on the focal plane of the telescope will be up to the following two factors:

- $\Delta R_i = |R_{nom,i} - R_{meas,i}|$, where for each mirror i ΔR_i is the difference between nominal curvature radius and the actual one. $R_{nom,i}$ is the nominal curvature radius as defined by MAGIC required distribution [Garczarczyk, 2014], $R_{meas,i}$ is the best curvature radius measured in Media Lario, namely the curvature radius corresponding at the smallest PSF.

- The intrinsic PSF of the mirror is the PSF corresponding to the best curvature radius.

Following Doro [Doro, 2009], to calculate the final linear PSF for each mirror we have to estimate the defocus effect ΔS_i due to ΔR_i by combining it with the intrinsic PSF. Due to the fact that the two aberrations are linearly independent, we sum the-m in quadrature mode.

We define the increasing spot size due to defocus $\Delta S_i = \theta \Delta f$ where the focal length $f = \frac{R}{2}$, $\theta = \frac{d}{f} = \frac{1m}{17m} \rightarrow \Delta S = \frac{\Delta R}{2 \cdot 17}$ if we have an error in the curvature radius of 100 mm the increasing defocus will be about 3 mm.

Following the data delivered by Media Lario, we can obtain the radii distribution from the shortest to the largest one to compare with radii nominal distribution indicated by MAGIC Collaboration (Figure 105).

The plot shows well the bimodal distribution of the mirror production. Mirror RoC distribution is driven by the mould RoC. In fact only two moulds have been used. Media Lario used the spring-back effect during the gluing process, to obtain several mirrors with different curvatures from the one of the master. Anyway the central part of distribution is less crowded then the wings.

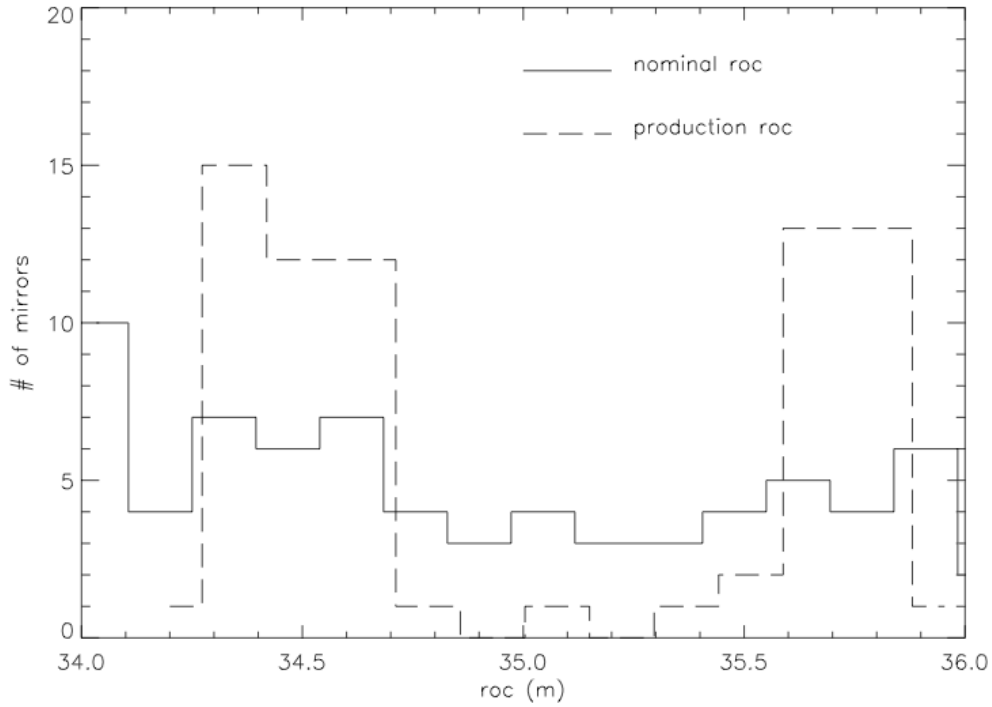

Figure 105: Curvature radii distribution of the Media Lario production (dashed line) compared with the desired one (solid line).

Despite the two different distributions, the median of the difference between the nominal and the actual RoC is less then 100 mm, i.e. 3 mm of defocus enlargement on the telescope focal plane.

$$Median\ (nominal\ RoC - actual\ RoC) = -96\ mm$$

We discuss now about the intrinsic PSF distribution to understand if ΔR_i introduces a significant PSF enlargement.

$$Mean\ r80\ @\ roc = 11.9 \pm 1.3\ mm$$

The distribution is approximately Gaussian and all the mirrors are inside the goal of 1mrad (as indicated in the identity card, Figure 93). In Figure 107 the real statistical

distribution of R80 on the focal plane combined with the defocus related to each mirror is shown. For this reason the distribution now is:

$$\textit{Mean R80 defocused @ focal plane} = 12.7 \pm 1.4 \ \textit{mm}$$

One can see by the figure that the distribution is a bit larger than the previous one, but anyway few mirrors have a radius larger than 15 mm. In particular the mean diameter of the PSF is inside the pixel size of MAGIC camera (25.4 mm), fitting the design specifications of the telescope.

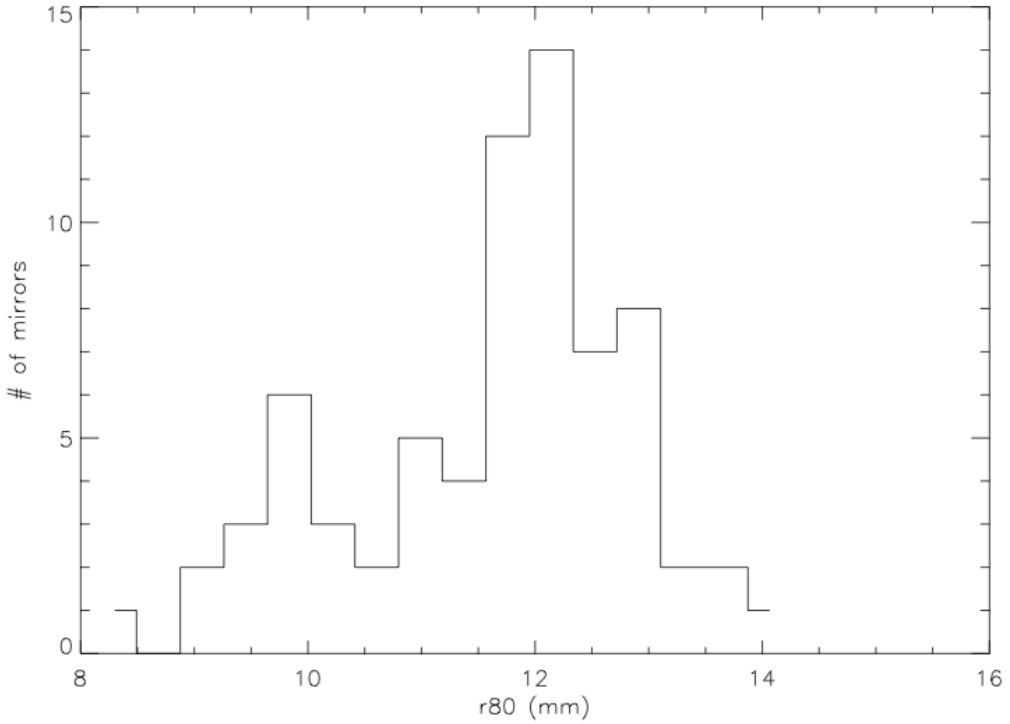

Figure 106: Statistical distribution of R80 at RoC for the 72 MAGIC mirrors produced by MLT.

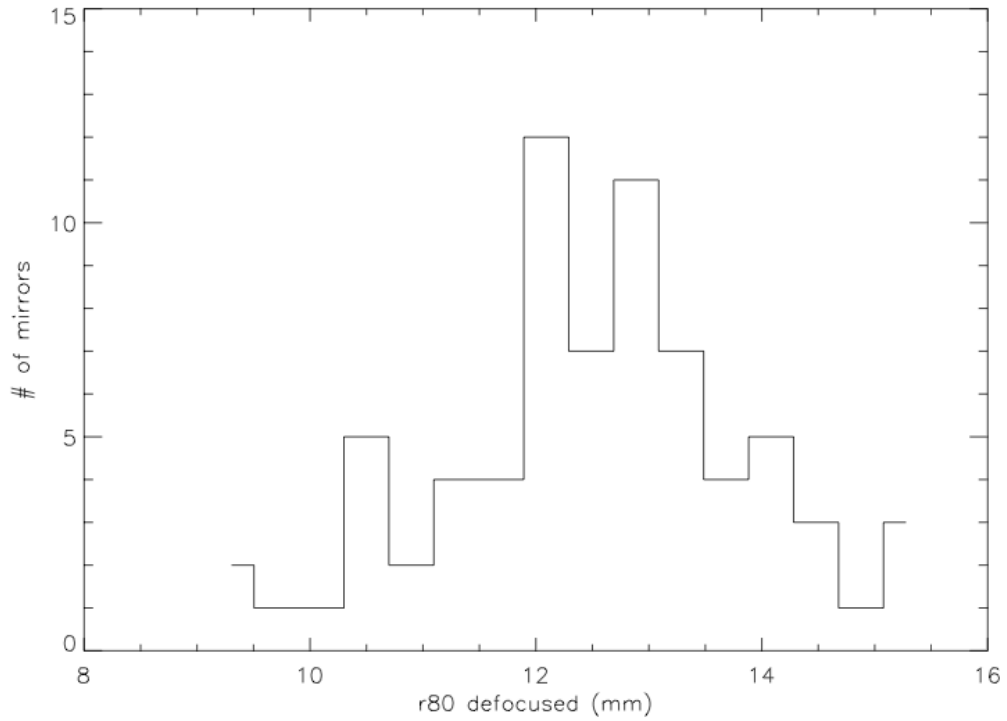

Figure 107: Statistical distribution of R80 defocused at focal plane of MLT.

Chapter V

CONCLUSIONS AND FUTURE PERSPECTIVES

To reach new limits of the astrophysical investigations a great improvement in technology efforts has been carried out and more else has to be developed. As largely illustrated in this work, IACT represents cost-effective and promising technique to observe in high-energy scenario. A quick evolution of the Cherenkov instruments seems to be started, and CTA represents the next generation of telescopes.

This work has started by a detailed analysis of the properties needed to fulfill mirror requirements for present and future generation of telescopes such as CTA, to arrive to discuss how a facility for mirror characterization has to be designed and how to work in this framework. In particular the facility of Merate has been described in details and optical tests on a sample of mirror panels mounted on MAGIC telescopes in summer 2014 have been here carried out. The measurement process performed by Merate Facility shows a higher precision than Media Lario one, anyway probing that the production and the optical requirements are fulfilled.

This work took part to the definition of the installation plan for the last mirror production for the MAGIC reflecting surface and contributed to make full operative the Mirror Test Facility of Merate in CTA framework.

Nowadays Merate Facility is fully integrated in the mirror test facilities network of CTA (the cross-calibration with the other facilities scheduled in 2015), and ready to give its contribution for mirror testing and cross-calibration of the huge industrial production of optical panels needed to realize the worldwide project CTA.

Part of this work has contributed to a paper submitted to Nuclear Instruments and Methods in Physics Research (*A facility to evaluate the focusing performance of mirrors for Cherenkov Telescopes*, Authors: Canestrari R., Giro E., Bonnoli G., Farisato G., Lessio L., Rodeghiero G., Spiga R., Toso G., Pareschi G.).

BIBLIOGRAPHY

1. Aloisio A. et al., The ARGO-YBJ experiment in Tibet, Il Nuovo Cimento 24C, 4-5, 739, 2001
2. Actis M. et al., The CTA Consortium, Design Concepts for the Cherenkov Telescope Array CTA: an advanced facility for ground-based high-energy gamma-ray astronomy, Experimental Astrononomy, 2011
3. Aharonian F. et al., The H.E.S.S. survey of the inner galaxy in very high energy gamma rays, The Astrophysics Journal, 636:777-797, 2006
4. Aharonian F. A., Akhperjanian A.G., Measurement of the radial distribution of Cherenkov light generated by TeV gamma-ray air showers, HEGRA Collaboration, Astroparticle Physics 10, 21-29, 1999
5. Aharonian F. A., Very high energy cosmic gamma radiation: a crucial window on the extreme Universe, River Edge, NJ: World Scientific Publishing, 2004
6. Aharonian, F. A., The Very-High-Energy Gamma-Ray Sky, Science, 315, 70, 2007
7. Aharonian F. A., Towards a Major Atmospheric Cerenkov Detector III, Tokyo, 1994
8. Akhperjanianet A. et al., The Optical Layout of The Hegra Cherenkov Telescopes, Experimental Astronomy, 8, 135-152, 1998
9. Aleksić J. et al., The major upgrade of the MAGIC telescopes, Astroparticle Physics, In press, 2015
10. Atwood W. B. et al. (Fermi/LAT Collaboration), The Large Area Telescope on the Fermi Gamma-ray Space Telescope Mission, Astrophysics Journal, 697-1071, 2009
11. Bastieri D. et al., The Mirrors for the MAGIC Telescopes, Proc. of 29th International Cosmic Ray Conference (ICRC), 5, 283-286, 2005
12. Bastieri D. et al., The reflecting surface of the MAGIC-II Telescope, International Cosmic Ray Conference (ICRC), 2007
13. Bennett J.M., Mattsson L., Introduction to Surface Roughness and Scattering, OSA The Optical Society, 1993
14. Bernlhör et al., The optical system of the H.E.S.S. imaging atmospheric Cherenkov telescopes, Astropart.Phys. 20, 111-128, 2003
15. Blackett P.M.S., Cloud chamber researches in nuclear physics and cosmic radiation, Nobel Lecture, December 13,1948
16. Bonardi A. et al., A new solution for mirror coating in γ-ray Cherenkov Astronomy, Exp Astron., 38, 1, 2014
17. Bonnoli G. et al., Reflective and antireflective coatings for the optical chain of the ASTRI SST-2M prototype, SPIE, 8861, 17, 2013
18. Born M., Wolf E., Principles of Optics, Cambridge University Press, 1999

19. Bradt H., Astrophysics Processes, The Physics of Astronomical Phenomena, Cambridge University Press, 2014
20. Buckley J., The Advanced Gamma-ray Imaging System (AGIS), American Physical Society Meeting and HEDP/HEDLA Meeting (meetings.aps.org/link/BAPS.2009.APR.E1.9) , 2008
21. Canestrari et al., Investigation of a novel slumping technique for the manufacturing of stiff and lightweight optical mirrors, SPIE, 7018, 0, 2008
22. Canestrari et al., The Italian ASTRI program: an end-to-end dual-mirror telescope prototype for Cherenkov light imaging above few TeV, 32nd International Cosmic Ray Conference (ICRC), Beijing, 9, 116, 2011
23. Canestrari R. et al., Composite panels for optical mirrors for Cherenkov telescopes: development of the cold glass slumping technology, SPIE, 7739, 0, 2010
24. Canestrari R. et al., Techniques for the manufacturing of stiff and lightweight optical mirror panels based on slumping of glass sheets: concepts and results, SPIE, 7437, 11, 2009
25. Canestrari R., Giro E., Bonnoli G., Farisato G., Lessio L., Rodeghiero G., Spiga R., Toso G., Pareschi G., A facility to evaluate the focusing performance of mirrors for Cherenkov Telescopes, Submitted to Nuclear Instruments and Methods in Physics Research, 2015
26. Canestrari R., Pareschi G. et al., Cold-shaping of thin glass foils as novel method for mirrors processing: from the basic concepts to mass production of mirrors, Optical Engineering, Special edition on Optical Materials, 52, 1204, 2013
27. Canestrari R., Thin glass sheets for innovative mirrors in astronomical applications, PhD Thesis, 2009
28. Canestrari, R.; Greenshaw, T.; Pareschi, G.; White, R., Technological developments toward the small size telescopes of the Cherenkov Telescope Array, SPIE, 8844, 39, 2012
29. Carrigan S. et al., The H.E.S.S. Galactic Plane Survey - maps, source catalog and source population, International Cosmic Ray Conference (ICRC), ArXiv:1307.4690, 2013
30. Cherenkov, Visible Radiation Produced by Electrons Moving in a Medium with Velocities Exceeding that of Light, Phys. Rev. 52, 378, 1937
31. Couder, A., Sur un type nouveau de télescope photographiqu, Compt. Rend. Acad. Sci., Paris, 1926
32. Chadwick P. M et al., The Formation of Condensation on Cherenkov Telescope Mirrors, Proc. 33rd International Cosmic Ray Conference (ICRC), ArXiv:1307.6313, 2013
33. CTA Consortium, Common Technology Evaluation, Testing and Calibration Technical Design Report, COM-TDR/140721 | v.5.1 | CTA Consortium, May 2015
34. Curie Marie Sklodowska, Traité de radioactivité, 1910
35. Daum A. et al, First results on the performance of the HEGRA IACT array, Astropart. Phys., 8, issue 1-2, 1, 1997
36. Davies J.M., Cotton E.S., "Design of the Quartermaster Solar Furnace", Solar Energy Sci. Eng., 1, 16,1957
37. De Angelis A., Domenico Pacini: uncredited pioneer of the discovery of cosmic rays, Il Nuovo

Cimento, arXiv:1103.4392, 2011
38. De Angelis A. et al., Very High Energy Gamma Astrophysics, Il Nuovo Cimento, 31, 4, 2008
39. Doro M. et al., The reflective surface of the MAGIC telescope, Nuclear Instruments and Methods in Physics Research, 595, 200, 2008
40. Doro M., Novel Reflective Elements and Indirect Dark Matter Searches for MAGIC II and Future IACTs, PhD Thesis, 2009
41. Doro M., Technical Solutions for the MAGIC Telescope, Astroparticle, Particle and Space Physics, 170-174, 2007
42. Doro M., The Reflective Surface of the MAGIC Telescope, International Workshop on Ring Imaging Cherenkov Counters (RICH), 2007
43. Einstein A., Zur Elektrodynamik bewegter Körper, Annalen der Physik, Band 17, 132, 1905
44. Fazio, G. et al., An experiment to search for discrete sources of cosmic gamma rays in the 1011 to 1012 eV region, Canadian Journal of Physics, 46, S427-S432, 1968
45. Feenberg E., Primakoff H., Interaction of Cosmic-Ray Primaries with Sunlight and Starlight, Phys. Rev. 73, 449, 1948
46. Fermi E. Phys. Rev., 75, 1169, 1949
47. Finnegan G.M., High energy gamma-ray astronomy observations of Geminga with the VERITAS array, PhD Thesis, 2012
48. Förster A., Dielectric Coatings for IACT Mirrors, International Cosmic Ray Conference (ICRC), arXiv1307.4557, 2013
49. Galbraith W., Jelley J. V., Light Pulses from the Night Sky associated with Cosmic Rays, Nature, 171, 349, 1953
50. Gao H. et al., Compton scattering of self-absorbed synchrotron emission, Monthly Notices of the Royal Astronomy Society, 435, 2520, 2013
51. Landau L.D., Lifshitz E.M., The Classical Theory of Fields (Vol. 2 of "A Course of Theoretical Physics"), Pergamon Press, 1971
52. Garczarczyk M., et al., The Active Mirror Control of the MAGIC Telescope, Proc. the 28th International Cosmic Ray Conference (ICRC), 2935, 2003
53. Garczarczyk M., Specifications of the Media Lario mirrors for the 2014 mirror exchange in MAGIC-I and MAGIC-II, MAGIC Internal Report, 2014
54. Gehrels N., Michelson P., "GLAST: the next-generation high energy gamma-ray astronomy mission", Astroparticle Physics, 11, 277, 1999
55. Ghigo M. et al., Novel "cold" slumping glass technology for making the XEUS mirror optics, XEUS workshop, ESTEC, 2008
56. Ghigo M. et al., Development of hot slumping technique and last optical performances obtained on a 500 mm diameter slumped segment prototype for adaptive optics, SPIE, 7439, 0, 2009
57. Ghigo, M. et al., Slumped glass option for making the XEUS mirrors: preliminary design and ongoing development, SPIE, 7011, 1, 2008
58. Giacconi R., Gursky H., Paolini F. R., Rossi B., Evidence for x Rays from Sources Outside the

Solar System, Phys. Rev. Lett. 9, 439, 1962
59. Giro E., Cold-slumped glass mirrors, ASPERA Technology Forum, Pisa, 2011
60. Giro E., Mirrors for CTA telescopes, CTA Industry, Roma, 2013
61. Goebel F., Status of the second phase of the MAGIC telescope, Proceedings of the 30th International Cosmic Ray Conference (ICRC), 3, 1485, 2008
62. Greisen K., End to the Cosmic-Ray Spectrum?, Physical Review Letters 16, 748, 1966
63. Hayakawa S. Prog. Theor. Phys. 8, 255, 1952
64. Hecht E., Optics (4th Edition). Addison Wesley, 2002
65. Heinrich J. Völk, Felix A. Aharonian, TeV Gamma-Ray Astrophysics: Theory and Observations Presented at the Heidelberg Workshop 1994, Springer, 2012
66. Hermann G., The ground-based gamma-ray observatory CTA, Astronomische Nachrichten, 328, 7, 593, 2007
67. Heß M. et al., The time structure of Cherenkov images generated by TeV γ-rays and by cosmic rays, HEGRA Collaboration, Astroparticle Physics 11, 363, 1999
68. Hess V., Phys. Z., 13, 1084, 1913
69. Hillas A. M., Cerenkov light images of EAS produced by primary gamma, 19th International Cosmic Ray Conference, 3, 445, 1985
70. Hillas A. M. et al., ApJ, 503, 744, 1998
71. Hillas A. M., Cosmic rays. New York: Pergamon Press, 1972
72. Hillas A. M.,The Origin of Ultra-High-Energy Cosmic Rays, Annual Review of Astronomy and Astrophysics, 22, 425, 1984
73. Hillas A. M.,The sensitivity of Cerenkov radiation pulses to the longitudinal development of cosmic-ray showers, J. Phys. G: Nucl. Phys. 8, 1475, 1982
74. Hofmann W. et al, Comparison of techniques to reconstruct VHE gamma-ray showers from multiple stereoscopic Cherenkov images, Astroparticle Physics, 12, 135, 1999
75. Hofmann W., Status of the H.E.S.S. project, Proceedings of the 27th International Cosmic Ray Conference (ICRC), 7, 2785, 2001
76. Holder J., TeV Gamma-ray Astronomy: A Summary, Astroparticle Physics, 39, 61, 2012
77. Jelley J. V., Cerenkov Radiation and Its Applications, Londra, Pergamon Press, 1958
78. Kildea J. et al., The Whipple Observatory 10 m gamma-ray telescope, 1997–2006, Astroparticle Physics 28, 182, 2007
79. Knauer M. C., Kaminski J., Häusler G., Phase measuring deflectometry: a new approach to measure specular free-form surfaces, in Photonics, Optical Metrology in Production Engineering, SPIE, 5457, 366, 2004
80. La Rocca P. et al., Fabrication, characterization and testing of silicon photomultipliers for the Muon Portal Project, submitted to Nuclear Instruments and Methods in Physics Research, 787, 1, 236‑239, 2015
81. Lamanna G., Very High Energy Phenomena in the Universe, Rencontres de Moriond - La Thuile, 2013

82. Longair M. S., High Energy Astrophysics, Cambridge University Press, Third Edition, 2011
83. Lorenz E., The MAGIC Telescope Project Description, Contributions to the Kruger National Park Workshop, 1997
84. Lorenz E. et al., The MAGIC Telescope Project, The MAGIC Collaboration, AIP Conference Proceedings, 515, 510, 1999
85. Meagher K. J., Schwarzschild-Couder Telescope for the Cherenkov Telescope Array, Proceedings of the SPIE, 9145, id. 914533, 2014
86. Mehra J., Rechenberg H., The Historical Development of Quantum Theory, Vol. 1: The Quantum Theory of Planck, Einstein, Bohr and Sommerfeld. Its Foundation and the Rise of Its Difficulties (1900-1925), New York, Springer-Verlag, 1982
87. Michelson P., Instrumentation for the Gamma-ray Large Area Space Telescope (GLAST) mission, Proceedings of the SPIE, 4851, 1144-1150, 2003
88. Mirzoyan R. et al., On the optical design of VHE gamma ray imaging Cherenkov telescopes, Nucl. Instr. Methods A, 373,153-158, 1996
89. Mirzoyan R., Brief history of ground-based very high energy gamma-ray astrophysics with atmospheric air Cherenkov telescopes, Astroparticle Physics 53, 91-99, 2014
90. Mirzoyan, R., Andersen M.I., A 15° wide field of view imaging air Cherenkov telescope, Astroparticle Physics, 31, 1-5, 2009
91. Mirzoyan, R., On the Calibration Accuracy of Light Sensors in Atmospheric Cherenkov Fluorescence and Neutrino Experiments, Proc. ICRC, 7, 265, 1997
92. Morrison, P., On the Origins of Cosmic Rays, Rev. Mod. Phys. 29, 235, 1957
93. Morrison, P., Stanislaw O., Rossi B., The Origin of Cosmic Rays, Phys. Rev. 94, 440, 1954
94. Pacini D., La radiazione penetrante alla superficie ed in seno alle acque, Il Nuovo Cimento 26, 96, 1912
95. Pareschi G. et al., Status of the technologies for the production of the Cherenkov Telescope Array (CTA) mirrors, Proc. SPIE 8861, 03, 2013
96. Pareschi G., Giro E. et al., Glass Mirrors by cold slumping to cover 100 m^2 of the MAGIC II Cherenkov telescope reflecting surface, Advanced Optical and Mechanical Technologies in Telescopes and Instrumentation, SPIE, 7018, 2008
97. Planck M., The theory of heat radiation, P. Blakiston's Son & Co., Philadelphia, 1914
98. Rao M., Extensive Air Showers, World Scientific, 10, 1998
99. Riess A. et al., Time Dependence of the CTE from Cosmic Ray Tails, Instrument Science Report WFPC2 99-04, 1999
100. Rodeghiero G., Optical design study, testing and qualification of a Schwarzschild-Couder telescope for CTA and an assessment on the Intensity Interferometry capabilities with CTA, PhD Thesis, 2015
101. Ronchi V., Due nuovi metodi per lo studio delle superfici e dei sistemi ottici, Annali della Scuola Normale Superiore di Pisa - Classe di Scienze, Series 1, 15, 1-50, 1927
102. Rossi B., High-Energy Particles, Prentice-Hall, New York, 1952

103. Rossi B., Cosmic rays, McGraw-Hill, 1964
104. Rousselle J. et al., Schwarzschild-Couder telescope for the Cherenkov Telescope Array: Development of the Optical System, SPIE, 8861, 2013
105. Rutherford E., The magnetic and electric deviation of the easily absorbed rays from radium, Philosophical Magazine, Series 6, 5, 26, 177-187, 1903
106. Sahakian V., Aharonian F., Akhperjanian A., Cherenkov light in electron-induced air showers, Astroparticle Physics, 25 (4), 233-241, 2006
107. Schliesser A., Mirzoyan R., Wide-field prime-focus imaging atmospheric Cherenkov telescopes: A systematic study, Astroparticle Physics 24, 382-390, 2005
108. Schroeder D. J., Astronomical Optics, San Diego Academic Press, 1999
109. Schultz C., Doro M., Mariotti M., Lessio L., Open Glass-Steel Structure Mirrors for the LST, CTA Meeting Turku, 2015
110. Schulz A., Methods for the characterization of mirror facets for Imaging Atmospheric Cherenkov Telescopes, ECAP, ICRC, 2011
111. Schwarzschild K., Untersuchungen zur geometrischen Optik, Astron. Mitt. Konig. Sternwarte, Gottingen, 1905
112. Shapiro M. M., Stanev T., Wefel J. P., Astrophysical Sources of High Energy Particles and Radiation, Springer, 2001
113. Sironi G. et al., Deflectometry for optics evaluation: Freeform segments of polynomial mirror, Proc. SPIE 9151, Advances in Optical and Mechanical Technologies for Telescopes and Instrumentation, 91510T, 2014
114. Stecker F. W., Diffuse Cosmic Gamma rays: Present Status of Theory and Observations, Nature Physical Science, 241, 74-77, 1973
115. Strazzeri E., Bonnoli G., Lombardi S., Maccarone M.C., Mineo T., for The Astri Collaboration, Calibration of the ASTRI SST-2M Prototype using Muon Ring Images, Procs. 33rd International Cosmic Ray Conference (ICRC), 2013
116. Striani E. et al., The Crab Nebula super-flare in 2011 April: extremely fast particle acceleration and gamma-ray emission, The Astrophysical Journal Letters, 741, L5, 2011
117. Tavani M., The AGILE Gamma-Ray Mission, American Astronomical Society, 10, 28, 2008
118. Tavecchio F., Maraschi L., Ghisellini G., Constraints on the physical parameter of TeV blazars, ApJ, 509, 608, 1998
119. Taylor J., An Introduction to Error Analysis: The Study of Uncertainties in Physical Measurements, Paperback, 1996
120. Terebizh V. Yu., Two-mirror Schwarzschild aplanats: basic relations, Astronomy Letters, 31, 2, 129–139, 2005
121. Vassiliev V., Fegan S. J., Brousseau P. F. et al., Wide field aplanatic two-mirror telescopes for ground-based γ-ray astronomy, Astroparticle Physics, 28, 2007
122. Vassiliev V., Medium-Size prototype Schwarzschild-Couder Telescope, CTA Meeting, 2015
123. Vercellone S. et al., On behalf of the ASTRI Collaboration, The ASTRI Project: prototype status

and future plans for a Cherenkov dual-mirror small-telescope array, 4th Fermi Symposium, http://arxiv.org/abs/1303.2024v2, 2013

124. Vernani D. et al., Development of cold-slumping glass mirrors for imaging Cherenkov telescopes, Proc. of SPIE, 70180V-1, 2008
125. Weekes T.C., et al., Observation of TeV gamma rays from the Crab nebula using the atmospheric Cerenkov imaging technique, Astrophysical Journal, Part 1, 342, 379-395, 1989
126. Weekes T.C., et al., VERITAS: the very energetic radiation imaging telescope array system, Proceedings of the 25th International Cosmic Ray Conference (ICRC), 1997
127. Weekes T.C., The Atmospheric Cherenkov Technique in Very High Energy Gamma-Ray Astronomy, Space Science Reviews, 75, Issue 1-2, 1-15, 1996
128. Willstrop R. V., The modified Couder Telescope, Monthly Notices of the Royal Astronomical Society 209, 587-606,1984
129. Wilson T., Reflecting Telescope Optics I: Basic Design Theory and its Historical Development, Second Ed., Springer Science & Business Media, 2007
130. Wyman C. L., Korsch D., Aplanatic Two-Mirror Telescopes; a Systematic Study. The Schwarzschild-Couder Configuration, Applied Optics,14, 4, 1975
131. Zatsepin, G. T., Kuzmin, V. A., Upper Limit of the Spectrum of Cosmic Rays, Journal of Experimental and Theoretical Physics Letters 4: 78–80, 1966
132. Zhang B. et al., High Energy Astrophysics, Frontiers of Physics, 8 (6), 605-608, 2013